Federal University of Espírito Santo

Technology Center

Postgraduate Program in Electrical Engineering

Augusto Cesar Federici Peterle

Performance Evaluation of a 5G-based Hybrid Visible Light and Radio Frequency Communication System

Vitória, ES

2024

Augusto Cesar Federici Peterle

Performance Evaluation of a 5G-based Hybrid Visible Light and Radio Frequency Communication System

This Master thesis was submitted to the Postgraduate Program in Electrical Engineering from the Technology Center of the Federal University of Espírito Santo, as partial requirement for the degree of Master in Electrical Engineering.

Federal University of Espírito Santo

Technology Center

Postgraduate Program in Electrical Engineering

Supervisor: Prof. Dr. Jair Adriano Lima Silva

Co-supervisor: Prof. Dr. Helder Roberto de Oliveira Rocha

Vitória, ES

2024

Augusto Cesar Federici Peterle

Performance Evaluation of a 5G-based Hybrid Visible Light and Radio Frequency Communication System

This Master thesis was submitted to the Postgraduate Program in Electrical Engineering from the Technology Center of the Federal University of Espírito Santo, as partial requirement for the degree of Master in Electrical Engineering.

Work approved. Vitória, ES, April 15th 2024:

Documento assinado digitalmente
JAIR ADRIANO LIMA SILVA
Data: 05/08/2024 15:49:20-0300
Verifique em https://validar.iti.gov.br

Prof. Dr. Jair Adriano Lima Silva
Supervisor

Documento assinado digitalmente
HELDER ROBERTO DE OLIVEIRA ROCHA
Data: 05/08/2024 15:53:27-0300
Verifique em https://validar.iti.gov.br

Prof. Dr. Helder Roberto de Oliveira Rocha
Co-supervisor

Documento assinado digitalmente
MARCELO EDUARDO VIEIRA SEGATTO
Data: 05/08/2024 16:36:37-0300
Verifique em https://validar.iti.gov.br

Prof. Dr. Marcelo Eduardo Vieira Segatto
Examiner

Documento assinado digitalmente
ALEXANDRE DE ALMEIDA PRADO POHL
Data: 05/08/2024 17:42:25-0300
Verifique em https://validar.iti.gov.br

Pof. Dr. Alexandre de Almeida Prado Pohl
External Examiner

Vitória, ES

2024

To my wife Isabela Schunk to the whole emotional support and patience during the whole journey.

Acknowledgements

Abstract

The development of 5G is an ongoing process and annually release are published by 3GPP considering fundamental aspects such as network's physical layer, numerology, bandwidth, modulation, among others. For new releases, a rapid prototyping is valuable for experimental demonstrations and proof-of-concepts. The usage of the Software-Defined Radio (SDR) technology is advantageous as it allows the implementation of modulation and demodulation procedures in software, enabling performance evaluations in various physical mediums, for instance both optical and Radio Frequency (RF).

Besides the prototyping need, the growing congestion and limitation of the RF spectrum have led to exploring alternative communication mediums. Visible Light Communication (VLC) technology has emerged as a solution, utilizing an unlicensed optical spectrum without substantial communication competition. The rise in popularity of Light Emitting Diodes (LEDs) for residential and commercial lighting supports this idea, as LEDs can be controlled and employed as information transmitters and its low power consumption. To this aim, studies regarding optical communication and Orthogonal Frequency Division Multiplexing (OFDM), as well as an in-depth explanation of 5G New Radio (NR) numerology were conducted. Therefore, a prototype was prepared and assembled for 5G NR signals generation for downlink via VLC, and for uplink via RF. The experimental results indicated that the coding techniques outlined by 5G NR integrate well with VLC, enabling the use of modulation levels up to 64-QAM. This outcome facilitated error-resistant communication for the transmitted data volume, showcasing a robust hybrid VLC/RF system capable of successfully supports relatively high data rates.

Keywords: Visible Light Communnications, 5G New Radio, Orthogonal Frequency Division Multiplexing, Software Defined Radio

Resumo

O desenvolvimento do 5G é um processo contínuo e anualmente são publicados lançamentos pela 3GPP considerando aspectos fundamentais como a camada física da rede, numerologia, largura de banda, modulação, entre outros. Para novos lançamentos, um prototipagem rápida é valiosa para demonstrações experimentais e provas de conceito. O uso da tecnologia de Rádio Definido por Software (SDR) é vantajoso, pois permite a implementação de procedimentos de modulação e demodulação em software, possibilitando avaliações de desempenho em diversos meios físicos, como ópticos e de Radiofrequência (RF).

Além da necessidade de prototipagem, a crescente congestão e limitação do espectro de RF têm levado à exploração de meios de comunicação alternativos. A tecnologia de Comunicação por Luz Visível (VLC) surgiu como uma solução, utilizando um espectro óptico não licenciado sem competição substancial de comunicação. O aumento da popularidade dos Diodos Emissores de Luz (LEDs) para iluminação residencial e comercial apoia essa ideia, pois os LEDs podem ser controlados e utilizados como transmissores de informação e consomem baixa potência. Com esse objetivo, foram realizados estudos sobre comunicação óptica e Multiplexação por Divisão de Frequência Ortogonal (OFDM), bem como uma explicação detalhada da numerologia do 5G New Radio (NR). Portanto, um protótipo foi preparado e montado para geração de sinais 5G NR para downlink via VLC e para uplink via RF. Os resultados experimentais indicaram que as técnicas de codificação delineadas pelo 5G NR se integram bem com o VLC, possibilitando o uso de níveis de modulação de até 64-QAM. Esse resultado facilitou a comunicação resistente a erros para o volume de dados transmitidos, demonstrando um sistema robusto híbrido VLC/RF capaz de suportar com sucesso taxas de dados relativamente altas.

Palavras-chave: Comunicações por Luz Visível, 5G New Radio, Multiplexação por Divisão de Frequência Ortogonal, Rádio Definido por Software.

List of Figures

List of Tables

List of abbreviations and acronyms

3GPP   3rd Generation Partnership Project

4G   Fourth Generation of Mobile Communications System

5G   Fifth Generation of Mobile Communications System

6G   Sixth Generation of Mobile Communications System

LTE   Long Term Evolution

IoT   Internet of Things

IIoT   Industrial Internet of Things

eMBB   enhanced mobile broadband

URLLC   ultra-reliable low-latency communications

mMTC   massive machine-type communication

NR   New Radio

RF   Radio Frequency

VLC   Visible Light Communication

Li-Fi   Light Fidelity

LED   Light Emitting Diode

SDR   Software Defined Radio

FPGA   Field Programmable Gate Arrays

DSP   Digital Signal Processing

ADC   Analog to Digital Converter

DAC   Digital to Analog Converter

gNB   gNodeB

UE   User Equipment

ACK   Acknowledge

NACK	Non Acknowledge
EVM	Error Vector Measurement
BER	Bit Error Rate
OWC	Optical Wireless Communication
OOK	On-Off-Keying
VPPM	Variable Pulse Position Modulation
CSK	Color Shift Keying
ICU	Intensive Care Units
EMI	Electromagnetic interference (EMI)
DC	Direct Current
PD	Photodiode
LOS	Line of Sight
OFDM	Orthogonal Frequency Division Multiplexing
CP	Cyclic Prefix
DFT	Discret Fourier Transform
FFT	Fast Fourier Transform
IDFT	Inverse Discret Fourier Transform
IFFT	Inverse Fast Fourier Transform
ZIF	Zero IF modulator
DUC	Digital up-converter
DDC	Digital down-converter
μ	5G NR Numerology
SCS	Subcarrier Spacing
RB	Resource Block
RE	Resource Element
RLC	Radio Link Control

PHY	Physical Layer
MAC	Medium Access Control Layer
CCCH	Common Control Channel
DCCH	Dedicated Control Channel
DTCH	Dedicated Traffic Control Channel
BCCH	Broadcast Control Channel
PCCH	Pagin Control Channel
DL-SCH	Downlink Shared Channel
UL-SCH	Uplink Shared Channel
BCH	Broadcast Channel
PCH	Paging Channel
RACH	Random Access Channel
CRC	Cyclic Redundancy Check
CB	Codeblock
LDPC	Low-Density Parity Check
TBS	Transport Block Size
PDSCH	Physical Downlink Shared Channel
PDCCH	Physical Downlink Control Channel
PBCH	Physical Broadcast Channel
PRACH	Physical Random Access Channel
PUSCH	Physical Uplink Shared Channel
PUCCH	Physical Uplink Control Channel
SSB	Synchronization Signal Block
PSS	Primary Synchronization Signal
SSS	Secondary Synchronization Signal
MIB	Master Informtion Block

DMRS	Demodulation Reference Symbols
MCS	Modulation Coding Scheme
SRS	Sounding Reference Signal
HARQ	Hybrid Automatic Repeat reQuest
DCI	Downlink Control Information
UCI	Uplink Control Information
M2k	ADALM 2000
TIA	Transimpedance Amplifier
I/Q	In-phase and quadrature components
LNA	Low Noise Amplifier
SOC	System on Chip
FIR	Finite Impulse Response

Contents

1 Introduction

The world is currently experiencing a revolutionary wave in the field of communications systems. Several types of devices such as mobile phones, computers, sensors, cameras, and many others now require seamless connectivity to networks, including the Internet. This demand is driven by the modernization of devices, the emergence of smart cities, autonomous operations, and the need for extensive databases for machine learning [2]. As a result, there is an increasing need for faster and more reliable wireless connectivity.

The fifth generation of telecommunications systems, commonly referred to as 5G, is expected to provide numerous advantages over its predecessor, the Long Term Evolution (4G-LTE), developed by the 3rd Generation Partnership Project (3GPP). The 5G technology aims to offer connectivity, ensuring that users can stay connected "Anywhere and Anytime". Additionally, it introduces a low-power consumption aspect, specifically designed to cater to the requirements of the Internet of Things (IoT) and Industrial Internet of Things (IIoT) devices [3]. The development of 5G is still ongoing within the 3GPP, involving significant changes to network structure, data transmission, and the physical layer, which pose risks. To mitigate these risks, the 3GPP is prioritizing compatibility with existing 4G-LTE systems [4]. Additionally, 3GPP's Release 15 introduced a new air interface called "New Radio" [5], designed with scalability and flexibility to meet the requirements of enhanced mobile broadband (eMBB), ultra-reliable low-latency communications (URLLC), and massive machine-type communications (mMTC) [6]. Furthermore, 5G proposes utilizing frequency bands up to 6 GHz for mobile applications in the FR1 band and millimeter-wave spectrum in the FR2 band, covering the range from 23 to 52 GHz [7].

As depicted in Figure 1, multiple releases, from 13 to 17, have already been published among 2015 and 2022, with the latest version currently being Release 18. Release 16 marked the first complete 5G release, followed by subsequent improvements in releases 16 and 17. The discussions within Release 18 are focused on advanced topics, with the 3GPP approving studies on energy efficiency for 5G New Radio. These studies encompass enhancements in physical coverage and even delve into aspects of the modulation formats, such as the switching between Cyclic Prefix - Orthogonal Frequency Division Multiplexing (CP-OFDM) and Discrete Fourier Transform Spread Orthogonal Frequency Division Multiplexing (DFT-S-OFDM) [1].

The 3GPP remains active by publishing annual improvements for 5G, thereby dynamically updating the new standard. In the current landscape of intense innovation and rapid advancements, numerous scientific research studies are being conducted. This highlights the clear need to consider strategies for fast hardware prototyping with 5G
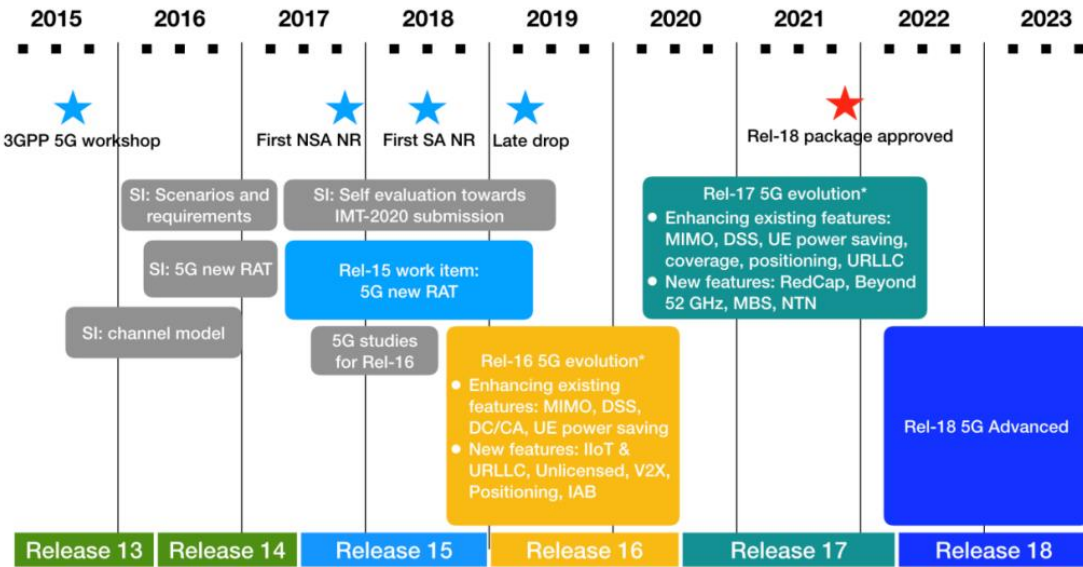
Figure 1 – 5G Milestones Roadmap [1]

specifications. With the continuous development of connectivity technologies and the introduction of the mMTC (massive Machine-Type Communication) concept, the demand for RF communication connectivity has significantly increased. An example of this can be seen in Figure 2 part. a), which depicts a scenario where multiple devices connect to a single access point. However, due to the limited bandwidth of this access point, the allocation of bandwidth for each new connected device decreases progressively. This phenomenon is known as "RF Spectrum Crunch" [8] and has significant impacts on connection quality and capacity.

A promising solution to mitigate these effects is exploring visible light connectivity [9]. By utilizing visible light as a data transmission medium, it is possible to overcome the bandwidth limitations of RF Spectrum Crunch. Visible light communication technology offers an efficient and high-performance alternative, allowing for increased connection capacity without compromising quality. Figure 2 part. b) shows a scenario where visible light is used as a communication medium. In this case, the light link is used as a supplement to meet the connection demands that could potentially overwhelm the Radio Frequency Access Point, causing a collapse. Light Emitting Diodes (LEDs) emit light in the visible spectrum (380-700 nm) [10] and offer benefits such as fast switching, low power consumption, and a bandwidth range of 10 to 20 MHz. Moreover, advancements in LED production have provided cost reductions, making them more affordable [11]. The combination of lower costs and widespread popularity significantly promotes the implementation of VLC systems.
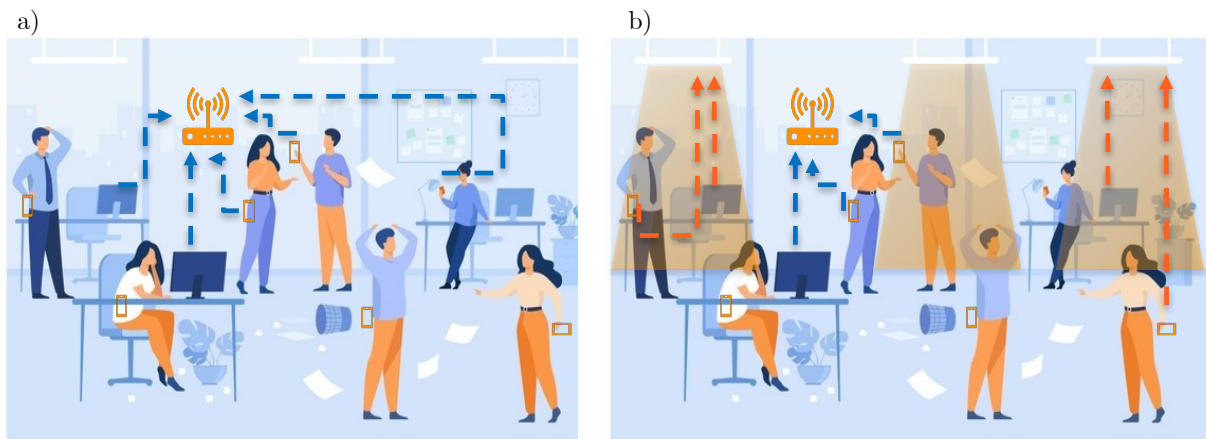
Figure 2 – a) A scenario with several devices connected a single RF Access Point with limited bandwidth. b) The Light Emitting Diode lighting is used as an access point for data transfer, effectively dividing the connection demand with the Radio Frequency medium.

1.1 Problem Statement

The fast evolution of 5G technology, marked by annual releases from the 3GPP, underscores the need for agile prototyping to validate experimental demonstrations and proofs-of-concept. This iterative development relies on the SDR technology, enabling flexible implementation of modulation and demodulation procedures in software across various physical mediums, including optical and RF channels. Additionally, the growing congestion and limitations in the RF spectrum have driven exploration of alternative communication mediums, such as those based on VLC. Utilizing the unlicensed optical spectrum, VLC presents a promising solution, especially with the widespread adoption of LEDs in both residential and commercial lighting. The controllable nature of LEDs allows them to serve as information transmitters, alongside their low power consumption. Consequently, investigations into optical communication, OFDM and the intricacies of 5G New Radio numerology should be pursued.

Therefore, the research question addressed in this work is related to the development of prototypes able to transmit 5G NR signals via VLC and RF channels. In particular, the aim is to investigate how innovative 5G mechanisms such as advanced channel coding techniques can enhance communication performance and hence reliability of full-duplex VLC systems.

Furthermore, recent prototyping endeavors, as referenced in [12] and [13], have predominantly concentrated on VLC downlink transmission and have been limited to half-duplex systems. The prototype presented here extends beyond this by incorporating VLC uplink transmission alongside RF links, as detailed in [14]. This expansion introduces a connection-oriented prototype that utilizes uplink transmission for ACK/NACK messages, thereby bolstering system reliability.

The experiment meticulously evaluates the prototype across various scenarios, encompassing different coderates, modulation levels, bias currents, and VLC link lengths, to cover a wide range of conditions. Results demonstrate the compatibility of 5G NR coding techniques with VLC, allowing modulation up to 64QAM and establishing a robust hybrid VLC/RF system capable of supporting high data rates while ensuring error-resistant communication for transmitted data volumes. Additionally, this approach exploits a channel underutilized by traditional communication methods and addresses nonlinear factors inherent in visible light systems, such as saturation, all while maintaining reliability.

1.2 Objectives of this Work

This research aims at the development of an innovative hybrid VLC/RF and full-duplex systems by adapting 5G NR electrical signals. To achieve the main objective, the following specific task were conducted:

- an extensive study involving the generation of signals compliant with the 5G NR standard;

- an in-depth research focusing on the paradigms and algorithms commonly employed in transmissions using Software-Defined Radios (SDRs);

- a prototype development for downlinks using visible light communication and uplinks through traditional RF communication;

- and a comprehensive proof-of-concept for performance evaluation and functionality.

1.3 Materials and Methods

The starting point of this work was a literature review on the three main pillars involved in the research question: Visible Light Communications, 5G New Radio numerology, and Software-Defined Radio. Based on the state-of-the-art review, the necessary adaptations were made to use 5G NR in downlink, employing signals named as Physical Broadcast Channel (PBCH), Physical Downlink Shared Channel (PDSCH), and Physical Downlink Control Channel (PDCCH); as well as uplink signals like Sounding Reference Signals (SRS), Physical Uplink Shared Channel (PUSCH), and Physical Uplink Control Channel (PUCCH), for the VLC/RF prototype reality.

After the generation of the 5G NR signals and their respective Resource Grids, appropriate adjustments were made to place these signal formats into real systems using Analog-to-Digital Converters (ADCs) and Digital-to-Analog Converters (DACs), which

their correspondent limitations. Each equipment used in the prototype was characterized, and its frequency response obtained. With a clear understanding of real transmission paradigms and the equipment characterization, transmission tests were performed. In this case, the downlink transmitter act as the 5G base station (gNodeB), and the receiving device act as the User Equipment (UE). The gNodeB sends downlinks through the VLC link, and the UE receives the downlink and checks the Cyclic Redundancy Checks (CRCs). If no errors are identified, the UE sends an Acknowledge (ACK) signal through RF link. Otherwise, a (non-Acknoladge) NACK signal.

Although the test setup has two communication channels (RF and VLC), the focus of the work is to evaluate 5G performance on the VLC link. The assumption is that the RF channel will always operate in a fixed nearby region, ensuring that all Uplink signals are sent from the UE and received at the gNodeB. However, not every downlink will arrive successfully, which may necessitate a retransmission.

Finally, the system performance was evaluated through metrics such as Error Vector Magnitude (EVM), Bit Error Rate (BER), and the number of retransmissions, with the variation of parameters including bias current, transmission distance, and code rate. These evaluations provided valuable insights into the primary trade-offs of the VLC system. The EVM measurement helped assess the accuracy of the transmitted signals compared to their ideal values, offering a clear indication of signal quality and constellations. The BER analysis allowed for an understanding of the error rate in the received data, highlighting the system's robustness and error correction capabilities. By varying the bias current, the impact on the overall system performance was investigated. Different bias current levels might influence the optical power output and, consequently, the achievable data rates and transmission range. Additionally, the effect of transmission distance on the system's performance was studied. Understanding how the VLC link performs at different distances is crucial to determine the practical limitations and design suitable communication strategies accordingly. Furthermore, the influence of the code rate on the system's performance was assessed. Adjusting the code rate could affect the error correction capabilities, channel capacity, and spectral efficiency, necessitating a trade-off between data throughput and error resilience.

Through these evaluations, a comprehensive understanding of the VLC transmission system's strengths and limitations was achieved, providing valuable insights for optimizing and designing efficient visible light communication solutions in various practical scenarios.

1.4 Main Contributions of this Work

This work presents an adaptation of 5G NR signals in the context of visible light communication systems. Moreover, it outlines the assembly of a full-duplex prototype

capable of utilizing two distinct communication mediums: VLC and RF. Additionally, the study delves into the key challenges pertaining to Digital Signal Processing (DSP) during the system's implementation.

Figure 3 provides a high-level overview of the implemented prototype. The gNodeB comprises an output interface, utilizing an ADALM 2000 device to serve as the VLC interface through its DAC. Additionally, an ADALM-PLUTO device is employed to receive the uplinks with ACK/NACK signals through its receiving antenna. On the other hand, the UE, equipped with the same devices as the gNodeB, but performs distinct functions. The ADALM 2000 at the UE receives signals from the Photodetector and decode them. Moreover, the UE's ADALM-PLUTO sends the Uplink signals along with their respective ACK/NACK signals.

The VLC channel interfaces are illustrated in Figure 3. The signals from the gNodeB's ADALM 2000 are amplified and subjected to DC-level adjustment to avoid negative clipping before transmission to the LED. To enhance signal transmission, optical collimators are positioned between the LED and the Photodetector (PD), concentrating the light power emitted by the LED onto the PD's detection area. This process amplifies the detected signals, and through appropriate amplification, the transmitted information that passed through the VLC channel can be effectively recovered.
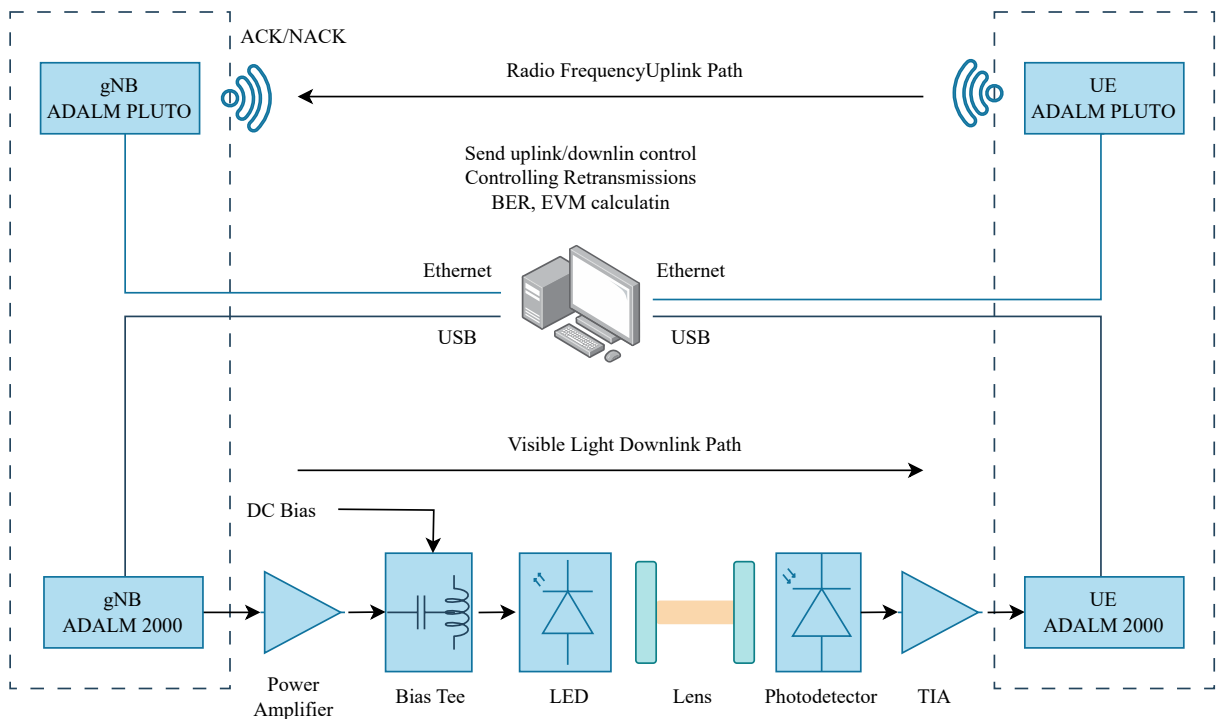
Figure 3 – The gNodeB is composed of an ADALM 2000, which transmits Downlinks through its DAC to the VLC interface, while it receives Uplinks through the RX antenna of the ADALM-PLUTO. On the other hand, the UE receives Downlinks through the ADC of the ADALM 2000 and transmits Uplinks through the TX antenna of its ADALM-PLUTO.

Other tests with OFDM signals were conducted, as listed in the publication below, which in turn, motivated the use of the 5G NR standard in this study. The list of publications during the whole study can be seen below:

1 - A. C. F. Peterle, W. Costa, H. Camporez, M. Segatto, H. Rocha and J. A. L. Silva, "Orthogonal Chirp Division Multiplexing in Visible Light Communication: A Performance Comparison with OFDM-based Systems," *2021 SBMO/IEEE MTT-S International Microwave and Optoelectronics Conference (IMOC)*, Fortaleza, Brazil, 2021, pp. 1-3.

2 - Peterle, A. C. F., Costa, W., Camporez, H., Segatto, M., Rocha, H., & Silva, J. A. L.. (2023). Comparing the Performance of OFDM and OCDM-based Visible Light Communications: Numerical and Experimental Analysis. *Journal of Microwaves, Optoelectronics and Electromagnetic Applications*, 22(1), 196–207.

1.5   Organization of this Work

The work will is divided into six chapters, with the current chapter focusing on the introduction, motivation, and methodology addressed. Chapter 2 covers fundamental concepts in visible light communication systems, focusing on LED and Photodetector operations. Chapter 3 delves into OFDM encompassing theoretical aspects and practical implementation. In Chapter 4, the 5G New Radio is explored in depth, including discussions on physical, logical, and transport channels, as well as signal generation for demodulation, synchronization, and Resource Allocation. Chapter 5 details the practical implementation of the 5G New Radio transmission and reception prototype within the context of visible light communication, including component characterization and frequency response analysis. Chapter 6 presents the experiment results, covering downlink transmission via VLC and uplink through the RF interface. Finally, Chapter 7 provides the main conclusions and discusses potential subjects for future research.

2 Visible Light Communication

Conventional wireless communication systems rely on the radio spectrum for transmission. However, the escalating demand for bandwidth has underscored the potential of Optical Wireless Communications (OWC) systems [15]. Unlike conventional methods, OWC systems utilize a unique portion of the electromagnetic spectrum known as the optical spectrum. As depicted in Figure 4, this spectrum spans from infrared to ultraviolet light [16].
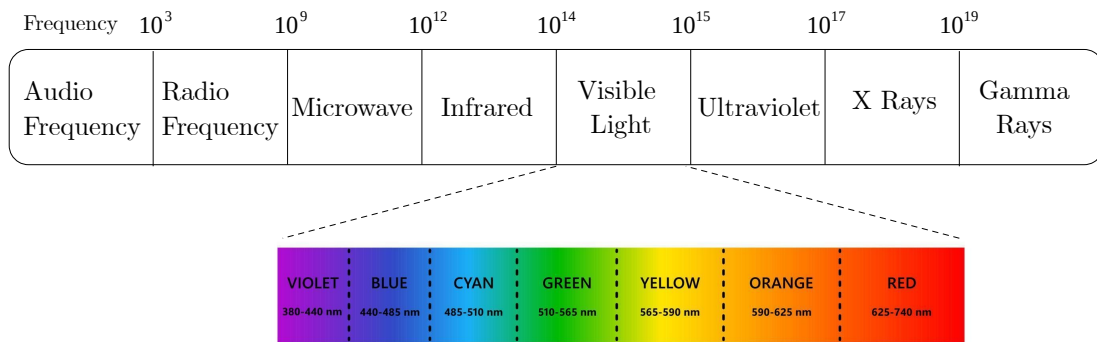
Figure 4 – Spectra with a focus on the visible light range, wich begins at 430 THz and extends up to 790 THz. In terms of wavelengths, this spectrum spans from 380 nm to 780 nm.

Visible Light Communication is a type OWC system that utilizes the visible light spectrum range. The utilization of this light range presents several advantages when compared to the adjacent ranges. First and foremost, it is important to highlight that systems using infrared and ultraviolet light may pose risks to human health [17], whereas VLC stands out as a safe alternative, devoid of these health risks. Furthermore, infrared-based systems often face challenges related to high reflectivity [18], resulting in a restriction of available bandwidth and, consequently, limiting transmission capacity. On the other hand, VLC, by using the visible light range, can exploit a wider bandwidth, allowing for higher and more efficient transmission rates. In it´s turn, ultraviolet-based systems often encounter significant interferences in the propagation channel and are additionally limited to short communication distances [19]. In this context, VLC emerges as a promising alternative, offering more directional propagation and a greater range, making it especially suitable for applications requiring long-distance communication and higher reliability.

In summary, VLC stands out as a advantageous choice, due to its safety for human health, improved data transmission capacity due to expanded bandwidth, and better performance in terms of range and interference when compared to infrared and ultraviolet-based systems. Moreover, other factors further contribute to the choice of VLC, such as the increasing popularity of LED usage and the duality of the transmitter acting both as a

luminary and a communication device. Recent research has made significant advancements in the VLC field, leading to the establishment of the IEEE 802.15.7 standard [20]. This standard encompasses the following modulation techniques:

- **On-Off Keying (OOK)**: This is a simple modulation technique where data is transmitted by toggling the states of a light transmitter between "on"and "off."The receiver detects the presence or absence of light to decode the transmitted bits. While straightforward, OOK is not as efficient in terms of data rate and noise resistance [21].

- **Variable Pulse Position Modulation (VPPM)**: In this method, a light pulse is divided into discrete positions, and information is encoded by varying the position of the pulse within a fixed time interval. The change in pulse position represents the transmission of bits. This allows for higher data transmission efficiency compared to OOK [21], as multiple bits can be transmitted in a single light pulse.

- **Color Shift Keying (CSK)**: This technique involves encoding information by changing the color of the transmitted light, utilizing the chromatic dispersion of the light spectrum [22]. Colored LEDs are used to represent different symbols or bits. Detection is achieved by measuring the received light color and decoding the corresponding symbols. CSK has the potential to transmit multiple bits per symbol, making it efficient in terms of data rate.

Another extensively utilized technique in wireless systems, such as 4G LTE, Wi-Max, and WiFi [23], and also pioneered by Light Fidelity [1] (Li-Fi) [24] is Orthogonal Frequency Division Multiplexing (OFDM). This technique is the main physical layer point of the 5G New Radio [25]. The implementation of OFDM in the context of Visible Light Communication is indeed viable, as indicated in [26] and [27]. However, this endeavor is accompanied by several challenges that must be addressed. First and foremost, it's imperative to acknowledge that an OFDM signal comprises both real and complex components, requiring the transmitter to modulate two orthogonal carriers despite utilizing only one LED as the transmitter [28].. Another important consideration revolves around the bipolar nature of OFDM signals, encompassing both positive and negative amplitudes. Such challenges and the proposed solutions within the scope of VLC systems is addressed in the next Section of this thesis.

The 5G NR technology is in the process of being deployed worldwide. However, the discussion about the sixth generation (6G) of telecommunications systems is already underway. According to the cited article [29], VLC is a promising technology for 6G due to advances that have enabled transmissions in the Gbps range, secure links, usage of a previously unexplored spectrum, and the low power consumption of transmitting

---

[1]   A figurative term for VLC.

LEDs. On the other hand, the study conducted in [30] suggests an integration between 6G and underwater systems, utilizing advanced modulation techniques and machine learning algorithms for digital signal processing. The article [31] also notes the feasibility of VLC for Telemedicine applications, due to its unique security features and high data rates. Furthermore, in the field of medicine, a study [32] highlights the benefits of using VLC for communication in hospital intensive care units, thanks to its RF and Electromagnetic Interference (EMI) free nature. Considering these benefits, studies on VLC become relevant and point towards its promising adoption in future telecommunications systems.

2.1 LED as VLC transmitter

The Light-Emitting Diode is a semiconductor device widely used for lighting due to its low energy consumption and high illuminance. However, beyond its traditional use, the LED can also play a significant role as a low-power communication medium in the optical spectrum. In semiconductor physics, a diode is constructed using semiconductor materials such as silicon or germanium, and a process called doping is carried out on the material, creating two distinct regions. One region has an excess of electrons (n), while the other has holes that have an affinity for electrons (p). This combination of p-n regions occurs within a semiconductor material [33]. In Figure 5, an appropriate voltage is applied between the anode and cathode, causing electrons to move from the n-type region towards the p-type region. During this recombination process, the energy of the free, unbound electrons transitions to a lower energy state, and this energy is emitted in the form of photons. The acceleration of electrons, driven by the battery, compels them to circulate between these regions, altering their original state and forcing them to release energy in the form of photons, thereby emitting light.

When an external voltage source is applied to the LED, it initiates a flow of electrons from the cathode to the conduction band. Simultaneously, holes are created in the valence band. Electrons in the conduction band have higher energy levels compared to those in the valence band. As a result, these high-energy electrons jump to the valence band, releasing energy in the form of photons [34]. These recombination process is shown in Figure 6. Hence, for proper operation, a unidirectional current is required, along with the correct voltage applied to avoid breaking the pn junction. Therefore, an electronic component capable of correctly supplying power to an LED is needed.

As mentioned earlier, LEDs permit current flow in only one direction. However, in OFDM-based modulation systems, the generated signals fluctuate between positive and negative values. To overcome this constraint of LEDs, a Direct Current (DC) level is introduced to the input modulating signal. Another aspect concerns LED linearity, where the luminous flux produced by the current flowing through the LED can be defined by [10].
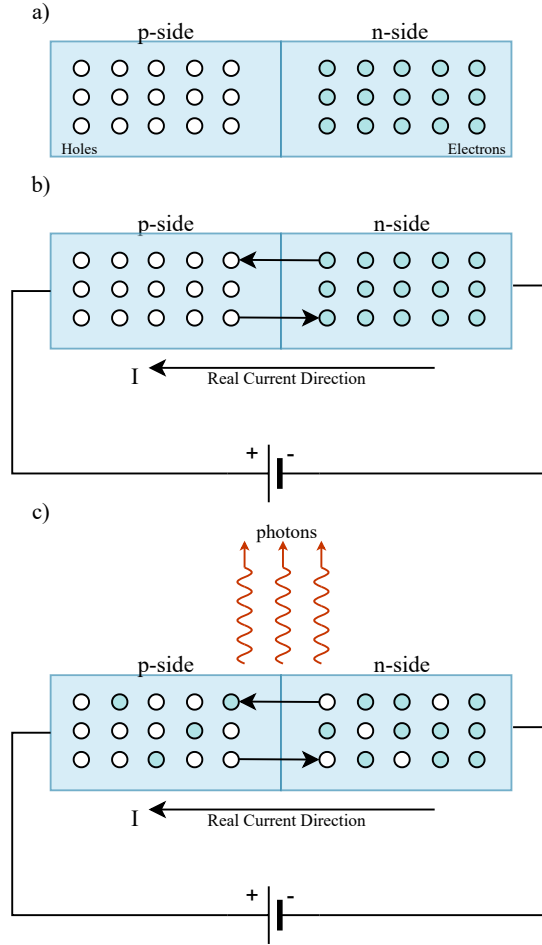
Figure 5 – In a) the balance between electron holes and electrons is observed. In b) a unidirectional direct current (real direction) is applied, initiating the recombination process. C) Several electrons and holes have moved and recombined.
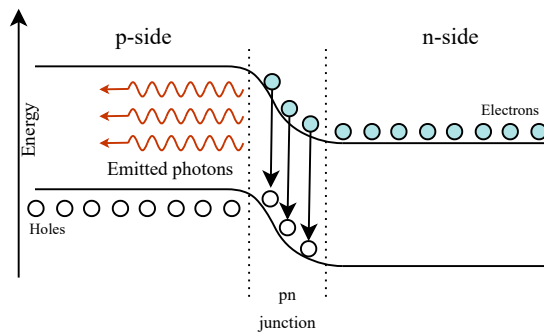
Figure 6 – As depicted in Figure 5, the electric current compels electrons to migrate from the n-region to the p-region. However, during the recombination process, electrons transition from a higher energy level to a lower one. In this process, photons are emitted, giving rise to the formation of light beams.

$$P_{LED} = \frac{I_{LED}}{\left(\zeta + \left(\frac{I_{LED}}{P_{MAX}}\right)^{2k}\right)^{1/2k}} \tag{2.1}$$

In equation 2.1 I_{LED} represents the current flowing through the LED, P_{MAX} denotes the LED's maximum power, ζ serves as an adjustment constant, and k is the knee factor that fine-tunes the level of intensity saturation, yielding P_{LED} in Watts. Notably, the output power generated by the LED exhibits non-linear behavior. The behavior is illustrated in Figure 7, depicting the LED's response when biased with a specific DC level.
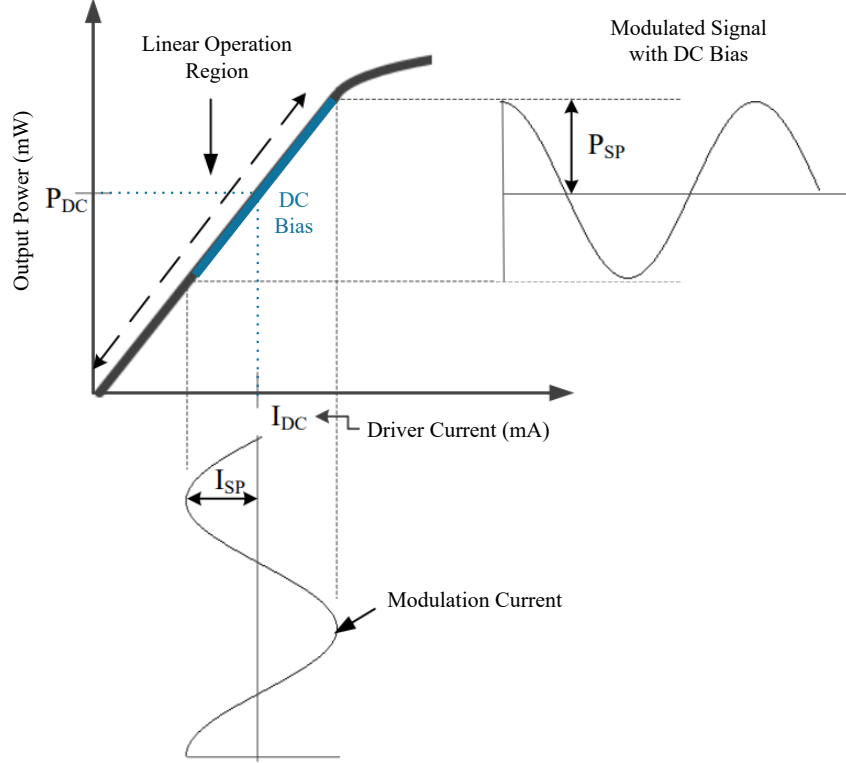
Figure 7 – The LED is biased by a DC level. A bias current is introduced, shifting the entire modulating signal to positive values only.

As depicted in Figure 7, the luminous power of the LED does not exhibit a perfectly linear relationship with the input current. Shifting the bias point to very high DC levels can bring the LED's operation closer to its non-linear region. In the other hand, employing a very low DC level may result in negative clipping when dealing with a low-amplitude modulating signal. Therefore, there exists a trade-off between these choices. While a low-amplitude modulating signal is highly susceptible to thermal noise in photodetection, increasing its amplitude can lead to negative clipping with a low DC level and to a non-linear region with a high DC level.

Figure 8 illustrates the small-signal model for an LED, where P_{signal} represents the power of the input signal and P_{out} denotes the power of the output optical signal. R_s and L_s stand for series resistance and inductance, respectively. C_d and C_b represent the diffusion and barrier capacitance of the LED, respectively. η signifies the photoelectric conversion efficiency, and R_d is the small-signal diode resistance of an LED. These values are inherent to the construction of the LED [35]. It's important to note the presence
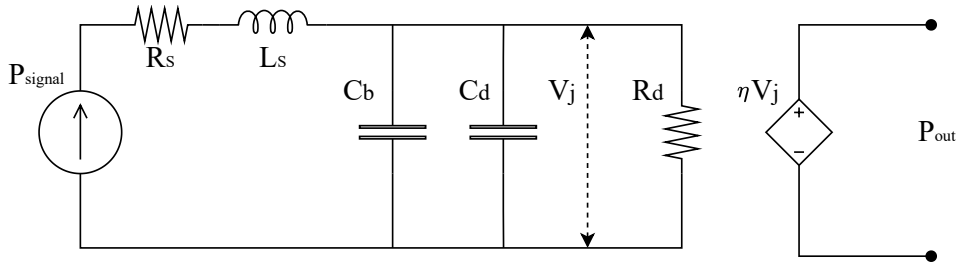
Figure 8 – Light emitting diode signal model

of an RLC circuit that imposes a second order low-pass characteristic, attenuating high frequencies of P_{signal}.

2.2 Photodiode as VLC receiver

The PIN photodiode is constructed with a pn junction, where a layer of intrinsic semiconductor material sits between the p-type and n-type materials. This intrinsic layer is essentially the heart of the device, actively responsive to light and functioning as a depletion region [36]. Furthermore, its positioning is meticulously done to not only optimize light exposure but also to minimize the inherent capacitance of the photodetector. This photodiode operates in a state of reverse bias, which means that when incoming photons hit, they get absorbed within the depletion region, a place of high-intensity electric field. This electric field ensures a rapid separation and collection of the photo-generated carriers, which are electron-hole pairs, efficiently directing them to their respective regions in p (holes) and n (electrons) before they get a chance to recombine [37].

In Figure 9, when light strikes the PIN photodiode, it gives rise to electron-hole pairs within the depletion region. This phenomenon occurs because the semiconductor material absorbs photons. The energy from these photons is then transferred to the electrons, prompting them to transition from the valence band to the conduction band, thereby creating holes in the valence band.

As seen for LEDs, photodetectors also exhibit a saturation effect. As illustrated in Figure 11, at low luminous powers, even with minimal or no light, the photodiode emits a so-called dark current I_D. Moreover, a certain amount of luminous power is required to increase the output electrical current. However, at the extreme end of the curve, it is observed that indiscriminately increasing the incident luminous power leads to saturation [38]. In this scenario, the output electrical current stay near beyond the level I_S. Therefore, similar to what was discussed for LEDs, it is more beneficial to operate with an optical bias level that keeps the photodetector's response curve within the linear region. This approach helps to avoid signal distortions and ensures better reliability in reception.

The Figure 12 depicts the small-signal model of the pin photodiode, where C_j
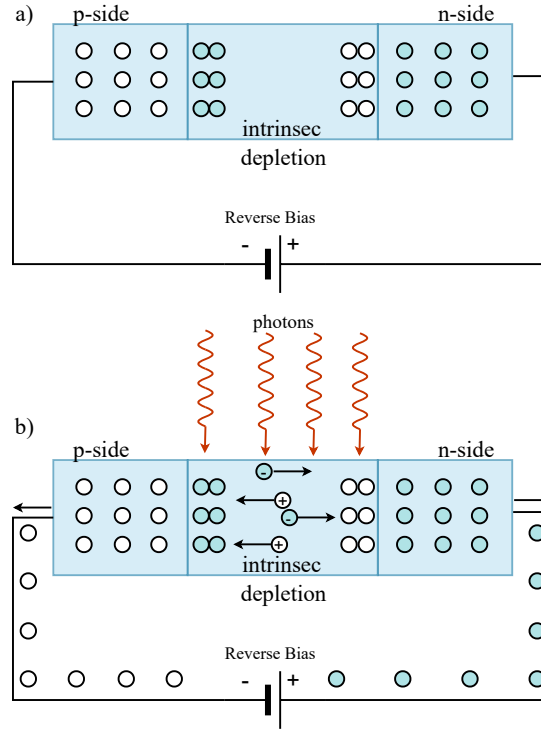
Figure 9 – In a) Reverse bias applied to the Photodiode, and in b) when the PIN is hitted by light the photons energy is transferred to the electrons and then move themselves.
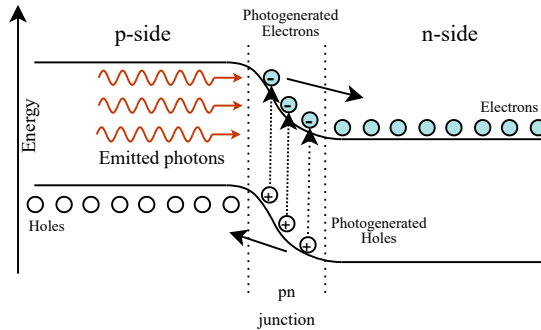
Figure 10 – A photon incident with energy greater than the bandgap energy of the semiconductor energizes an electron, moving it from the valence band to the conduction band.

represents the junction capacitance, R_j is the junction resistance, C_p stands for parasitic capacitance, R_s denotes the series resistance due to contacts between the p and n regions, and R_L is the load resistance, $i_0(\omega)$ is the current converted from optical signal and $i(\omega)$ is the current flowing in the load [39]. It's important to note that there will be an equivalent circuit $Z(\omega)$ formed by R_s and C_p, which will impose a first order low-pass characteristic to the frequency response of the pin photodiode. Hence, at higher frequencies, there will be attenuation of the received signal. In this case, it is crucial to consider the bandwidths available from the chosen photodetector in the design.
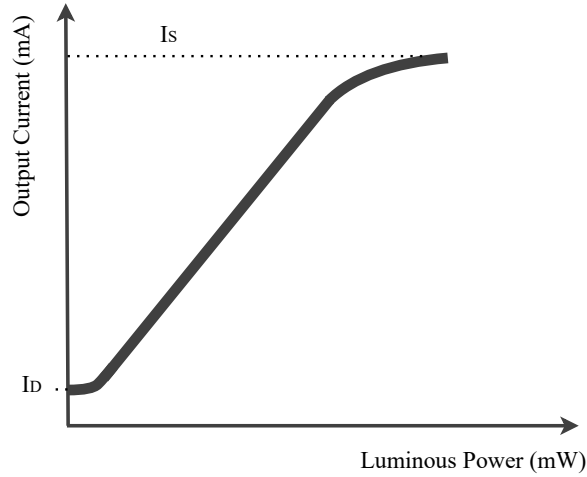
Figure 11 – A saturation effect, after a certain level of luminous power, the output current of the photodetector becomes confined to a value very close to I_S.
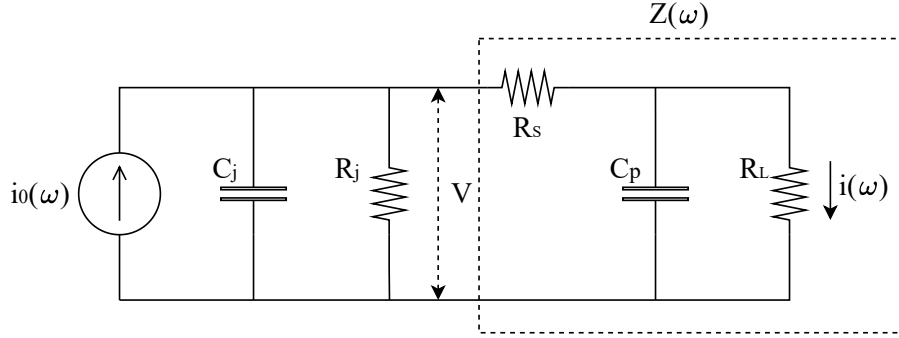
Figure 12 – Photodiode pin small signal model

2.3   VLC Line-of-Sight Channel Model

When dealing with wireless communication, such as radio, optical communication (as in VLC), or even satellite communication, the acronym LOS stands for Line of Sight. This means that there are no physical obstacles between the device transmitting information (the transmitter) and the device receiving that information (the receiver). Having a LOS connection is the ideal scenario to ensure that the signal transmission is efficient and reliable because there is nothing in the way that could interfere with or weaken the signal.

The LOS channel model considered in this work is illustrated in Figure 13. It consists of a transmitter in which the light emission is provided by an LED and a receiver that detects the light by a photodetector.

Equation (2.2) shows the model to estimate the optical wireless channel frequency response [16]:

$$H(0) = \begin{cases} \frac{(m+1)A}{2\pi d^2} \cos^m(\phi) T_s g(\psi) \cos(\psi), & 0 \le \psi \le \psi_c \\ 0, & \psi > \psi_c \end{cases} \tag{2.2}$$
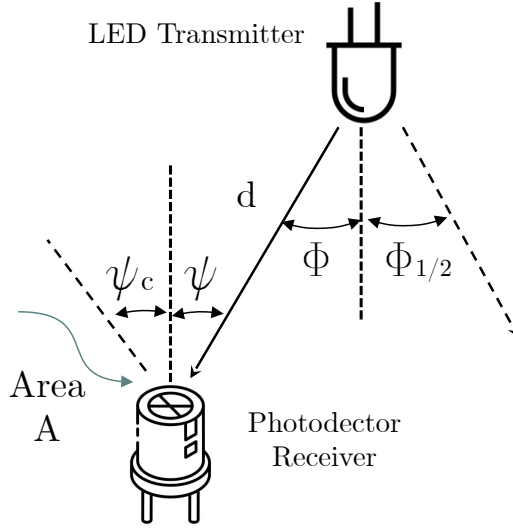
Figure 13 – A schematic depicting visible light communication, specifically emphasizing the transmitting and receiving components of visible light.

where A denotes the area of the photodetector, while d signifies the distance between the transmitter and receiver. T_s represents the gain of an optical filter, and $g(\psi)$ is associated with the gain of an optical collimator, as discussed in [40]. Additionally, ϕ refers to the angle of irradiance concerning the axis normal to the transmitter surface, while ψ indicates the angle of incidence concerning the axis normal to the receiver surface. The parameter ψ_C is crucial for understanding the concentrator's field of view (FOV), defining the semiangle at half power. Moreover, the variable m plays a vital role in characterizing the order of Lambertian emission and is intricately linked to the directivity of the light beam being emitted. This value is determined by the semi-angle at half power of the transmitter, denoted as $\phi_{1/2}$, and calculated as the following Equation (2.3),

$$m = \frac{-ln\,2}{ln\left(cos\phi_{1/2}\right)} \tag{2.3}$$

in which ln represents the Nepierian logarithm, and $\phi_{1/2}$ denotes the half-power angle or semiangle, which signifies the angle at which half of the illuminance provided by the LED source. The half-power angle directly impacts the directivity of the transmitter, indicating the maximum extent of the lobe that encompasses 50% of the radiant energy within a plane.

In a VLC LOS system model, the received optical power can be obtained as $P_r = H(0) \cdot P_{LED}$. This equations hold a vital role in our comprehension of the transmission and reception of optical power within VLC systems, establishing a fundamental cornerstone in optical communication engineering.

3 OFDM Basics

A multi-carrier system modulates multiple subcarriers to achieve maximum spectral efficiency within a specific range of the spectrum. The technique referred to as Orthogonal Frequency Division Multiplexing (OFDM) divides these subcarriers through frequency spacing in a manner ensuring their orthogonality [41]. Thus, the multiplex of a variety of data symbols, such as M-PSK, M-QAM, or M-PAM, can occur in parallel on these subcarriers, resulting in significantly enhanced data throughput when compared with a single-carrier system. As consequence, a symbol with duration T_s can be subdivided into n subcarriers such that the difference in the central frequency between carriers is fixed. Considering the $k-th$ subcarrier and the previous $l-th$ subcarrier as presented in Equation (3.1):

$$f_k - f_l = \frac{n}{T_s} \tag{3.1}$$

where n is a integer number and $n > 0$. The waveform of the $k-th$ subcarrier is obtained using the *rect* function as follows:

$$s_k(t) = rect\left(\frac{t}{T_s}\right) e^{j2\pi f_k t}. \tag{3.2}$$

$$rect(t) = \begin{cases} 1 & -1/2 < t \leq 1/2 \\ 0, & otherwise \end{cases} \tag{3.3}$$

The subcarriers s_k and s_l for $l \neq k$ are considered orthogonal whether complex inner product is zero [41], according to Equation (3.4).

$$\langle s_k, s_i \rangle = \frac{1}{T_s} \int_{-T_s/2}^{T_s/2} s_k(t) s_l^* \, dt = \frac{sin(\pi(f_k - f_l)T_s}{\pi(f_k - f_l)T_s}$$
$$= sinc(f_k - f_l)T|_{f_k - f_l = n/T_s} = 0 \tag{3.4}$$

where $sinc(x) = sin(\pi x)/(\pi x)$. The Equation (3.4) would not be zero only if $f_k = f_l$, i.e., in the same subcarrier. Therefore, an arbitrary analogical $s(t)$ OFDM signal could be generated as proposed in Equation 3.5.

$$s(t) = \begin{cases} \sum_{k=0}^{N-1} X_k e^{j2\pi kt/T_s}, & -T_s/2 < t \leq T_s/2 \\ 0, & otherwise \end{cases} \tag{3.5}$$

where X_k is the symbol that modulates the k-th subcarrier. To convert from the continuous-time OFDM signal to discrete-time, let $t = mT$ in Equation 3.5, where the signal was

sampled in the interval $T_s/2 < t < T_s/2$ with a sample interval $T = T_s/N$ and N is an integer value.

$$s(mT) = \begin{cases} \sum_{k=0}^{N-1} X_k e^{j2\pi kmT/T_s}, & -T_s/2 < mT \le T_s/2 \\ 0, & otherwise \end{cases} \tag{3.6}$$

Then, considering $T_s/T = N$ the Equation (3.6) can be rewritten as

$$s(mT) = \begin{cases} \sum_{k=0}^{N-1} X_k e^{j2\pi \frac{km}{N}}, & -T_s/2 < mT \le T_s/2 \\ 0, & otherwise, \end{cases} \tag{3.7}$$

which means that the OFDM multiplexing technique utilizes an Inverse Discrete Fourier Transform (IDFT) to achieve multiplexing. To enhance processing efficiency, the IDFT operation can be executed using the Inverse Fast Fourier Transform (IFFT) algorithm, particularly beneficial when the number of subcarriers is a power of 2 [41]. While the conventional IDFT algorithm requires N^2 complex multiplications, the IFFT algorithm reduces this requirement to $(N/2) \cdot \log_2(N)$ complex multiplications [42]. Figure 14.a) depicts the orthogonal subcarriers that can be modulated by digital symbols, while Figure 14.b) provides an illustration of the entire spectrum.
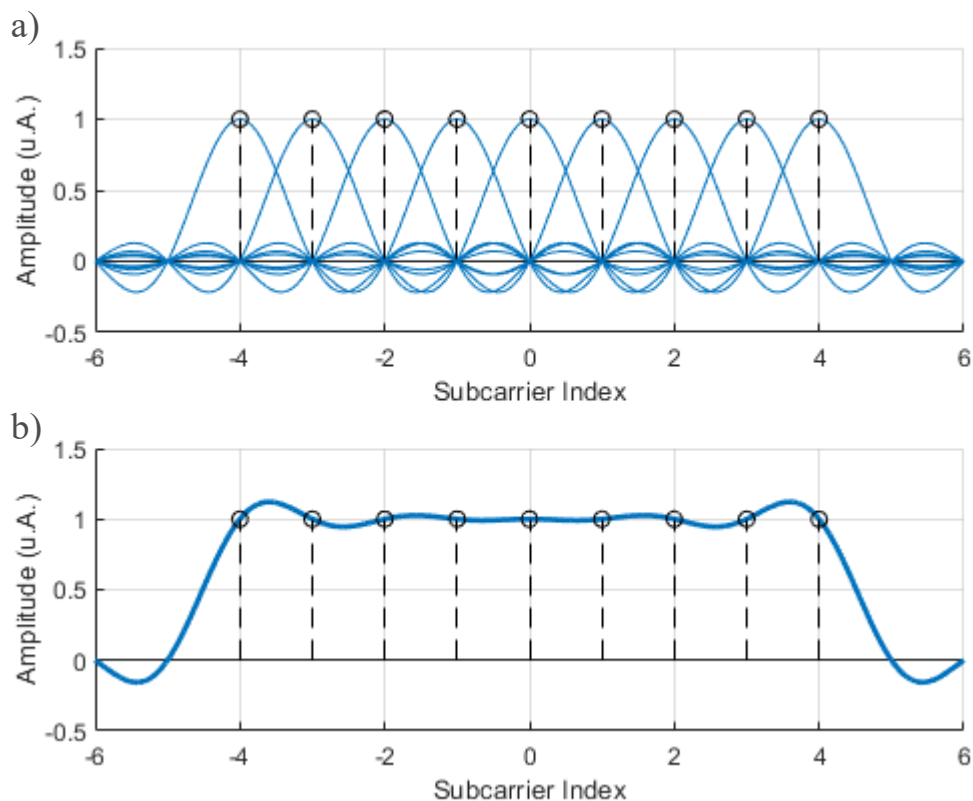
Figure 14 – a) Orthogonality among subcarriers in frequency domain. b) Overall OFDM signal spectrum with the sum of all subcarrier.

During the OFDM demonstration, a discrete-time signal was described with the notation mT. In the following section, we will use only m to refer to a discrete-time signal.

3.1 Cyclic Prefix as Guard Interval

The transmission of OFDM signals in wireless communication channels is susceptible to undesired effects, such as dispersion and multipath fading. Figure 15 illustrates the dispersion effect. In Figure 15. a), a signal $x(t)$ with a duration of T_s is depicted, which, after transmission through the channel $h(t)$, experiences an increase of τ_{max} and is then represented as $y(t)$. The additional time, as depicted by the signal $y(t)$, in a serialized transmission condition of OFDM signals, can lead to the well-known effect called Intersymbol Interference (ISI), impacting the transmission quality. As shown in Figure 15.b), the extra time duration of τ_{max} added to the OFDM signal begins to interfere with the start of the subsequent signal.
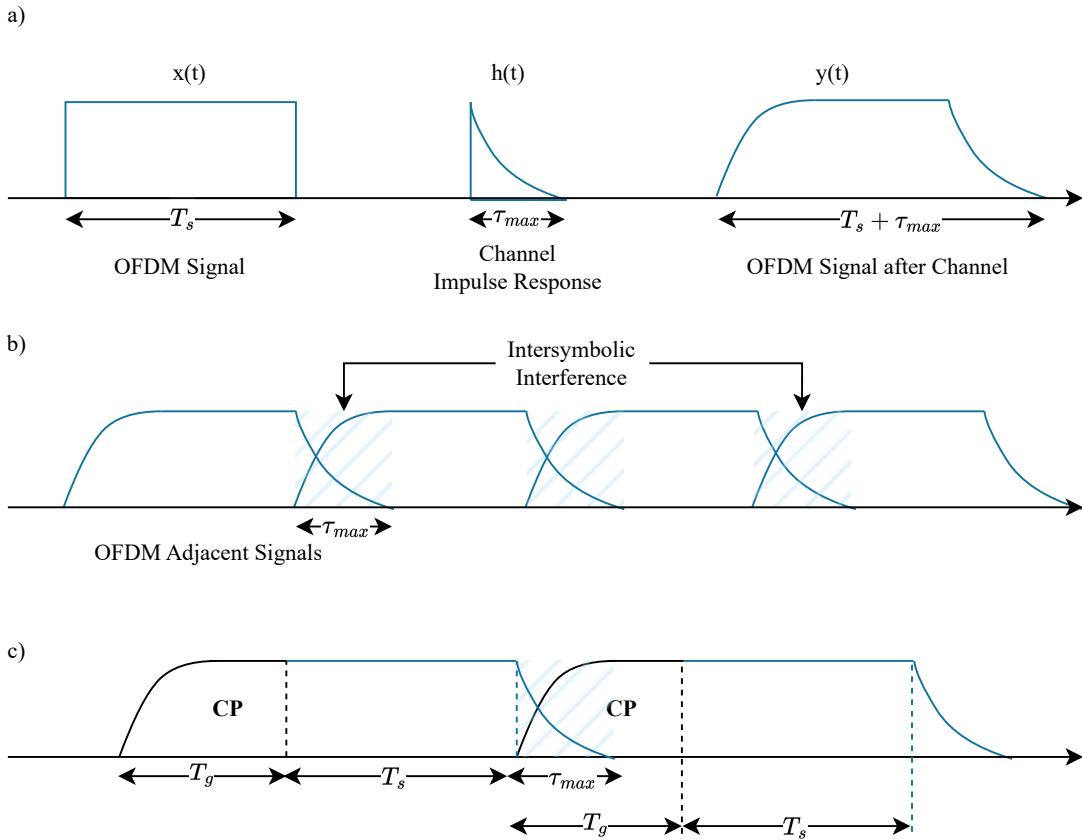
Figure 15 – a) Represents an OFDM signal $x(t)$ before passing through the $h(t)$ channel, and $y(t)$ after passing through the $h(t)$ channel. The $y(t)$ signal is longer than $x(t)$ by a factor of τ_{max}. b) The signal, which has its duration increased by the $h(t)$ channel, is transmitted serially with other extended OFDM symbols, resulting in intersymbol interference. c) A copy of the end of the OFDM signal is inserted at the beginning and intersymbol interference occurs in CP region. The content of the CP is removed, and the useful signal remains unaffected.

To address the ISI issue, a Cyclic Prefix (CP) insertion can be employed [43]. As illustrated in Figure 15 part c), a copy of the end of the symbol is inserted at the beginning of the same OFDM signal. However, to ensure its effectiveness, this copy must

have a duration of T_g which is known as the guard interval. This guard interval should be significantly longer than the maximum possible delay that the channel may introduce to the transmitted signal.

Figure 16 shows a block diagram of a basic OFDM transmitter and receiver. Digital symbol mapping, also known as subcarrier modulation, multiplexing using IFFT, and CP are part of the transmitter. A noise addition is used as model model, and the signal distortion ignored for the sake of simplicity. However, in real systems, reception requires a Time Synchronizer to identify the packet's start and a Frequency Synchronizer to identify the deviation between local oscillators. Subsequently, the operations imposed on the transmitter are reversed, with a special focus on the Fast Fourier Transform (FFT) used for signal demultiplexing [42]. Following this step, channel equalization is performed to accurately recover the transmitted symbols affected by fading and other distortions, thus enabling the retrieval of the bit sequence.
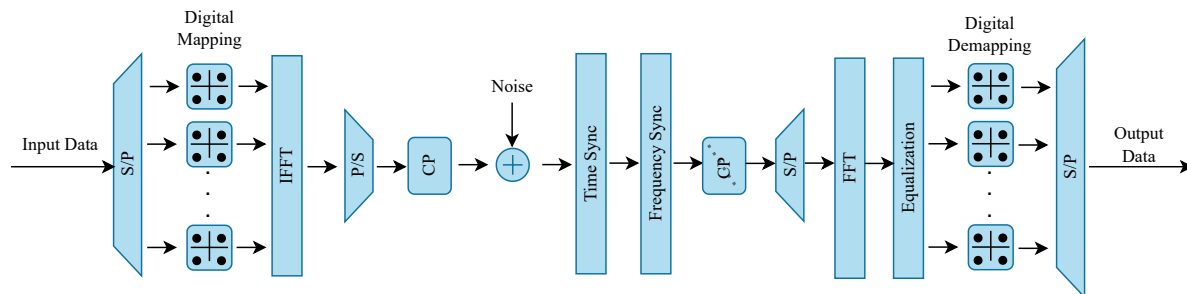
Figure 16 – Basic OFDM transceiver. It commences with a Series-Parallel Converter, which disperses symbols from the Input Data Stream across all subcarriers. Following this, Digital Mapping, which may involve M-PSK or M-QAM, precedes the IFFT responsible for OFDM multiplexing. Subsequently, the Parallel-Series Converter serializes the signal, and finally, the Cyclic Prefix (CP) is inserted. On the receiver side, Time and Frequency Synchronization initiates the process, followed by the removal of the Cyclic Prefix and performing the FFT to retrieve digital symbols. These symbols then undergo equalization to eliminate channel effects and recover the transmitted data. Post equalization, a digital demodulation stage extracts the transmitted bits.

3.2   Time Domain Synchronization

In practical communication systems, the receiver detects a signal that is subsequently converted to baseband by an analog front-end and then sampled by the digital signal processing of a hardware. However, this hardware, that can be a microcontroller or an FPGA, doesn't have precise information about the starting point of, for example, an OFDM frame. To address this inaccuracy, it is necessary to insert a header sequence to perform process of the signal time synchronization, which involves identifying the sample offset from which the OFDM signal recovery begins. A Zadoff-Chu sequence is employed

in 4G LTE to solve the synchronization process, as described in [44] and [45]. The 5G NR adopts a similar concept [46], in which a m-sequence with 127 subcarriers is utilized to identify the start of the OFDM symbol in Downlink. On the other hand, for Uplink the 5G NR adopts the conventional Zadoff-Chu sequence as used in 4G LTE.

Conventionally, the Downlink utilizes a Primary Synchronization Symbol (PSS) for time synchronization. As outlined in the 3GPP specification [47], the m-sequence utilized for time synchronization in 5G NR is specified in Section 4.3.3.1.1. Conversely, for the Uplink, a signal known as the Sounding Reference Signal is employed. This Zadoff-Chu sequence,aids in identifying the frame start as detailed in Section 4.3.3.4. The m-sequence and Zadoff-Chu sequences represent distinct types of signal sequences used in wireless communication. The binary m-sequence is generated through a linear feedback shift register, offering valuable pseudo-random characteristics for spread spectrum and synchronization purposes [48]. Conversely, Zadoff-Chu sequences, complex in nature, serve communication systems by providing robust autocorrelation traits, low cross-correlation interference, and reliable channel estimation properties. These sequences provide significant utility in OFDM-based systems like 5G NR [49], specifically in the generation of Sounding Reference Signals (SRS) and addressing synchronization requirements due to their advantageous properties suited for modern communication needs.

In 5G NR, to locate the beginning of the OFDM symbol, the m-sequence/Zadoff-Chu sequence is also used. This sequence is transformed into an OFDM signal through IFFT multiplexing procedure, creating a reference synchronization signal. Subsequently, a cross-correlation is performed between the received signal and the created reference signal. The identified highest peak of correlation indicates the initial sample of the received OFDM signal. More details is available in the example of the Figure 30.

3.3 Frequency Synchronization

Commonly, transmitters and receivers have different local oscillators (LOs), each with its own accuracy. Some Software Defined Radios have a local oscillator accuracy of 2.5 PPM [50]. Thus, if the system central frequency is 2.4 GHz, the maximum offset deviation can be described as 3.8:

$$f_{omax} = \frac{f_c \times PPM}{10^6} = \frac{2.4 \times 10^9 \times 2.5}{10^6} = 6 \text{ kHz}, \tag{3.8}$$

where f_{omax} is the maximum frequency offset, f_c is the central carrier frequency and PPM is the LO frequency accuracy. Considering a received signal $r(m)$ after the time synchronization process, and that this signal has f_o frequency offset. Mathematically, it is possible to describe the received signal as eEquation 3.9:

$$r(m) = s(m)e^{j2\pi f_o m}. \tag{3.9}$$

To remove the f_o component, a kind of search mechanism should be conducted aiming at a frequency correction. Applied to the signal $r(m)$ using Equation (3.8), it eliminates the frequency offset according to the following Equation 3.10:

$$r(m) = s(m)e^{j2\pi f_o m}e^{j2\pi f_{oc}m} = s(m)e^{j2\pi m(f_o + f_{oc})}. \tag{3.10}$$

The objective of frequency offset correction is to determine a value for f_{oc} that nullifies the influence of f_o. In essence, $f_{oc} + f_o = 0$, indicating that $f_{oc} = -f_o$. The search process can be executed via Pearson's cross-correlation. This approach relies solely on the PSS_{ref} signal, a primary synchronization signal transformed into an OFDM reference signal through IFFT. The cross-correlation between two variables can be defined as follows 3.11 [51]:

$$\rho(A, B) = \frac{1}{N-1}\sum_{i=1}^{N}\left(\frac{A_i - \mu_A}{\sigma_A}\right)\left(\frac{B_i - \mu_B}{\sigma_B}\right) \tag{3.11}$$

where N represents the number of elements in A and B signals, μ_A and σ_A are the mean and standard deviation of the variable A and μ_B and σ_B are the mean and standard deviation of the variable B. Note that the calculation in Equation (3.11) can be time-consuming until the desired correction frequency f_{oc} is found. To make the search non-exhaustive, the f_{oc} will be divided into two stages. The first stage is referred to as coarse frequency offset f_{CFO}, and the second stage as fine frequency fffset f_{FFO}, such that $f_{oc} = f_{CFO} + f_{FFO}$, for

$$f_{CFO} = \max\left(\rho\left(PSS_{ref}, r(m)e^{-j2\pi f_i}\right)\right)$$
$$f_i = [-10000 : 1000 : 10000]. \tag{3.12}$$

where f_i varying within the range shown in Equation 3.12 indicates a search between -10000 and 10000 Hz with a search step of 1000 Hz. These values align with the result obtained in Equation 3.8, where a variation in the local oscillator of 2.5PPM results in a carrier frequency variation of 6KHz. In this initial adjustment stage, coarse adjustment is performed, followed by fine adjustment of the carrier phase correction at the receiver. After determining the correction frequency f_{CFO}, the fine adjustment of the estimated frequency is carried out. During this stage, the search for f_{FFO} is conducted in a manner very similar to what was presented in Equation (3.12). The f_{FFO} is then calculated as:

$$f_{FFO} = \max\left(\rho(PSS_{ref}, r(m)e^{-j2\pi(f_{CFO}+f_j)})\right)$$
$$f_j = [-1000 : 5 : 1000]. \tag{3.13}$$

In the second stage of frequency correction, fine-tuning is applied. Implementing the correction in two stages reduces the number of calculations at the receiver. After finding the adjustment value within the larger range, a search for the detailed value within the smaller variation search space is conducted, thereby avoiding exhaustive searching within the range of values from -10000Hz to 10000Hz. The final received signal after two stages of frequency correction $r_{fc}(m)$ is obtained as:

$$r_{fc}(m) = r(m)e^{-j2\pi(f_{CFO}+f_{FFO})}. \tag{3.14}$$

3.4 Channel Estimation and Equalization

Consider the discrete-time sampled received $r(m)$, and for simplicity consider no additional corrections of time and frequency were needed. Moreover, let $r(m)$ be denoted as Equation 3.15:

$$r(m) = h(m) * s(m) + v(m), \tag{3.15}$$

for $h(m)$ the channel discrete impulse response and $v(m)$ the noise added to the transmitted signal. Performing the Fourier Transform in both sides of Equation 3.16 allows the received signal in frequency domain:

$$R(k) = H(k) \cdot S(k) + V(k) \tag{3.16}$$

where $R(k)$, $H(k)$, and $V(k)$ denote $r(m)$, $h(m)$, and $v(m)$ in the frequency domain, respectively. The equalization process involves determining a filter $w(m)$ such that $w(m) * h(m) = \delta(m)$ or, in the frequency domain, $W(k)H(k) = 1$ [52]. Hence, it can be assumed that:

$$\begin{aligned} \tilde{S}(k) &= W(k)R(k), \\ \tilde{S}(k) &= W(k)H(k)S(k) + V(k)W(k) \end{aligned} \tag{3.17}$$

Therefore the $W(k)$ filter used to equalize the modulated symbols can be obtained as proposed in Equation 3.18:

$$W(k) = H^{-1}(k) = W_{ZF}(k), \tag{3.18}$$

in which the term $W_{ZF}(k)$ is often known as the Zero-Forcing Equalizer [53]. It is anticipated that this equalizer can efficiently alleviate channel distortion by applying the inverse channel response to the detected symbols. However, it's crucial to note that $W(m)$, as defined in

Equation (3.17), does not eliminate the noise component. In scenarios where $|H(m)|^2 \approx 0$, the equalizer might even amplify the noise.

To deal with the fact of the noise component enhanced by the ZF Equalizer an alternative approach is worth considering. The Minimum Mean Square Error (MMSE) Equalizer takes into account the noise variance σ^2 to mitigate the noise component [52]. Equation (3.19) illustrates the transfer function of the MMSE equalizer filter as

$$W_{MMSE}(k) = \frac{H^*(k)}{|H(k)|^2 + \sigma^2}. \tag{3.19}$$

The estimation of the channel transfer function is a crucial task. A common approach involves using training symbols, known as pilots, which modulate the subcarriers of the OFDM signal. Through these symbols, it is possible to estimate a channel response using the following Equation 3.20:

$$\tilde{H}_p(k) = \frac{Y_p(k)}{X_p(k)}. \tag{3.20}$$

The term $H(m)$ can be replaced by its estimated version $\tilde{H}_p$ in Equations (3.18) and (3.19). To obtain the noise variance, the recovered symbols $\tilde{S}(k) - X_p(k)$ is employed by performing the variance calculation operation using Equation (3.21) according to [54]

$$\sigma^2 = \frac{1}{NNp} \sum_{i=1}^{N} |X_p(k) - \tilde{S}_{ZF}(k)|^2, \tag{3.21}$$

where N is the total amount of subcarriers, N_p is the number of pilots and $\tilde{S}_{ZF}$ is the symbols recovered using a Zero Forcing equalizer. Hence, it is clear that the MMSE equalizer has significantly higher complexity compared to the ZF equalizer. This is because the MMSE equalizer initially needs to apply the ZF to obtain the noise variance. This observation highlights a trade-off between performance and complexity.

4 Fundamental Concepts of 5G New Radio

The technical specifications of 5G aim to meet the requirements established by the International Telecommunication Union Radiocommunication Sector (ITU-R) for International Mobile Telecommunications (IMT 2020). Key Performance Indicators (KPIs) for 5G include Enhanced Mobile Broadband (eMBB), Ultra-Reliable Low Latency Communications (URLLC), and Massive Machine Type Communications (mMTC) [55]. However, achieving these KPIs required several strategies, such as utilizing the FR1 bands (below 6 GHz) and the FR2 band (24.25 to 52.6 GHz), along with channels featuring bandwidths ranging from 5 MHz to 400 MHz. A parameter known as numerology provides the necessary flexibility to operate across such distinct frequency bands and with varying bandwidths.

Mathworks provides the 5G Toolbox, offering standard-compliant functions and reference examples for modeling, simulating, and verifying 5G New Radio (NR) and 5G-Advanced communication systems. With the toolbox, it's possible to configure, simulate, measure, and analyze end-to-end 5G NR communication links. Additionally, its possible to modify or customize the toolbox functions and utilize them as reference models for implementing 5G systems and devices [56]. This toolbox was utilized to implement transport and physical channels during the project development.

4.1 Numerology and Slot Format

The 3GPP 5G New Radio has specified the numerology parameter since Release 15. Numerology, in turn, defines the frequency spacing between subcarriers (SCS), the size of the cyclic prefix (CP), and the size of slots. The need for multiple numerology becomes evident as, in channels with frequencies below 6 GHz, bandwidths are narrower. In such cases, increasing the number of subcarriers can enhance the spectral efficiency of the OFDM format, making it advantageous to use a smaller SCS. However, using a lower SCS results in longer symbol duration, which, in turn, increases the size of the cyclic prefix. This makes the OFDM signal less susceptible to multipath fading issues [57], but at the cost of increased latency. In higher operation frequencies like millimeter waves (mmWaves), the Doppler Spread effect is significant [58], and to minimize its impact, it is more advantageous to use a higher SCS. For the 5G NR there is a relationship between numerology and subcarrier spacing as shown in Equation (4.1):

$$SCS = 2^{\mu} \times 15 \quad [\text{kHz}] \tag{4.1}$$

where μ represents the numerology. Figure 17 shows an example of the variation in subcarrier spacing. For this illustration, it was used a set of 12 subcarriers, as this is the number of subcarriers that make up a Resource Block (RB). In Figure 17.a), is presented the RB for a spacing of 15 kHz, resulting in an occupancy of 180 kHz. Parts b), c), and d) of Figure 17 show variations for 30 kHz, 60 kHz, and 120 kHz. Furthermore, there are options for spacing of 240 kHz, 480 kHz, and 960 kHz to be used in mmWaves scenarios.
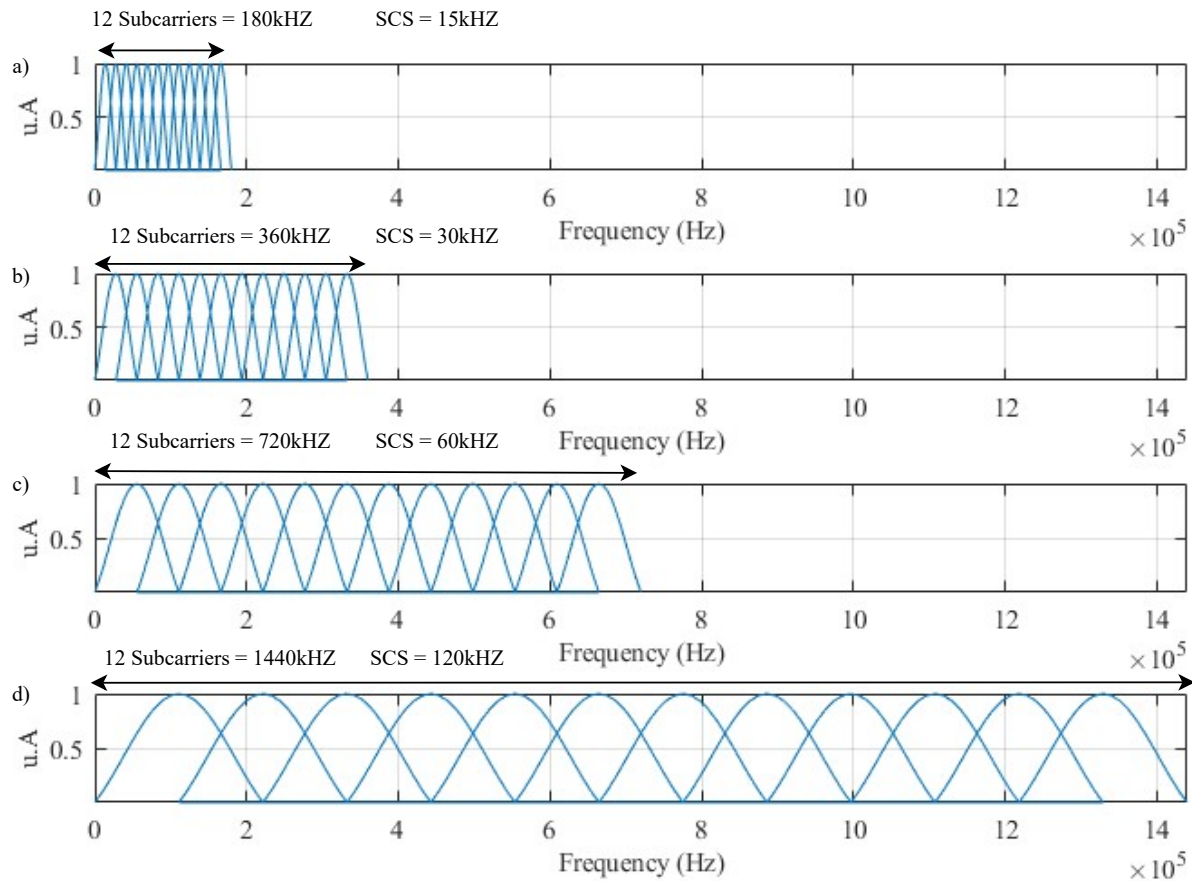
Figure 17 – a) Spectrum allocation for a Resource Block with SCS = 15kHz. b) with SCS = 30kHz. c) SCS = 60kHz. d) SCS = 120kHz.

In 5G NR, the time slot is a unit of time that subdivides the signal frame. Each time slot represents the time interval during which 14 symbols can be transmitted [59]. Due to the various numerologies that define the values of subcarrier spacing, there will be different durations for the time slots. Increasing the Subcarrier Spacing results in a larger bandwidth for a single RB (12 subcarriers) allocation. However, as shown in Figure 18, the effect in the time domain is the opposite. As the subcarrier spacing increases and, consequently, the bandwidth expands, the symbols become shorter in the time domain, i.e., faster. This contributes in the reduction of latency.

The frame structure is illustrated in Figure 19a), each frame can be segmented into 10 subframes, each with a duration of 1ms, totaling 10ms for the entire frame. These subframes are further divided into slots, as depicted in parts b), c), and d), showcasing
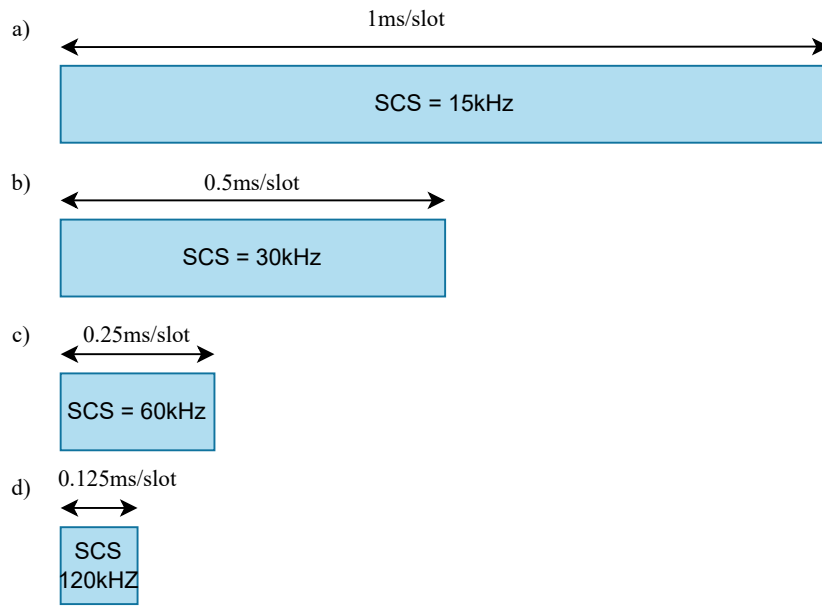
Figure 18 – a) For a subcarrier spacing SCS = 15 kHz the slot duration is 1 ms. b) shows the slot duration of 0.5 ms with an SCS = 30kHz. c) and d) shows the duration of the time slot for SCS = 60kHz and SCS = 120kHz, respectively.

the subdivision into 1, 2, 4, and 8 slots, respectively. Additionally, the division of each slot into 14 symbols is displayed. The symbol mappings can be QPSK, 16QAM, 64QAM, or 256QAM, all representing square constellations. Table 1 summarizes the parameters in terms of Subcarrier Spacing, OFDM symbol duration, Cyclic Prefix duration, slots in subframe, and slot duration for the numerology values available in 5G NR standard.

Numerology	$\mu = 0$	$\mu = 1$	$\mu = 2$	$\mu = 3$	$\mu = 4$
SCS (kHz)	15	30	60	120	240
OFDM symbol duration (μs)	66.67	33.33	16.67	8.33	4.17
CP duration (μs)	4.8	2.4	1.2	.6	0.3
Slots in subframe	1	2	4	8	16
Slot duration (μs)	1000	500	250	125	62.5

Table 1 – Summary of the parameters associated with each numerology value.

4.2   Resource Grid Concepts

The Resource Grid is defined as a matrix of time and frequency resources, as described in [60]. It plays a fundamental role in allocating resources for all physical layer channels in 5G NR. Figure 20 highlights the basic unit known as the Resource Element. Each Resource Element represents a digital symbol mapped by a subcarrier of the OFDM signal, as specified in [47]. Additionally, in the Figure 20, the presence of a Resource Block is highlighted, which is a set of 12 sequential subcarriers in the frequency domain, and the time slot, which contains 14 sequential symbols in the time domain. It is also important to
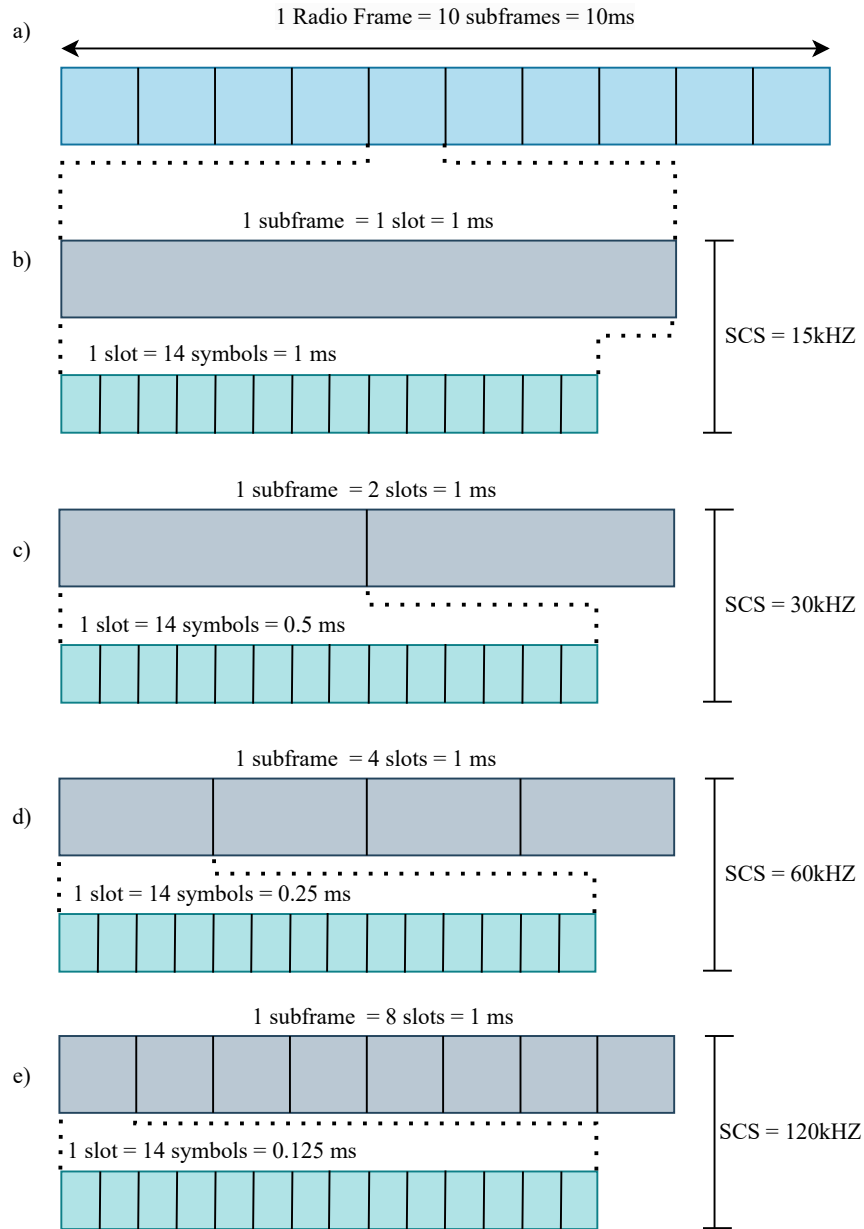
Figure 19 – a) The Radio Frame can be subdivided into 10 subframes, each with a duration of 1 ms. b) With an SCS of 15 kHz, each subframe contains only 1 slot with a duration of 1 ms, which can be subdivided into 14 symbols. c) When the SCS is 30 kHz, the subframe is divided into 2 slots, each with a duration of 0.5 ms, and each slot can hold 14 symbols. d) For an SCS of 60 kHz, the subframe is divided into 4 slots, each with a duration of 0.25 ms, and all of them can accommodate 14 symbols. e) With an SCS of 120 kHz, the subframe is divided into 8 slots, each with a duration of 0.125 ms, and they all contain 14 symbols.

note that in Figure 20, only a segment of the Resource Grid is highlighted. However, the total size of the grid is determined by $N_{RB}^{\mu} N_{SC}^{RB} \times N_{symb}^{slot} N_{slot}^{frame}$, where N_{RB}^{μ} represents the total number of Resource Blocks available in the bandwidth for a μ numerology, N_{SC}^{RB} is the number of subcarriers in each Resource Block, N_{symb}^{slot} is the number of symbols in a slot, and N_{slot}^{frame} denotes the number of slots in the Frame. The complete $N_{RB}^{\mu} N_{SC}^{RB} \times N_{symb}^{slot} N_{slot}^{frame}$

Resource Grid corresponds to the Radio Frame illustrated in Figure 20.
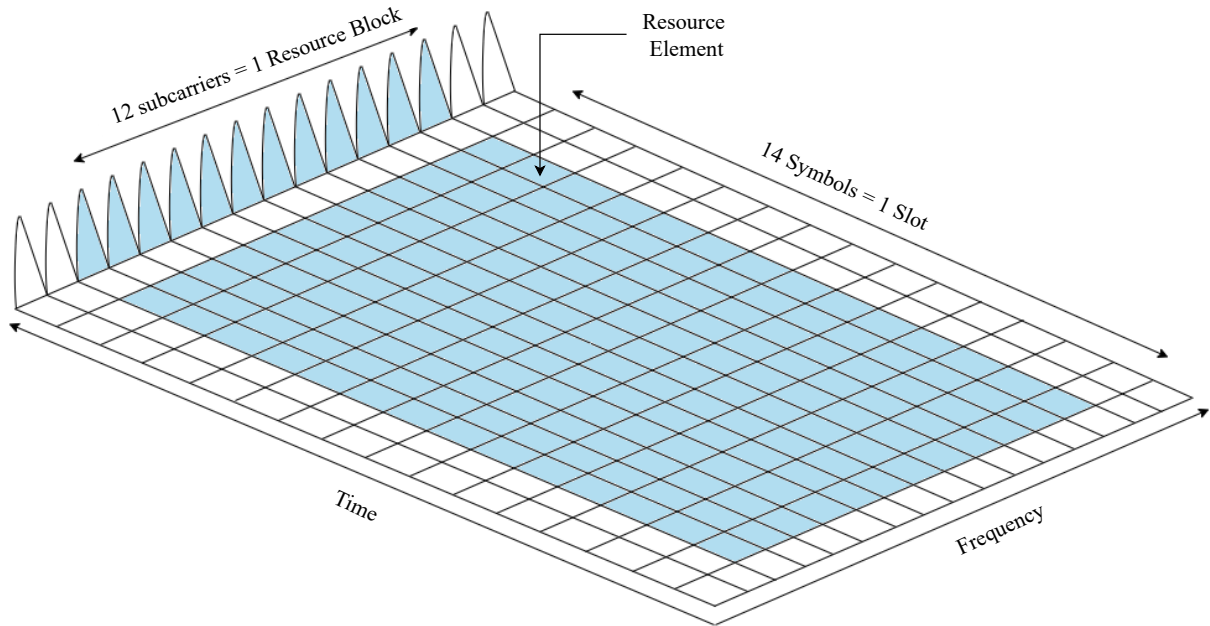
Figure 20 – A Resource Grid is a matrix of time and frequency. The most basic unit of the Resource Grid is called a Resource Element, which comprises a digital symbol modulating an OFDM subcarrier.

The Resource Grid varies for each frequency spacing defined by different numerologies, meaning that different Subcarrier Spacing (SCS) values should not be mixed within the same Resource Grid. To accommodate various numerologies, the approach involves partitioning the entire channel bandwidth into multiple dedicated Resource Grids, each corresponding to a specific numerology.

In a typical 5G New Radio Mobile system, the RF communication channel is shared for both Downlink and Uplink flows. This shared channel entails a directional allocation of slot-symbols within a time slot [61], with certain slot-symbols allocated for Downlink and others exclusively for Uplink. This scenario is known as Time Division Duplex (TDD). Alternatively, another approach, known as Frequency Division Duplex (FDD), involves the exclusive use of certain subcarriers for Downlink and others for Uplink. Moreover, in a conventional 5G system, Resource Elements are allocated to facilitate multiple users accessing the medium, a technique known as Orthogonal Frequency Division Multiple Access (OFDMA). However, for simplicity, in the prototype examined in this study, only one user is allocated for transmission in both the Uplink and Downlink.

The 3GPP still specifies, according to [62], the quantity of Resource Blocks for each communication channel bandwidth and subcarrier spacing. The allocations of Resource Blocks for the FR1 frequency can be observed in Table 2. Following the specification for a 5 MHz bandwidth, it is noted that only SCS = 15 kHz is available. Upon analyzing the Table 2 it is evident that for SCS = 15 kHz, the effectively utilized bandwidth is

$12 \times N_{RB} \times 15$ kHz $= 12 \times 25 \times 15$ kHz $= 4.5$ MHz. This implies that 500 kHz of bandwidth has not been allocated. This unallocated range is referred to as the Guard band, with 250 kHz before the signal and 250 kHz after it.

SCS (kHz)	Channel Bandwidth			
	5 MHz N_{RB}	10 MHz N_{RB}	15 MHz N_{RB}	20 MHz N_{RB}
15	25	52	79	108
30	11	24	38	51
60	N/A	11	18	24

Table 2 – Summary of Number of Resource Blocks associated to Channel Bandwidth and Subcarrier spacing

4.3   New Radio Channels

The 5G NR specification incorporates a hierarchy structured around a protocol stack, as illustrated in Figure 21. Data channels serve as pathways that interconnect the layers of the 5G stack. To begin with, it is crucial to understand the functionalities of each layer [63]:

RLC (Radio Link Control) encompasses functionalities such as automatic retransmission, flow control, and data segmentation/desegmentation, aiming to optimize the efficiency and reliability of wireless communication. Within the context of 5G NR, RLC is paramount in ensuring effective and secure data transmission in next-generation networks.

Medium Access Control (MAC) is responsible for managing the use of radio resources. In 5G, the MAC layer supports functions such as dynamically allocating resources, controlling access, and managing quality of service (QoS). Serving as a bridge between the PHY and link (RLC) layers, the MAC layer facilitates smooth communication within the 5G framework.

The physical layer receives data from the transport layer and maps it onto the radio interface. Specifically, it inserts the data into the Resource Grid for transmission over the radio interface.

Figures 22 and 23 show all channels involved in both the Downlink and Uplink. These channels are categorized into three distinct types: Logical, Transport, and Physical. It is important to highlight that in the graphical representation, specific channels are emphasized in blue, indicating their were implemented in the prototype. These channels play a crucial role in the User/Traffic Plane, responsible for transmitting data to users [64]. Therefore, the implementation focused on channels that constitute the actual infrastructure for communication with end-users. On the other hand, the remaining channels constitute the Control Plane, performing crucial functions related to identification, paging, and access
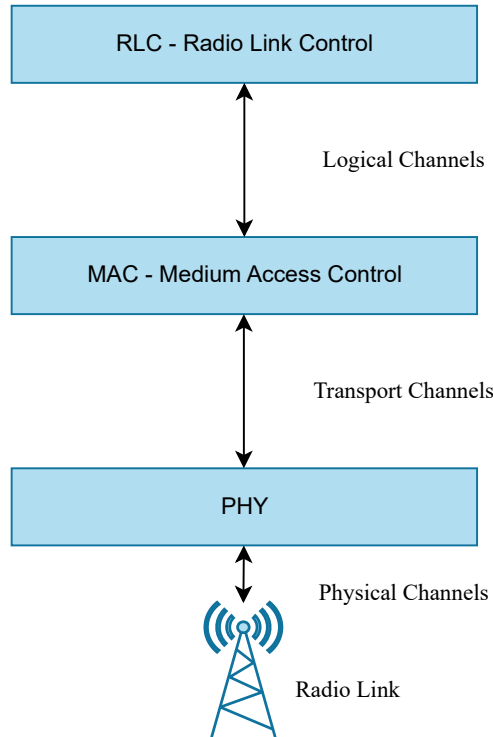
Figure 21 – 5G Stack. RLC, MAC and PHY are layers and Channels is the way to transfer information among these layers
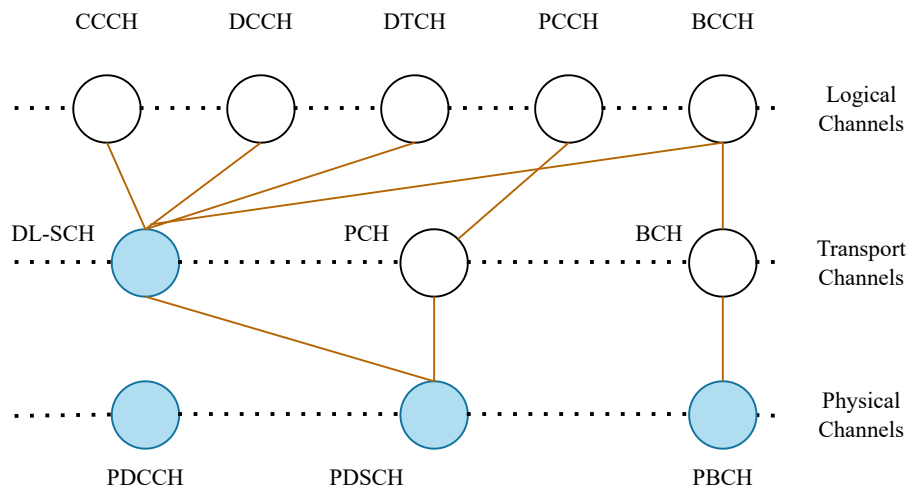
Figure 22 – Downlink Logical, Transport and Physical channels, the channels filled in blue have been implemented in the project.

to the 5G network. This distinction between planes highlights the complexity and diversity of functions performed by different channels in the communication architecture under consideration.
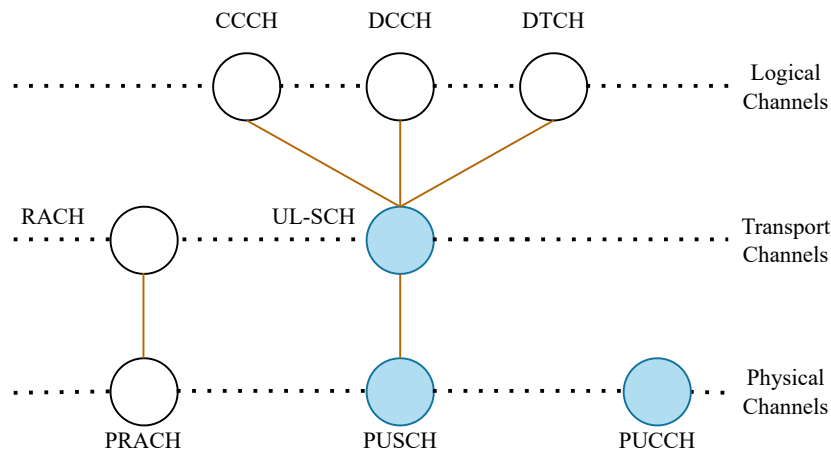
Figure 23 – Uplink Logical, Transport and Physical channels, the channels filled in blue have been implemented in the project.

4.3.1 Logical Channels

Logic Channel: it is a collection of information that identifies what type of data is being carried [60]. Logic channels are often identified by the type of information they carry: control channel or traffic channel. While control channels are used to transfer data from the control plane, traffic channels are used to transfer information from the User plane. There exists five types of Logic Channel as illustrated in Figure 22, observes that the logical channels are also used in Uplink channels as shown in Figure 23.

In a subdivision Control Channels are BCCH, PCCH, CCCH, DCCH and Traffic Channel is only DTCH. Below here is a summary of the main assignments of each logical channel [65].

BCCH (Broadcast Control Channel): Employed for broadcasting system control information, such as Master Information Block (MIB) and System Information Block (SIB). It is transmitted from the network to all mobile terminals within a cell. Before accessing the system, a terminal needs to acquire system information to understand its configuration and behavior within a cell.

PCCH (Paging Control Channel): Used to locate users whose cell-level location is unknown, i.e., those users in an idle state. The PCCH channel is transmitted across multiple cells.

CCCH (Common Control Channel): A point-to-multipoint channel typically utilized for transferring control information between the network and the UE before the establishment of the RRC connection.

DCCH (Dedicated Control Channel): A point-to-point channel used for the dedicated transmission of control information between the mobile device and the network. This channel is employed for the individual configuration of terminals, such as in handover

procedures.

DTCH (Dedicated Traffic Channel): Dedicate to carrying useful data from users for a point-to-point connection with the network.

4.3.2   Transport Channels

Transport channels are provided by the Physical (PHY) layer to the Medium Access Control (MAC). The MAC layer multiplexes one or more logical channels onto a transport channel. While logical channels define the content being conveyed, transport channels specify how they are transported. They establish the method of carrying information, encompassing aspects such as encoding, error protection, and CRC (Cyclic Redundancy Check). Below there are a little summary about Transport channels [60].

DL-SCH (Downlink Shared Channel): The Downlink shared transport channel is responsible for transmitting Downlink data to multiple mobile devices simultaneously, ensuring efficient delivery of information.

PCH (Paging Channel): This channel is used to send paging information, being essential to locate mobile devices that are in an idle state.

BCH (Broadcast Channel): The broadcast transmission channel is responsible for transmitting crucial information to all devices in the cell, such as the Master Information Block (MIB), essential for the initial device configuration.

RACH (Random Access Channel): The random access channel is used for the initial communication between mobile devices and the base station, facilitating random access to the network.

UL-SCH (Uplink Shared Channel): This channel is responsible for transmitting Uplink shared data from various mobile devices, ensuring efficient transmission of information in the Uplink direction.

These channels play specific roles in the 5G NR communication architecture, ensuring effective and efficient data transmission in both Downlink and Uplink directions.

4.3.2.1   Downlink/Uplink Shared Channel - DL/UL-SCH

The encoding process chain is the same for Downlink (DL-SCH) and Uplink (UL-SCH) transport channels. Figure 24 provides an overview of the process [66]. Firstly, in Figure 24 a), it can be observed that a Transport Block is constructed, defined as a sequence of bits to be encoded. Initially, this Transport Block is protected by error checking through a first CRC. In Figure 24 part b), it is noted that the Transport Block is segmented into several Code Blocks, and each Code Block receives a respective CRC for its sequence. Moving forward in part c), the bits of the Code Block + CRC goes to
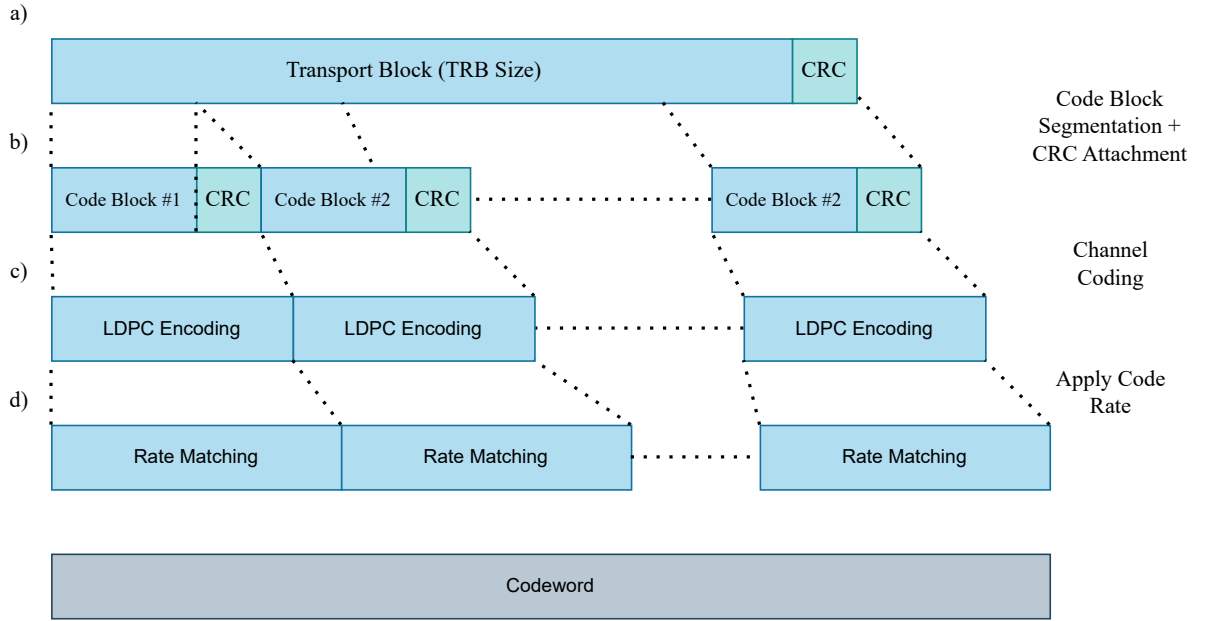
Figure 24 – Downlink/Uplink Process Chain: a) Begin by attaching the CRC to the Transport Block. b) Subsequently, divide the Transport Block + CRC into Code Blocks and attach a second CRC. c) Proceed with LDPC encoding. d) Apply the code rate to create a codeword that the specified PDSCH length.

encoding process using a method known as Low-Density Parity Check (LDPC). Finally, in part d), Rate Matching is demonstrated, ensuring that the codeword contains exactly the same number of elements available in the PDSCH/PUSCH.

4.3.2.1.1 Transport Block Size Calculation and CRC

The method to calculate the Transport Block Size is described in [67]. First step is find the estimated number of resource elements allocated in PDSCH Resource Blocks N'_{RE} as described in Equation 4.2.

$$N'_{RE} = N_{SC}^{RB} \times N_{symb}^{slot} - N_{DMRS}^{PRB} - N_{oh}^{PRB} \qquad (4.2)$$

where N_{SC}^{RB} is the number of subcarriers per RB and its normally 12, N_{symb}^{slot} is the number of the symbols allocated within slot, N_{DMRS}^{PRB} is the number of resource elements used to reference signal dedicated to channel estimation in the PDSCH resource grid and N_{oh}^{PRB} is a high layer parameter $= [0, 6, 12, 18]$ and for all experiments was used to zero. Next step determine the total number of Resource Elements N_{RE} as given in Equation 4.3.

$$N_{RE} = min(156, N'_{RE}) \times n_{PRB} \qquad (4.3)$$

where n_{PRB} is the total number of Physical Resource Blocks allocated to the UE receives. In the project case as discussed the VLC channel is exclusive to the Downlink and Radio

Frequency signal is exclusive for the Uplink, in this case n_{PRB} is the total Number of Resource Blocks available for the numerology and bandwidth.

Finally, Equation 4.4 is utilized to calculate the intermediate number of information bits, taking into account the number of Resource Elements.

$$N_{info} = N_{RE} \times R \times Q_m \times \nu \tag{4.4}$$

where R represents the code rate proportion, Q_m denotes the digital modulation order, and ν stands for the number of antenna layers. In both Downlink and Uplink, only one layer was utilized, consisting of a single LED and a single antenna. Upon calculating N_{info}, the final step involves implementing the algorithm outlined in Figure 25. The MATLAB 5G NR Toolbox is equipped to compute the Transport Block Size (TBS), as elaborated in [68]. Essentially, the function nrTBS takes parameters from Equation 4.4 and returns the Transport Block Size. Once the Transport Block size is determined, obtaining an equivalent-sized sequence of bits becomes necessary. Subsequently, the CRC of the sequence is applied, as depicted in Figure 24, part a). In this context, the CRC can have values of 16 or 24 bits. If the DL-SCH or UL-SCH size exceeds 3824, a 24-bit CRC is utilized.

4.3.2.1.2 Code Block Segmentation and CRC

To calculate the size of the Code Block, it is necessary to first establish a relationship between the size of the Transport Block and the coderate. This relationship is defined as a base graph. Figure 26 illustrates the division of possible values for TBS (Transport Block Size) and R into two distinct zones called Base Graph 1 and Base Graph 2. From there, the sizes of the Code Blocks can be obtained [69]. After Code Block division is attached a CRC with 24 bits based on the same premises than the CRC of full Transport Block. Equation 4.5 shows the K_{CB} size for the two different base graph.

$$K_{CB} = \begin{cases} 8448, & For\,Base\,graph\,type\,1 \\ 3840, & For\,Base\,graph\,type\,2 \end{cases} \tag{4.5}$$

4.3.2.1.3 LDPC Channel Coding

The 3GPP specification defines the utilization of LDPC channel encoding for transport channels within the realm of 5G, while Polar encoding is employed for control channels [69]. Although the theory of channel encoding extends beyond the scope of this work, the practical implementation was executed using the 5G NR toolbox in Matlab, as detailed in [70]. However, for a more comprehensive understanding of the topic, a brief introduction will be provided here.

$N_{info} \leq 3824$

NO

YES

$n = [log_2(N_{info} - 24] - 5$

$$N'_{info} = 2^n round\left(\frac{N_{info} - 24}{2^n}\right)$$

$$N'_{info} = max\left(24, 2^n \times \left[\frac{N_{info}}{2^n}\right]\right)$$

Determine TBS based on
TS38.214

YES

$R \leq 1/4$

NO

$$TBS = 8 \times C \times \left[\frac{N'_{info} + 24}{8 \times C}\right] - 24$$

$$C = \left[\frac{N'_{info} + 24}{3816}\right]$$

NO

$N'_{info} \geq 8424$

YES

$$C = \left[\frac{N'_{info} + 24}{8424}\right]$$

$$TBS = 8 \times \left[\frac{N'_{info} + 24}{8}\right] - 24$$

$$TBS = 8 \times C \times \left[\frac{N'_{info} + 24}{8 \times C}\right] - 24$$
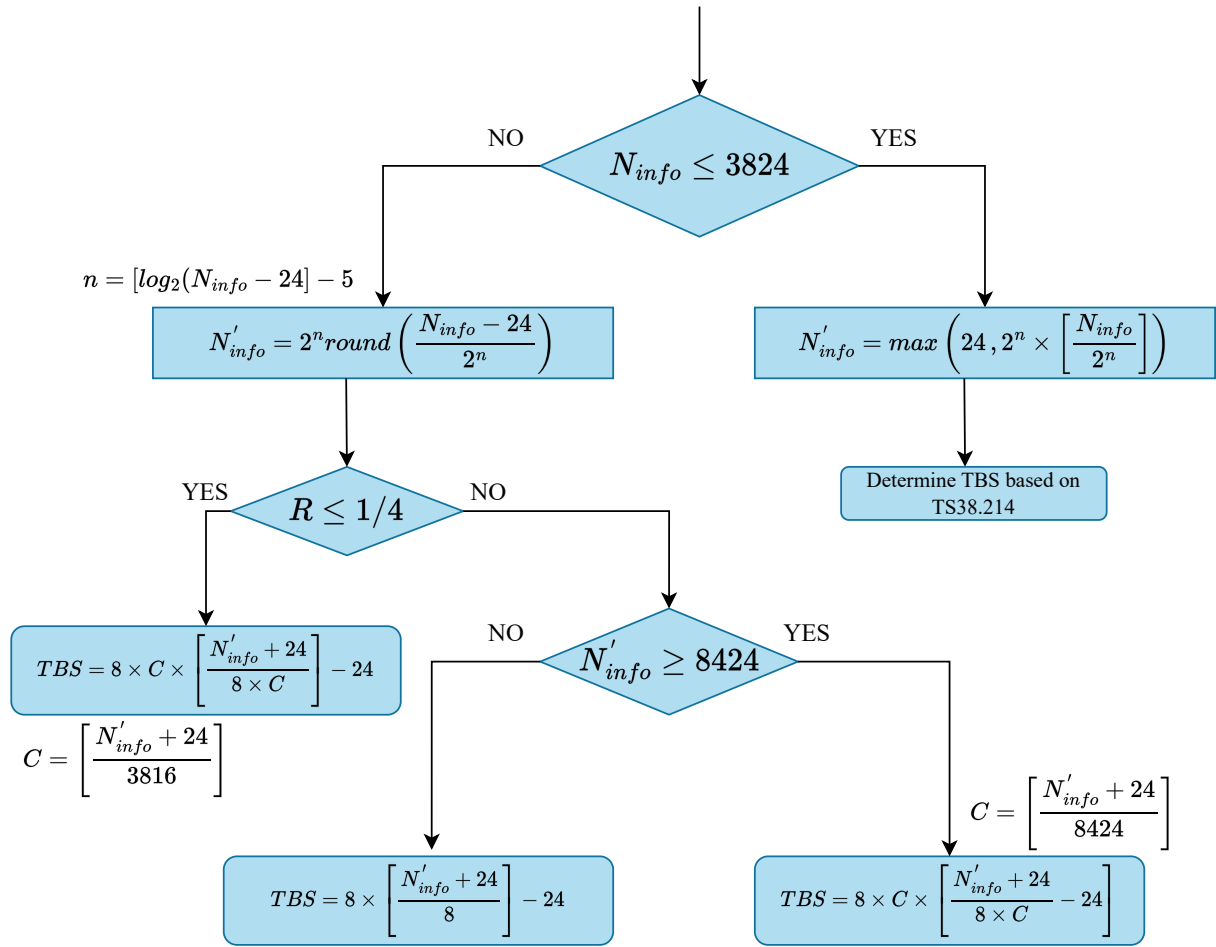
Figure 25 – Algorithm to calculate the Transport Block Size (TBS) after used equations
4.2-4.4.

.
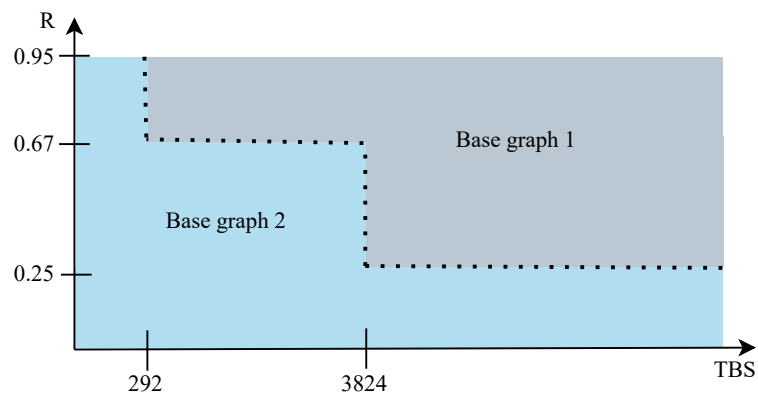
Figure 26 – Base graph division considering Transport Block Size and Target Code Rate

The LDPC has two fundamental approaches, first one is based on parity check matrix H and the second one based on the Tunner Graph [71]. Consider a set of databits d_i arranged in a 2×3 structure and protected by parity bits p_i both horizontally and vertically as disposed in Table 3. The parity bits is obtain by the XOR boolean operation, for instance for a row $p_1 = d_1 \oplus d_2 \oplus d_3$ where $\oplus$ denotes the XOR operation. And for the row $p_3 = d_1 \oplus d_4$. A new codeword is produced with the parity bits, the data bits $(d_1, d_2, d_3, d_4, d_5, d_6)$ formed a new codeword $(d_1, d_2, d_3, d_4, d_5, d_6, p_1, p_2, p_3, p_4, p_5)$.

Data bits			Parity Bits
d_1	d_2	d_3	p_1
d_4	d_5	d_6	p_2
p_3	p_4	p_5	

Table 3 – Distribution of parity and data bits in a table

The matrix H from 4.6 is called the Parity Check Matrix. Each row of matrix H represents one of the parity equations. The columns on the left represent the data bits, while the columns on the right represent the parity bits. The structure of the Parity Check Matrix H is given by the combination $(n - k) \times k$ of the data input matrix C^T and the identity matrix I with k entries, where n represents the final codeword length and k the quantity of data bits. According [60] for a received codeword string $y = (c_1, .., c_n)$ it is valid if and if it satisfies the equation $Hy^T = 0$.

$$H = (C^T|I) = \begin{pmatrix} d_1 & d_2 & d_3 & d_4 & d_5 & d_6 & p_1 & p_2 & p_3 & p_4 & p_5 \\ 1 & 1 & 1 & 0 & 0 & 0| & 1 & 0 & 0 & 0 & 0 \\ 0 & 0 & 0 & 1 & 1 & 1| & 0 & 1 & 0 & 0 & 0 \\ 1 & 0 & 0 & 1 & 0 & 0| & 0 & 0 & 1 & 0 & 0 \\ 0 & 1 & 0 & 0 & 1 & 0| & 0 & 0 & 0 & 1 & 0 \\ 0 & 0 & 1 & 0 & 0 & 1| & 0 & 0 & 0 & 0 & 1 \end{pmatrix} \tag{4.6}$$

From the parity check matrix H, it is possible to derive the generator matrix G by equation 4.7:

$$G = (I|C) = \begin{pmatrix} d_1 & d_2 & d_3 & d_4 & d_5 & d_6 & p_1 & p_2 & p_3 & p_4 & p_5 \\ 1 & 0 & 0 & 0 & 0 & 0| & 1 & 0 & 1 & 0 & 0 \\ 0 & 1 & 0 & 0 & 0 & 0| & 1 & 0 & 0 & 1 & 0 \\ 0 & 0 & 1 & 0 & 0 & 0| & 1 & 0 & 0 & 0 & 1 \\ 0 & 0 & 0 & 1 & 0 & 0| & 0 & 1 & 1 & 0 & 0 \\ 0 & 0 & 0 & 0 & 1 & 0| & 0 & 1 & 0 & 1 & 0 \\ 0 & 0 & 0 & 0 & 0 & 1| & 0 & 1 & 0 & 0 & 1 \end{pmatrix} \tag{4.7}$$

After defining the generation matrix G the channel-encoded codeword can be obtained by combining the data word d_i with G matrix to create the new codeword c,
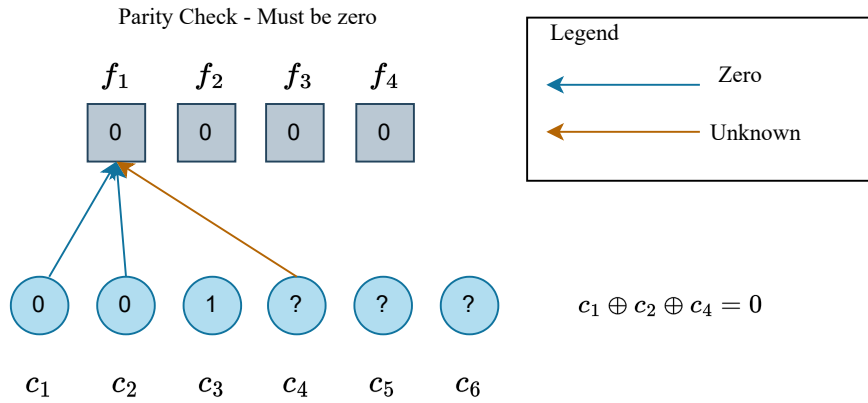
Figure 27 – The first row of Equation 4.9 in the Tanner graph.

where $c = d \cdot G$ (matrix product). With k data bits and a final codeword length with n elements the ratio k/n is defined as coderate. Now for decoding process consider the H matrix (only C^T part) as exemplified in equation 4.8 [60].

$$H = \begin{pmatrix} c_1 & c_2 & c_3 & c_4 & c_5 & c_6 \\ 1 & 1 & 0 & 1 & 0 & 0 \\ 0 & 1 & 1 & 0 & 1 & 0 \\ 1 & 0 & 0 & 0 & 1 & 1 \\ 0 & 0 & 1 & 1 & 0 & 1 \end{pmatrix} \tag{4.8}$$

The reader should observe that the for this example $n = 6$ codeword bits, $k = 2$ data bits and $r = 4$ parity bits then the coderate is $k/n = 2/6$. In the other words, for 6 received encoded bits there exists 4 party check equations, where:

$$\begin{aligned} c_1 \oplus c_2 \oplus c_4 &= 0 \\ c_2 \oplus c_3 \oplus c_5 &= 0 \\ c_1 \oplus c_5 \oplus c_6 &= 0 \\ c_3 \oplus c_4 \oplus c_6 &= 0 \end{aligned} \tag{4.9}$$

As discussed the received codeword is valid when $Hy^T = 0$. Let a received codeword with noise $c_{error} = [0\,0\,0\,?\,?\,?]$. The subsequent process involves recovering the codeword through an iterative procedure visualized as a Tanner graph. Observe in Figure 27 that the code bits from the first row of Equation 4.9 were connected to the parity check f_1. The same process can be carried out for the remaining three rows of Equation 4.9 as proposed in Figure 28.

In Figure 28 (part a), it can be observed that all connections between the code bits have been established up to the outputs f_i. Examining f_1, it is noted that $0 \oplus 0 \oplus c_4 = 0$,
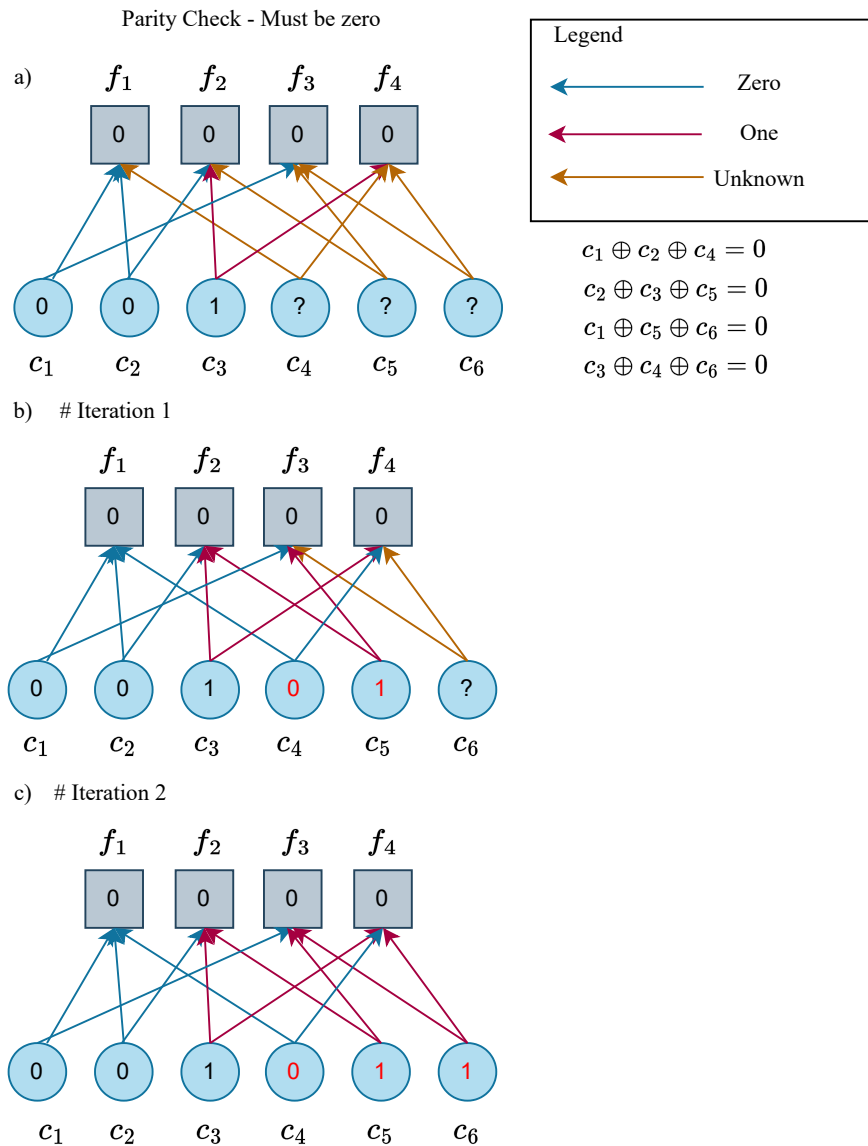
Figure 28 – a) Shows all rows of Equation 4.9 in the Tanner graph. b) The first iteration and discovered c_4 and c_5 coded bits c) after discovered c_4 and c_5 it is possible find c_6 coded bit in a second iteration

indicating $c_4 = 0$. Similarly, for f_2, it is evident that $0 \oplus 1 \oplus c_5 = 0$, leading to $c_5 = 1$. This outcome is then propagated to Figure 28 (part b), where in the second iteration, c_6 is obtained. It is observed that to determine c_6, one must consider both f_3 and f_4. For f_3, it is found that $0 \oplus 1 \oplus c_6 = 0$, and for f_4, $0 \oplus 1 \oplus c_6 = 0$. In this scenario, $c_6 = 1$ resolves both situations, thus completing the validation of the received codeword.

4.3.2.1.4 Rate matching

The final step in the coding scheme of DL/UL-SCH is rate matching. Rate matching is the process by which the transport channel aligns with the physical channel PDSCH/PUSCH length [72]. The rate matching process involves bit repetition and bit

interleaving as discussed in [69] pattern.

After rate matching, the encoding process outlined by the DL/UL-SCH is complete. According to the documentation provided in [73], an object of type nrDLSCH must be instantiated in the implementation. It is important to emphasize that the coderate must be specified, and from the input bit vector, the nrDLSCH instance determines the size of the Transport Block Size. This allows obtaining the size of the CodeBlocks. Additionally, it is specified in the encoding process to inform the size of the output data (outlen), considering additional CRC bits, redundancy bits in the LDPC algorithm, and defining the rate of rate matching. Furthermore, it is important to note that a decoder structure is defined for the DL/UL-SCH. The difference in this case is the necessity to indicate, in addition to the coderate, the size of the TBS for the decoder. The decoder is also capable of performing parity checks and indicating if there were any transmission errors in the received Transport Block.

4.3.3 Physical Channels

Physical channels are responsible for transmitting information across the air interface in wireless communication systems. These channels are directly associated with transport channels. Additionally, there are standalone physical channels that operate independently, not tasked with conveying higher-layer information. Instead, these channels serve specific functions within the broader communication framework. A short summary is described below [60].

PDSCH (Physical Downlink Shared Channel): Ensures the efficient Downlink transmission of shared data to multiple devices simultaneously.

PDCCH (Physical Downlink Control Channel): Facilitates Downlink control information transmission, aiding in configuration and resource allocation.

PBCH (Physical Broadcast Channel): Transmits crucial broadcast information, including the Master Information Block (MIB), to all devices within the cell.

PRACH (Physical Random Access Channel): Supports initial communication between devices and the base station, enabling random network access.

PUSCH (Physical Uplink Shared Channel): Facilitates the Uplink transmission of shared data from multiple devices, ensuring efficient Uplink communication.

PUCCH (Physical Uplink Control Channel): Analogous to PDCCH but in the Uplink direction, conveys control information from devices to the network.

4.3.3.1 Synchronization Signal Block - SSB

The block known as the Synchronization Signal Block occupies 4 consecutive symbols in the Resource Grid and serves several crucial functions [74]:

1) Indicating the start of the frame,

2) Identifying the Cell ID, and

3) Transmitting information from the MIB (Master Information Block).

Although the focus of the work is on transferring data from the User Plane (data payload) rather than the Control Plane, the PBCH was implemented due to its significant role in the synchronization block. The transmission of the MIB is not being used, nor is polar coding for this case; only a random payload is being transferred for simplicity.

The program essentially allocates resources (modulated 5G NR symbols) in an empty Resource Grid. As discussed in Section 4.2, a Resource Grid in terms of software will be a matrix where the rows represent Resource Elements and the columns represent OFDM symbols. According to [75], the Resource Grid will be initialized for a Subcarrier Spacing of 15 kHz and for a bandwidth of 5 MHz, there will be 25 Resource Blocks, hence, there will be a total of 300 Resource Elements. Additionally, for each time slot, there will be 14 OFDM symbols and 10 slots, resulting in a final matrix size of 300x140.

4.3.3.1.1 Primary Synchronization Signal - PSS

As discussed in Session 3.2 PSS is used to detect the time start offset from a signal acquired and sampled. As proposed before [47] the m-sequence sequence used for time synchronization in 5G NR is defined in Equation 4.10:

$$d_{PSS}(n) = 1 - 2x(m) \qquad (4.10)$$

where the m-value is denoted by Equation 4.11:

$$m = (n + 43N_{ID}^2) \, mod \, 127 \quad , 0 \leq n \leq 127 \qquad (4.11)$$

and x values are initiated as indicated in Equation 4.12:

$$
\begin{aligned}
&x(i+7) = (x(i+4) + x(i)) \, mod \, 2 \\
&[x(6) \; x(5) \; x(4) \; x(3) \; x(2) \; x(1) \; x(0)] = [1 \; 1 \; 1 \; 0 \; 1 \; 1 \; 0]
\end{aligned}
\qquad (4.12)
$$

The 5G NR specifies in [47] that there are three possible values for the parameter m, resulting in three distinct values of the PSS: $N_{ID}^2 = [0, 1, 2]$. For all these values, the situation of autocorrelation with a maximum peak at delay zero is valid. With three
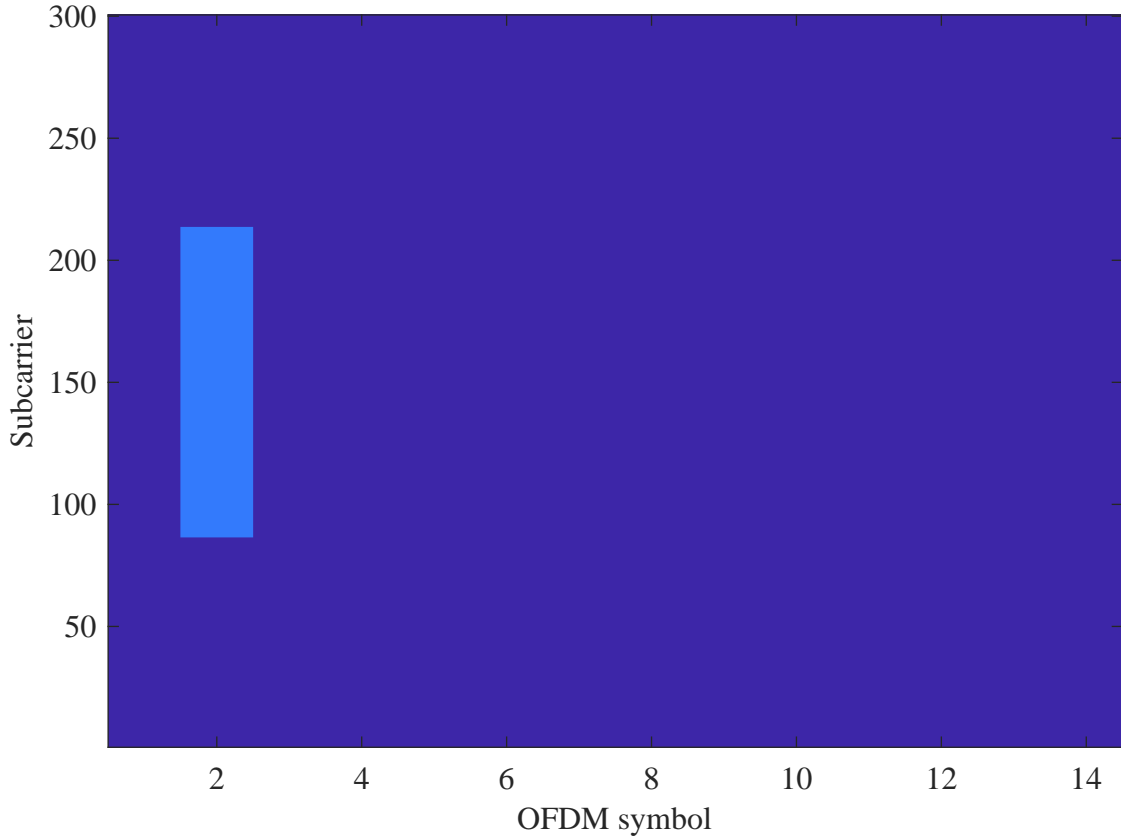
Figure 29 – PSS Resource Elements allocated into SSB grid

possibilities for the value of N_{ID}^2 and another 336 possibilities for N_{ID}^1 it is possible to identify up to 1008 different cells, representing an advancement compared to LTE, which could only identify 504 cells [76].

As specified in [47], the PSS sequence modulates 127 subcarriers and is mapped onto the Resource Grid with a certain offset, ensuring it is positioned in the middle of the grid. In Figure 29, the PSS is mapped for a Resource Grid with $\mu = 0$ and $Bw = 5$ MHz as specified in Table 2. In this case, there are 25 Resource Blocks and 300 available subcarriers. For the scenario depicted in Figure 29, the PSS started at subcarrier 88 and extended to subcarrier 215 in the second slot.

Figure 30 illustrates the signal synchronization process. Firstly, in a), there is a 5G signal with its allocated physical channels (PDSCH, PDCCH, and SSB). This signal was sampled by another receiver with a low level of noise, but initially, the exact frame start was unknown. In b), it is observed that the frame start is not known. However, after performing correlation with the PSS reference signal, a correlation peak is obtained, as shown in c), precisely indicating the start of the 5G frame.

At this point, it is important to observe that N_{ID}^2 has three possible formations, resulting in three distinct m-sequences. However, in the UE receiver, it is not known in advance which N_{ID}^2 was used. Therefore, as illustrated in Figure 31, in a real-time
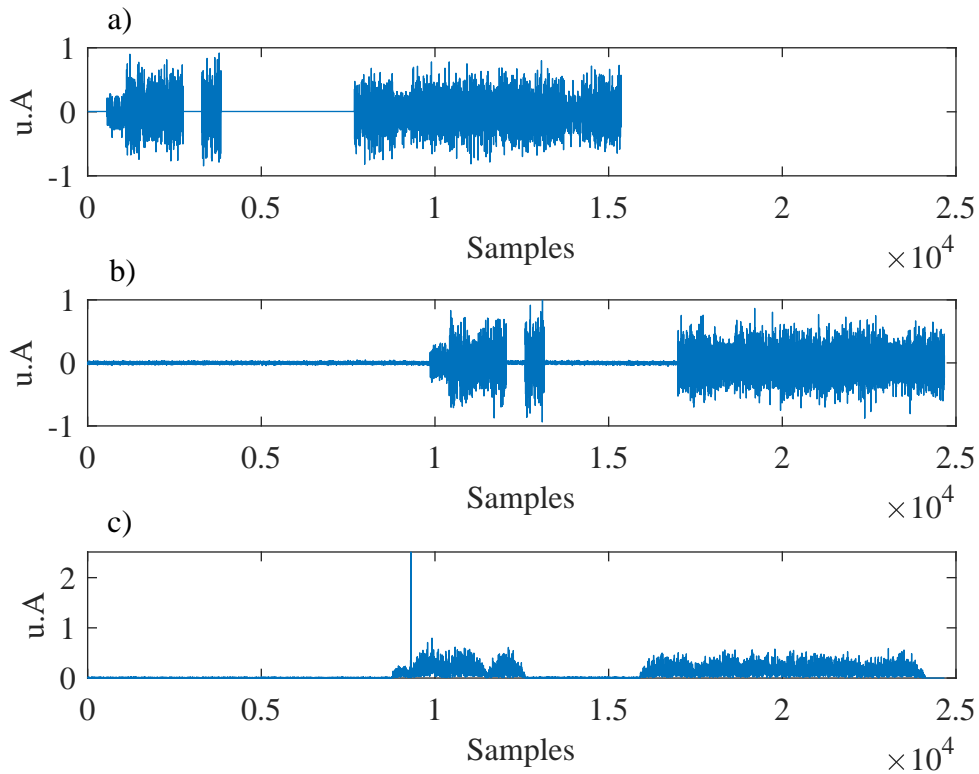
Figure 30 – Synchronization process a) shows the original 5G New Radio signal, b) is a received time shifted 5G NR signal with noise c) is the result of the cross correlation between received time shifted 5G New Radio Signal and OFDM Modulated PSS signal. The peak in this case shows the start sample
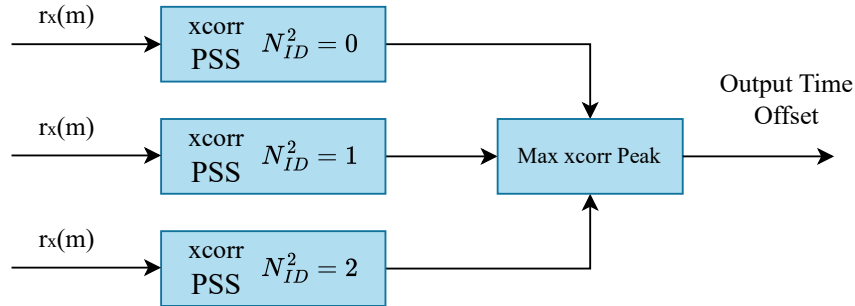
Figure 31 – In the synchronization process, there are three possible PSS signals for the values of $N_{ID}^2 = [0, 1, 2]$. The UE doesn't know exactly which N_{ID}^2 was chosen, so tests are performed for all three possible PSS sequences. A cross-correlation is performed with each sequence, and the highest correlation peak is identified. This peak represents the initial offset, indicating the start of the 5G NR Frame, as well as indicating the N_{ID}^2 of the sequence with the highest correlation.

application, the UE must perform cross-correlation of the received signal with the three possible PSS sequences. For each PSS sequence, there will be a correlation peak, and the highest correlation peak among the three possibilities will be considered as the start sample of the PSS in the received signal.

According to [77] in the software toolbox, the PSS symbols are initialized based

on the N_{ID} using the `nrPSS` function, where this N_{ID} contains the information of N_{ID}^2. The 127 generated symbols are allocated in the second column of the Resource Grid, as depicted in Figure 29, with an initial offset at Resource Element 88.

4.3.3.1.2 Secondary Synchronization Signal - SSS

The Secondary Synchronization Signal (SSS), much like the PSS, is an m-sequence. This signal complements the PSS for identifying the 5G NR cell to which the UE is attached. According to [47] the m-sequence used in the SSS is based on N_{ID}^1 and N_{ID}^2. Equation 4.13 presents the SSS sequence generation:

$$d_{SSS}(n) = [1 - 2x_0((n + m_0) \bmod 127][1 - 2x_1((n + m_1) \bmod 127)] \tag{4.13}$$

where the m-value is denoted by Equation 4.14:

$$m_0 = 3 \left[\frac{N_{ID}^1}{112} \right] + N_{ID}^2$$
$$m_1 = (N_{ID}^1 \bmod 112) + m_0 + 1 \tag{4.14}$$

and x_0 and x_1 values presented in Equation 4.13 are initiated as indicated in Equation 4.15 and 4.16 respectively:

$$x_0(i + 7) = (x_0(i + 4) + x_0(i)) \bmod 2$$
$$[x_0(6)\ x_0(5)\ x_0(4)\ x_0(3)\ x_0(2)\ x_0(1)\ x_0(0)] = [0\ 0\ 0\ 0\ 0\ 0\ 1] \tag{4.15}$$

$$x_1(i + 7) = (x_1(i + 1) + x_1(i)) \bmod 2$$
$$[x_1(6)\ x_1(5)\ x_1(4)\ x_1(3)\ x_1(2)\ x_1(1)\ x_1(0)] = [0\ 0\ 0\ 0\ 0\ 0\ 1] \tag{4.16}$$

Finally, $N_{ID} = 3N_{ID}^1 + N_{ID}^2$. The process to recover the SSS is simpler than that for the PSS. In the case of the SSS, the received symbols with time correction, frequency correction, and equalization. The process involves receiving the SSS sequence and performing Pearson Correlation with the SSS test signals. In this scenario, it is necessary to search for the maximum correlation with N_{ID}^2 received in the PSS and test all $N_{ID}^2 = [0, 1, ..., 336]$ to find the best correlation and detect N_{ID}^2.

The Figure 32 is related to the allocation of SSS resource elements in the Resource Grid. Notice that the SSS occupies Slot 4 of the Resource Grid and furthermore shares the same bandwidth allocation as the PSS (127 subcarriers). Also, note that the third symbol
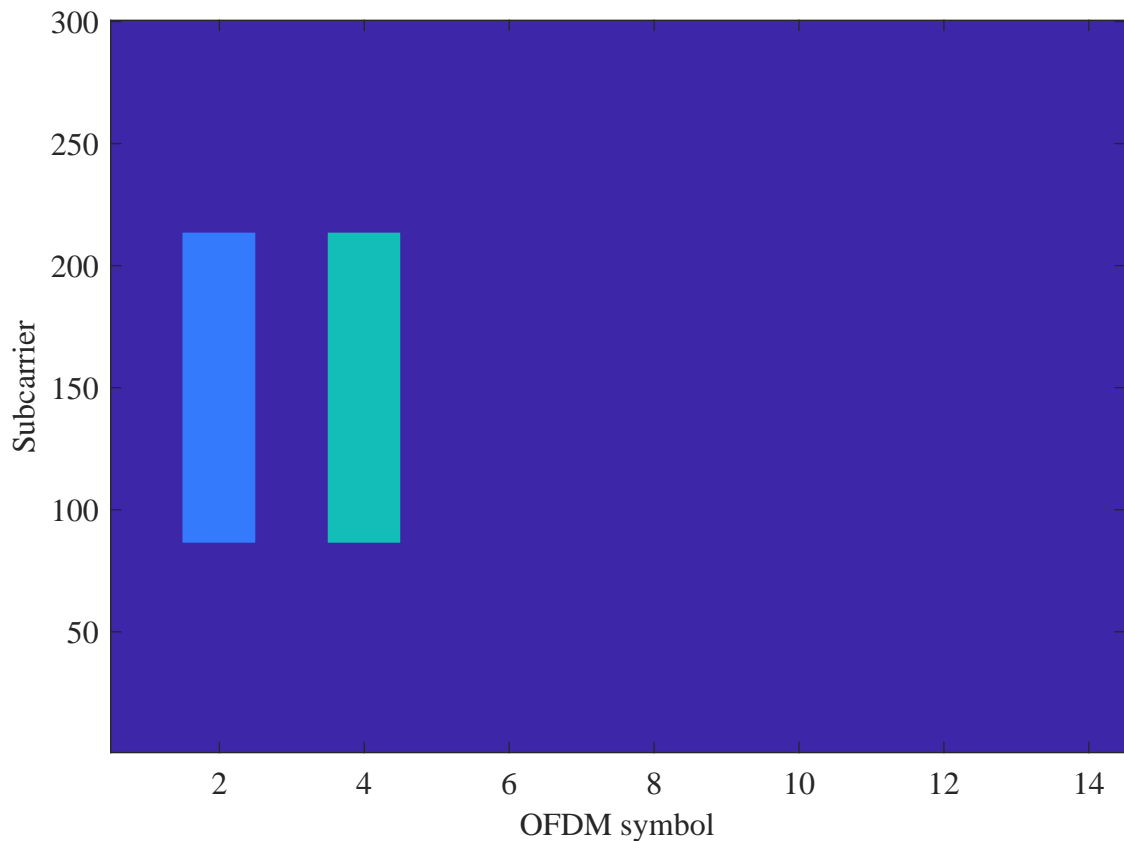
Figure 32 – PSS and SSS Resource Elements allocated into SSB grid

of the time slot is related to the PBCH, which will be further explored in the subsequent section. For the generation of SSS, the 5G Toolbox relies on the reference in [78]. It's worth noting that similar to PSS, SSS only requires the N_{ID} parameter, and the toolbox will return the sequence of Resource Elements to be correctly allocated in column 4 of the Resource Grid matrix.

4.3.3.1.3 Physical Broadcast Channel - PBCH

As discussed earlier, this work primarily focuses on the implementation of channels associated with the Data Plane, rather than those related to the Control Plane. However, it's important to note the direct relationship between the Physical Broadcast Channel (PBCH) and the Signal Synchronization Block (SSB). Consequently, certain simplifications were made. According to [47], the PBCH channel utilizes Polar encoding for its transmission bits, which carry information from the Master Information Block (MIB) through the Broadcast Channel (BCH). In this context, the simplification involves introducing a random character codeword into the resource grid to generate the PBCH signal.

However, despite the simplifications made, the implementation retained symbols known as PBCH-DMRS (Physical Broadcast Control Channel - Demodulation Reference Signals). These signals consist of sequences recognized as pilots, employed to equalize the

received signal in the UE (User Equipment).

According to [47], the DMRS Downlink symbols are defined by equation 4.17. The DMRS is based on pesudorandom signal and its results in a QPSK constellation [60].

$$r(m) = \frac{1}{\sqrt{2}}(1 - 2c(2m)) + j\frac{1}{\sqrt{2}}(1 - 2c(2m + 1)) \tag{4.17}$$

where $c(n)$ is defined by 3GPP Pseudo-random generic sequence proposed in [47] as illustrated in equation 4.18. The sequence $c(n)$ is a scrambling sequence composed of two 31-bit Gold sequences. This DMRS symbol generation scheme will be used in other physical channels; however, each channel will have the peculiarity of its own initializing sequence c_{init}.

$$
\begin{aligned}
c(n) &= (x_1(n + N_c) + x_2(n + N_c)) \, mod \, 2 \\
x_1(n + 31) &= (x_1(n + 3) + x_1(n)) \, mod \, 2 \\
x_2(n + 31) &= (x_2(n + 3) + x_2(n + 2) + x_2(n + 1) + x_2(n)) \, mod \, 2
\end{aligned} \tag{4.18}
$$

where $N_c = 1600$ and the initialization of variables proceeds as follows: $x_1(0) = 1$, with the remaining values set to zero, denoted as $[x_1(0), x_1(1), ..., x_1(30)] = [1, 0, ..., 0]$. The initialization of x_2 depends on $c_{init} = \sum_{i=0}^{30} x_2(i)2^i$, where $x_2(i)$ represents the i-th bit of c_{init} for $i = 0, ..., 30$. The initialization of $c(n)$ also relies on c_{init}; equation 4.19 demonstrates the calculation of c_{init} for PBCH DMRS symbols.

$$c_{init} = 2^{11}(\bar{i}_{SSB} + 1)([N_{ID}/4] + 1) + 2^6(\bar{i}_{SSB} + 1) + (N_{ID} \, mod \, 4) \tag{4.19}$$

Finally, $\bar{i}SSB$ is defined in [47], and it depends on the length of Synchronization Signal Blocks (SSBs). In this work, only one SSB block is available in the first half frame, and its length is $L_{max} = 4$ (PSS,SSS and PBCH). According to [47], the value of $\bar{i}SSB$ is 2.

The subcarrier index destined to carry the PBCH-DMRS symbols for $\mu = 0$, according to [47], The allocation is based in the subcarrier index $\nu = N_{ID} \, mod \, 4$. After ν calculation the PBCH symbols will be allocated as proposed in equation 4.20.

$$
\begin{aligned}
[0 + \nu, 4 + \nu, 8 + \nu, ..., 236 + \nu], & \quad symbol = [3, 5] \\
[0 + \nu, 4 + \nu, 8 + \nu, ..., 44 + \nu, 192 + \nu, 196 + \nu, ..., 236 + \nu], & \quad symbol = 4
\end{aligned} \tag{4.20}
$$

The symbol allocation mentioned earlier is conducted within the PBCH subcarrier index, which 240 subcarriers. Consequently, the entire Resource Grid comprises 300 subcarriers. To ensure the PBCH block's centralization within the Resource Grid, the starting subcarrier was shifted to $(300 - 240)/2 = 30$ subcarriers above the central position. Figure 33 shows the SSB with PSS, SSS and PBCH-DMRS symbols allocated.
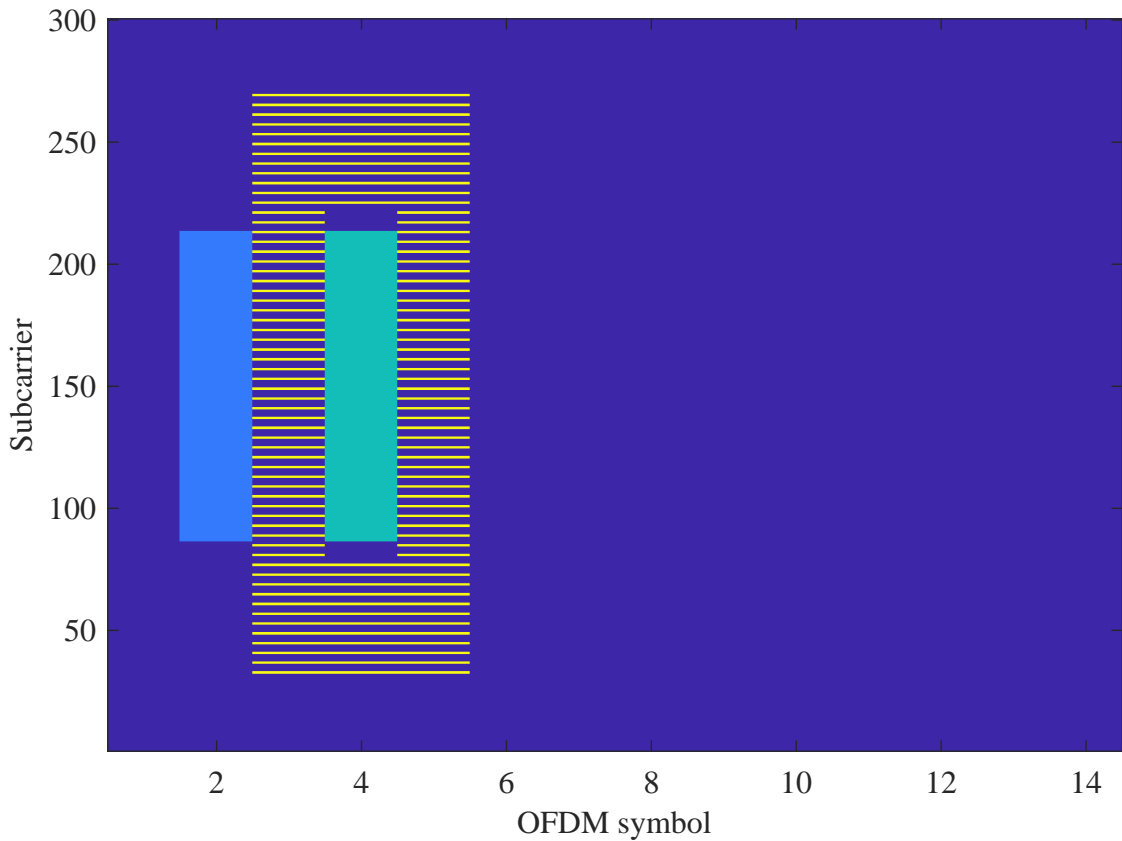
Figure 33 – PSS, SSS and PBCH-DMRS Resource Elements allocated into SSB grid

For the remaining symbols of the PBCH, a random codeword was inserted. For simplification, polar encoding was not applied, as this signal was not decoded at the UE. According to [47], PBCH symbols are modulated using QPSK modulation and directly applied to the Resource Grid according to the allocation described in equation 4.21.

$$
\begin{array}{ll}
[0, 1, ..., 239], & symbol = [3, 5] \\
[0, 1, ..., 47, 192, 193, ..., 239], & symbol = 4
\end{array}
\tag{4.21}
$$

Figure 34 illustrates the complete allocation of the SSB within a Resource Grid, emphasizing the fixed size of the PBCH, which consists of 240 subcarriers. Additionally, it's worth noting that, as discussed earlier, due to bandwidth limitations of the LED, a bandwidth of Bw = 5 MHz was employed. However, referring to Table 2, it becomes evident that for $\mu = 1$ or SCS = 30 kHz, the 3GPP 5G New Radio system only provides 11 Resource Blocks or 132 subcarriers. This indicates that utilizing SCS = 30 kHz requires additional efforts to handle this exception, as the PBCH requires 240 subcarriers. Therefore, the work will be restricted to using $\mu = 0$, SCS = 15 kHz.

Similarly to PSS and SSS, the PBCH-DMRS symbols can be obtained from [79] using nrPBCHDMRS. The inputs expected by the toolbox are the N_{ID} and $\bar{i}_{SSB} = 2$, as indicated for the generation of c_{init} in Equation 4.19. Additionally, the toolbox proposes
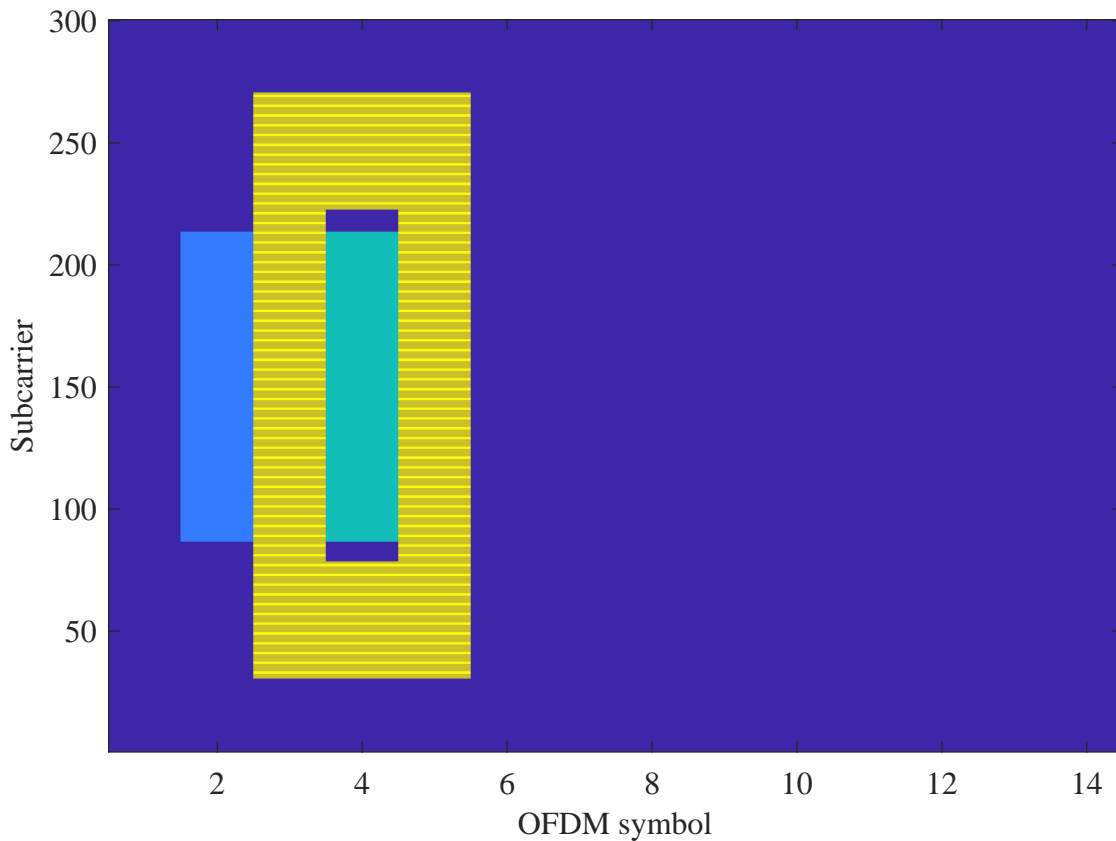
Figure 34 – PSS, SSS, PBCH-DMRS, abd PBCH Resource Elements allocated into SSB grid

an easy method to obtain the allocation indices in the Resource Grid matrix. Essentially, the function described in [80] applies Equation 4.20, which depends only on N_{ID}, to obtain the proper positions of the PBCH-DMRS symbols within the Resource Grid with nrPBCHDMRSIncides. On the other hand, the PBCH symbols will be generated using the function nrPBCH described in [81]. At this point, it's worth noting that after the allocation of PBCH-DMRS symbols, there are 432 free Resource Elements remaining. Since the modulation is only QPSK, a random PBCH payload of 864 bits will be generated for the PBCH. Finally, similar to PBCH-DMRS, there exists a function for generating PBCH indices nrPBCHIndices described in [82], responsible for generating the allocation indices of PBCH within the Resource Grid matrix.

4.3.3.2 Physical Downlink Control Channel - PDCCH

The Downlink Control Channel, known for carrying Downlink Control Information (DCI), encompasses various formats detailed in [69]. It's crucial to acknowledge that the VLC-5G prototype operates with several limitations and simplifications compared to the 5G Mobile system. Given these constraints, the DCI Format 1_0 was specifically chosen for implementation, and its details are outlined in the Table 4:

Referring to [83], utilized for both 4G LTE and 5G NR, an Aggregation Level of

Name	Length (Bits)	Description
Identifier	1	Always 1
Frequency Resources	4	Not used
Resource Assignment	4	First OFDM Symbol of PDSCH Grid
VRB-to-PRB Mapping	1	Always 0 - Non Interleaved
Modulation Scheme	5	See Appendix (B)
New Data Indication	1	1 = New Data, 0 = Retransmission
Redundancy Version	2	1 = Not Used- Always zero
HARQ	4	Not Used- Always zero
Downlink assignment Index	1	1 = Not Used- Always zero
TPC Command for PUCCH	2	1 = Not Used- Always zero
PUCCH Resource Indicator	3	1 = Not Used- Always zero
PDSCH HARQ timing indicator	3	1 = Not Used- Always zero

Table 4 – Detailed Downlink Control Information Fields

4 corresponds to a total of 288 PDCCH subcarriers. Among these, 72 are allocated to PDCCH-DMRS, while the remaining 216 are utilized for PDCCH DCI, as specified in [83]. The [47] specifies PDCCH modulation only with QPSK symbols, resulting in 432 bits for DCI. Table 4 illustrates a specific allocation of 31 bits for DCI information. Consequently, these 31 bits are iterated approximately 13.93 times within the PDCCH allocation to completely populate the PDCCH Resource Grid.

The PDCCH-DMRS symbols follows the same principles showed in the equations4.17 and 4.18, but in this case the c_{init} is different as illustrated in equation 4.22:

$$c_{init} = (2^{17}(N_{symb}^{slot}n_s + l + 1)(2N_{ID} + 1) + 2N_{ID}) \, mod \, 2^{31} \qquad (4.22)$$

where l is the number of slot-symbols used ($l = 1$), $N_{symb}^{slot} = 14$ is the number of symbols inside in a slot, $n_s = 1$ is the number of slots-symbols dedicated to PDCCH, for $\mu = 0$, then $n_s = 1$ and N_{ID} is the cell number. The symbol allocation for a single slot, as specified in [47], starts at $k = 2$ and spans from 2 to 288 at an Aggregation level of 4. This allocation scheme designates 72 DMRS symbols within the 288 PDCCH symbols, resulting to 1 DMRS occurrence per 4 PDCCH symbols. For visual reference, Figure 35, shows the allocation of PDCCH DMRS.

Figure 36 illustrates the allocation of the PDCCH (which includes both DMRS and PDCCH Symbols) within the Resource Grid. With the conclusion of the first slot, the allocation will now transition to the 15th OFDM Symbol, specifically designated for the PDSCH.

For PDCCH-DMRS, the process of generating indices and DMRS symbols can be done using only the function described in [84]. In this case, a data structure called nrCarrierConfig is used, which defines parameters of the 5G NR carrier: N_{ID}, SCS, N_{RB}. Additionally, an nrPDCCHConfig structure is used as an input parameter and must
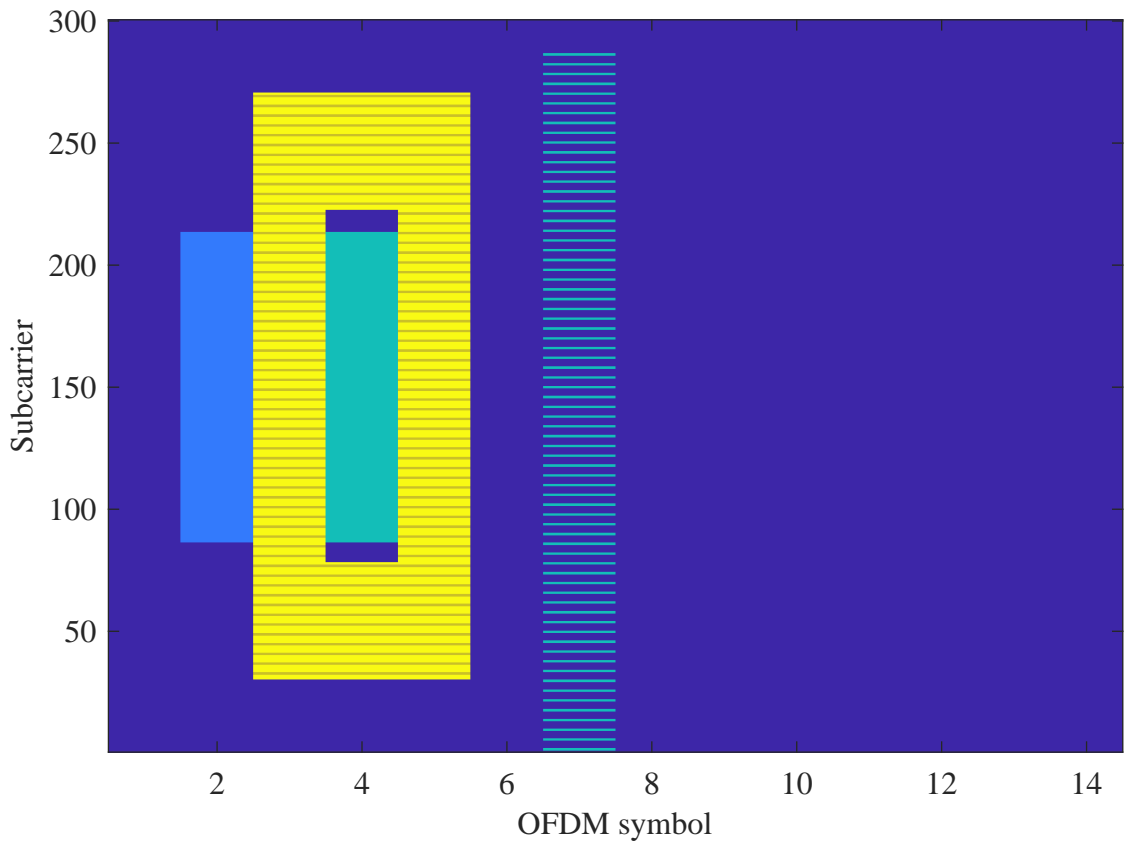
Figure 35 – SSB Block and PDCCH DMRS Allocation
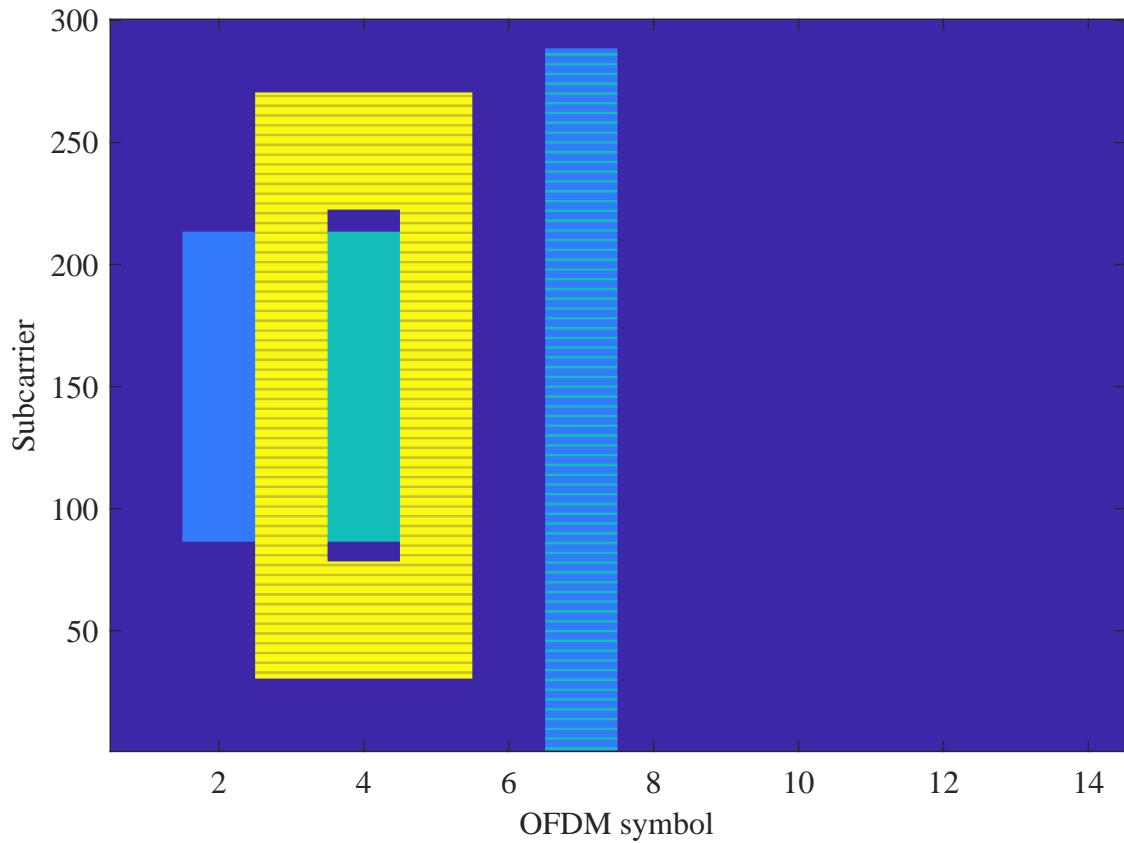
Figure 36 – SSB Block and PDCCH DMRS Allocation

be configured with the correct parameters: AggregationLevel, N_{RB}, n_s. The function nrPDCCHResources returns the PDCCH-DMRS symbols, their respective indices, and also the allocation indices of the PDCCH. Finally, it's only necessary to obtain the QPSK symbols used in PDCCH according to [85]. As discussed, the 31-bit DCI is repeated until 432 available bits are obtained. From there, the nrPDCCH function takes care of performing QPSK modulation.

4.3.3.3 Physical Downlink Shared Channel - PDSCH

The Physical Downlink Shared Channel (PDSCH) is the most crucial Downlink channel for this project. It's where all payload symbols (User Plane) will be allocated and effectively transmitted by the gNB to the UE. This channel plays a central role in efficiently transferring user data and is essential for effective communication between the base station (gNB) and the user device (UE).

As discussed in section 4.3.2.1, the PDSCH channel receives data from the DL-SCH transport channel. Here, the User Plane data undergoes CRC attachment, division into Code Blocks each with a new CRC, LDPC encoding, and finally, Rate Matching is applied to achieve the expected number of subcarriers. Furthermore, as depicted in Figure 19, a 5G NR Frame consists of 10 subframes. Presently, only the first subframe has been utilized for the SSB and PDCCH. The remaining nine subframes are designated for the allocation of User Plane data (payload).

Similar to PBCH and PDCCH, there are reference signals (PDSCH-DMRS) crucial for the reception and accurate channel equalization. Just like in the case of PDCCH and PBCH, the PDSCH-DMRS symbols adhere to the format outlined in equation 4.17, with the initialization c_{init} as proposed in the Equation 4.23.

$$c_{init} = (2^{17}(N_{symb}^{slot}n_s + l + 1)(2N_{ID} + 1) + 2^{17}\left\lfloor\frac{\overline{\lambda}}{2}\right\rfloor + 2N_{ID} + \overline{n}_{SCID}^{\overline{\lambda}}) \, mod \, 2^{31} \quad (4.23)$$

where, $l = 2$ is the OFDM symbol number within the slot $n_s = 1$ and N_{ID} is the cell identification, and according [47] for DCI Format 1_0 $\overline{n}_{SCID}^{\overline{\lambda}} = 0$ and $\overline{\lambda} = 0$. The characterization of PDSCH-DMRS symbols involves three primary parameters, as discussed in [60]: the mapping type (A or B), the configuration type (1 or 2), and the DMRS length within a slot. Mapping type A defines the time reference, specifying whether the slot symbol initiates at the second position ($l_0 = 2$) or the third position ($l_0 = 3$) concerning the first slot-symbol. For clarity, Figure 37, part a), illustrates the $l_0 = 2$ time reference concerning the first non-allocated data. On the other hand, Mapping type B signifies the DMRS position concerning the beginning of the PDSCH allocated data ($l_0 = 0$), referencing the first PDSCH slot symbol, as detailed in [86]. In this context, Figure 37, part b), depicts the structure associated with Mapping type B.
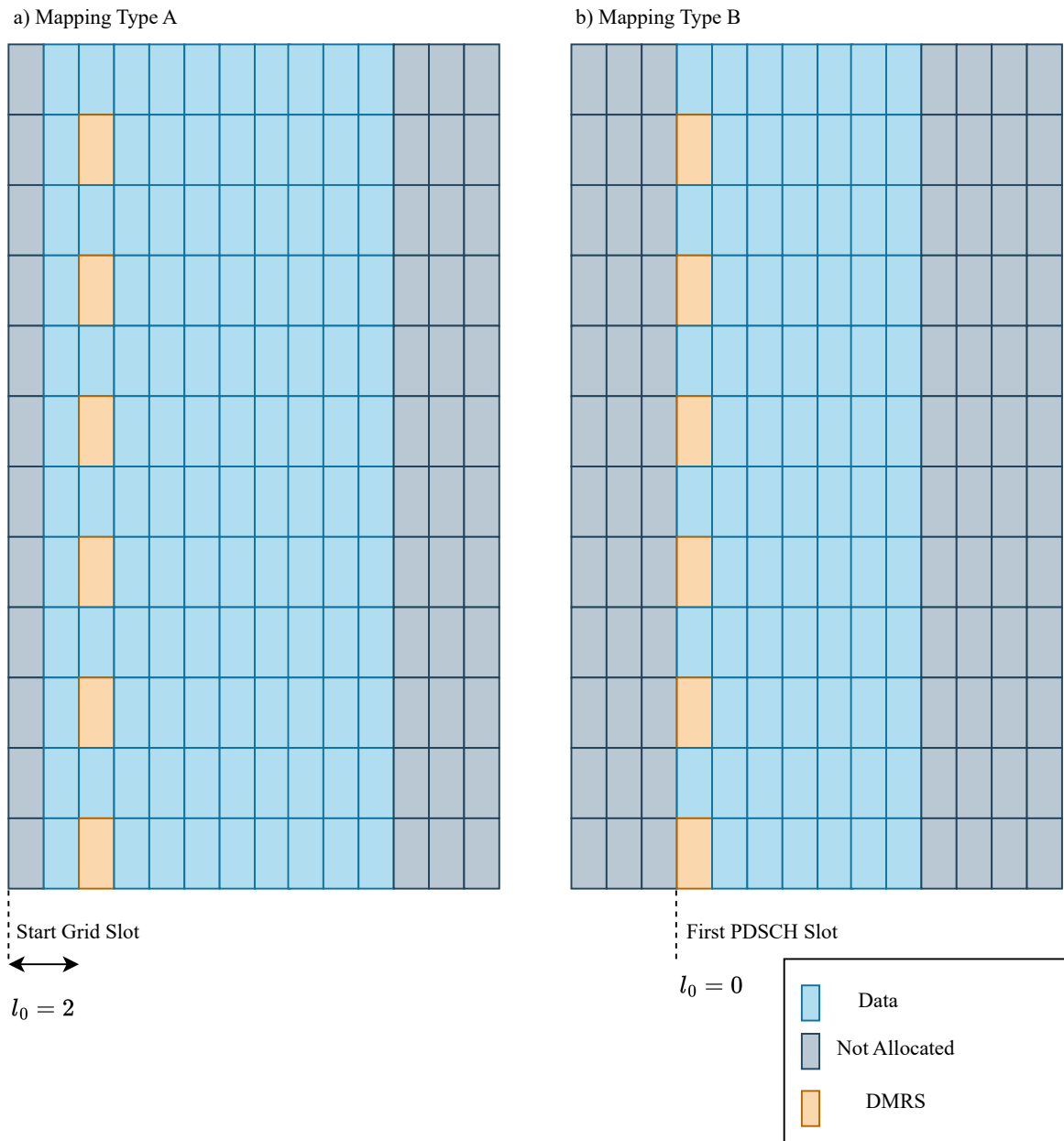
Figure 37 – a) The structure of PDSCH-DMRS mapping type A involves allocating resource elements within a Resource Grid with an offset from the grid's start, specifically $l_0 = 2$. b) Conversely, the structure of PDSCH-DMRS mapping type B entails allocating resource elements with an offset of $l_0 = 0$ from the first PDSCH slot.

The length of the DMRS is directly linked to the duration of the time slot-symbol. In Figure 38, part a) illustrates a length of $L = 1$ for the DMRS duration, while part b) showcases two consecutive DMRS slot symbols allocated with a length of $L = 2$

The parameter for configuration type 1 specifies the mapping of DMRS (Demodulation Reference Signal) PDSCHs to non-contiguous subcarriers. As detailed in [47] and illustrated in Figure 39 part a) for PDSCH-DMRS Configuration type 1, a Resource Block of 6 subcarriers is assigned to receive DMRS symbols. Conversely, configuration type 2, as
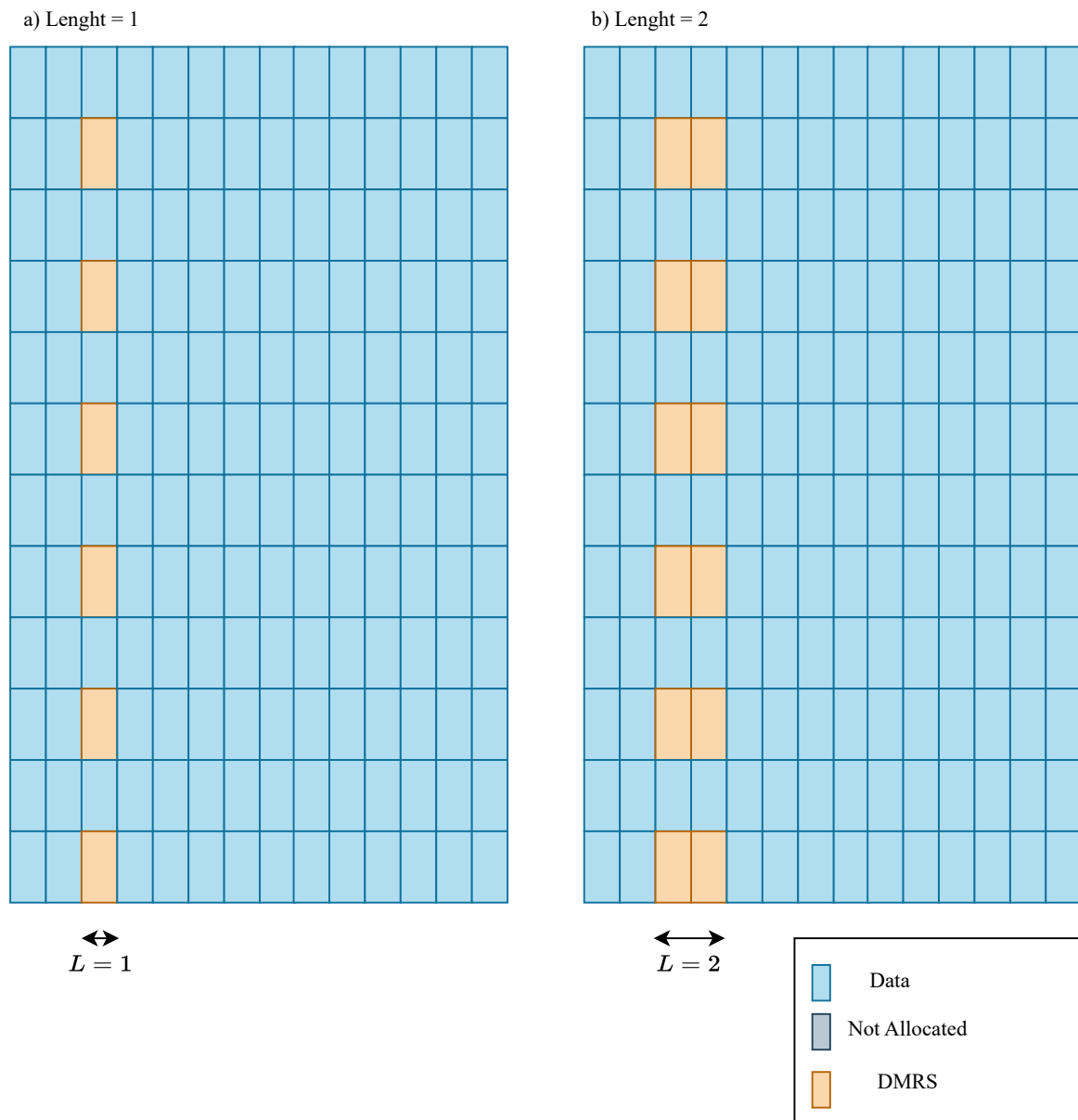
Figure 38 – a) For DMRS, a single symbol represents the slot-symbol length, denoted as $L = 1$. b) In contrast, the slot-symbol length for DMRS consists of two symbols, indicated as $L = 2$.

depicted in Figure 39 part b), mandates the use of two contiguous carriers for allocating DMRS symbols, with 4 subcarriers dedicated to receiving these symbols within a Resource Block.

In 5G NR 3GPP indeed offers a configuration to include extra DMRS (Demodulation Reference Signal) symbols [47]. These additional symbols come into play when the channel conditions deteriorate due to factors like low signal-to-noise ratio (SNR), high Doppler shift frequency, or significant multipath effects [60]. Figure 40 shows an example that the additional DMRS employed in the PDSCH Resource Grid.

It's crucial to recognize that when these extra DMRS symbols are incorporated, the
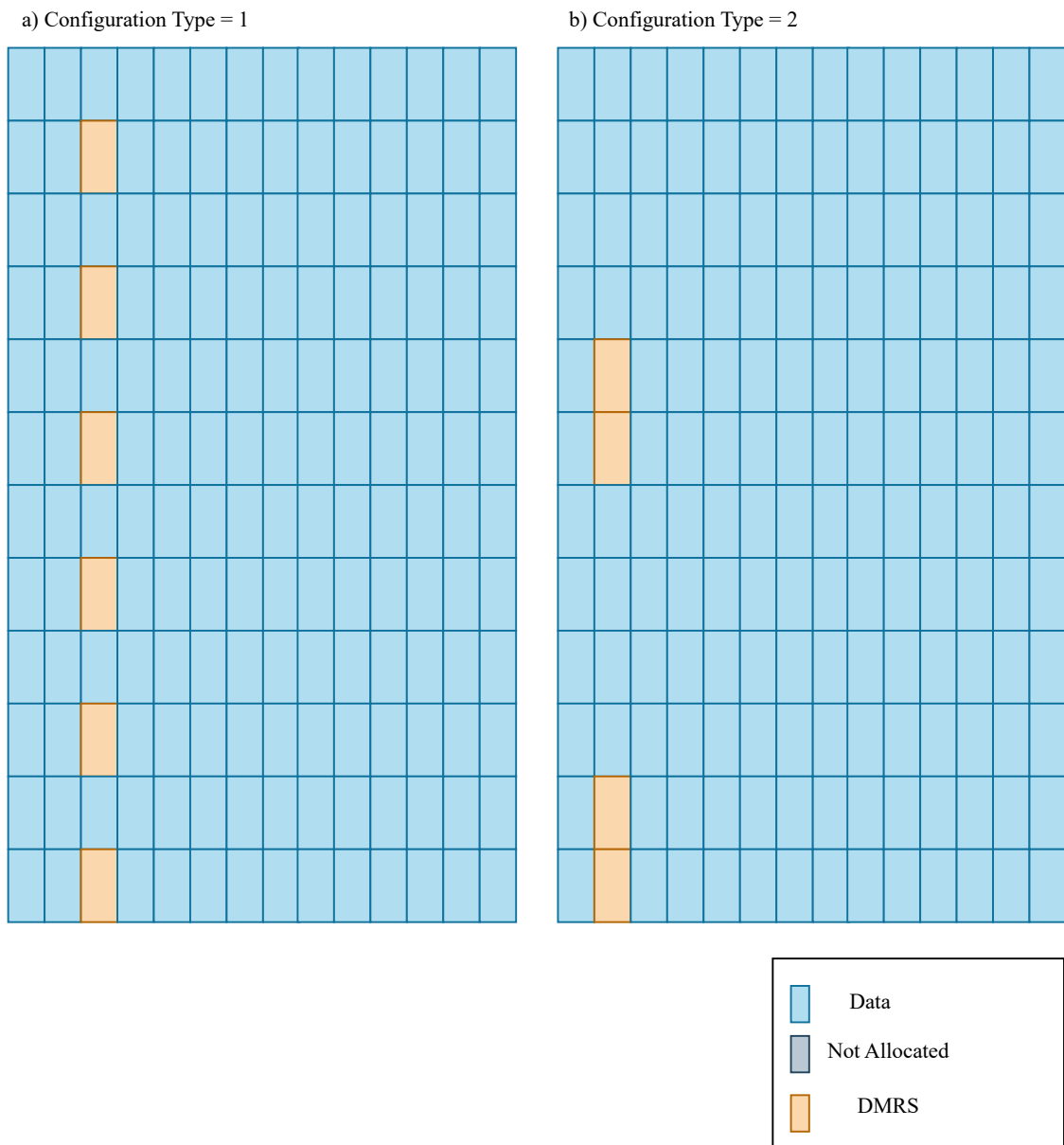
Figure 39 – a) In configuration type 1, DMRS symbols are non-contiguous, utilizing 6 resource elements within a Resource Block. b) On the other hand, configuration type 2 couples the DMRS with two symbols, utilizing 4 resource elements within a Resource Block.

resource grid initially allocated for data transmission gets utilized to carry these DMRS symbols instead. This decision represents a trade-off in 5G NR: while it enhances channel estimation accuracy by providing additional reference signals, it comes at the expense of reducing the available resources for transmitting payload data. This trade-off is an essential consideration in optimizing the balance between channel estimation quality and data transfer efficiency within the constraints of varying network conditions. It's about using resources wisely to make sure communication stays strong, even in tough situations, though it might mean sacrificing some data resource elements.
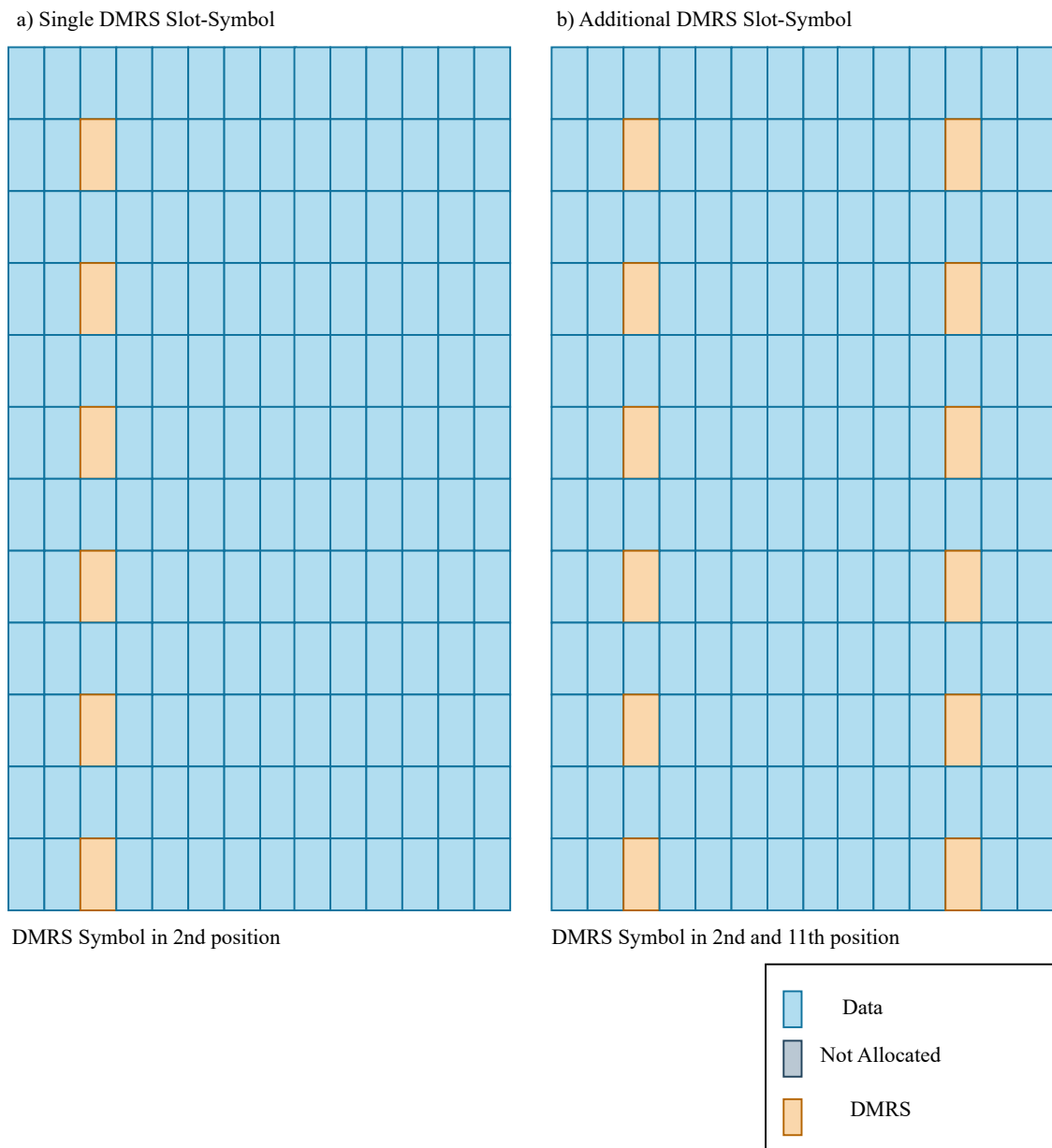
Figure 40 – a) The allocation of DMRS only on the 2nd slot-symbol of the Resource grid. b) An additional DMRS slot symbol is added by placing the DMRS in the 2nd and 11th slot-symbols.

For the implementation of this project, only the usage of DMRS for PDSCH with mapping type A, configuration type 1, and length $L = 1$ was considered. However, an additional DMRS symbol-slot was inserted to enhance channel equalization and estimation, especially in RF environments. This addition aims to improve channel estimation by multiplexing symbols in frequency at two different time instances, particularly addressing temporal variance. The Figure 41 shows the allocation of PDSCH-DMRS for all the remaining 9 slots within the Frame format discussed in Figure 18. Note that the DMRS pair repeats with each new subframe.

For the remaining Resource Elements of the PDSCH, the DL-SCH encoding process

Figure 41 – Allocation of PDSCH-DMRS elements with mapping type A, configuration type 1, and length $L = 1$ and a additional DMRS. Note that a DMRS pair is inserted in each subframe to enhance the estimation of the transmission channel.

MCS Index	Modulation	Code Rate
1	QPSK	120/1024
5	QPSK	602/1024
6	16QAM	378/1024
11	16QAM	658/1024
12	64QAM	466/1024
20	64QAM	873/1024

Table 5 – All MCS considered for work in this project. Note that for each modulation order, a low and a high coderate were selected to achieve high and low redundancy, respectively.

4.3.2.1 was executed, involving CRC application, LDPC Encoding, and Rate Matching. Subsequently, modulation was applied based on the MCS (Modulation Control Scheme) field in the DCI (Downlink Control Information) specified in the PDCCH 4.3.3.2. The Table 5 displays the utilized MCS in the tests. Additionally, note that for each modulation order, both a low and high code rate level were chosen. In other words, these represent scenarios with high and low redundancy. The Figure 42 illustrates the allocation of the remaining PDSCH elements across the 9 available subframes within the Resource Grid.
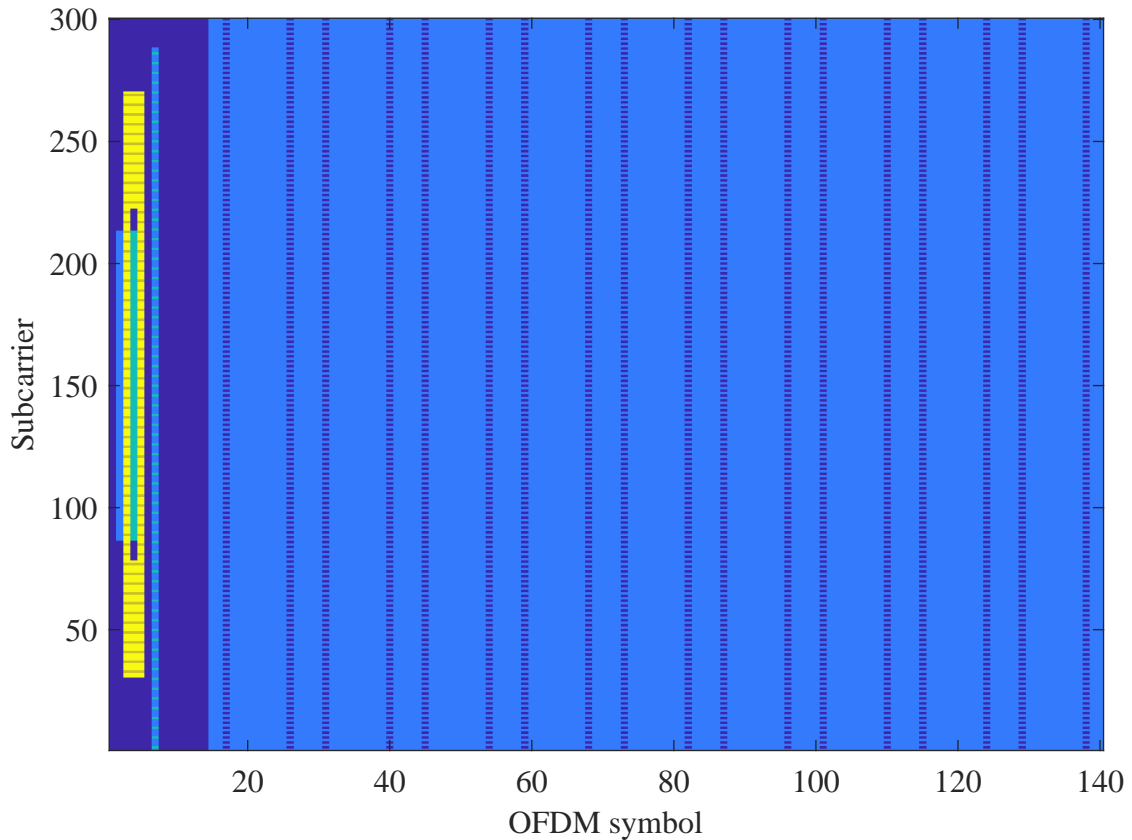
Figure 42 – The entire frame allocated within the Resource Grid (SSB + PDCCH + PDSCH).

The PDSCH-DMRS symbols are generated using the function nrPDSCHDMRS described in [87], and their respective indices are obtained using the function nrPDS-CHDMRSIndices [88], which are defined in the 5G toolbox. In this case, the nrCarrierConfig structure must be used. Additionally, the nrPDSCHDMRSConfig structure is utilized, where the following parameters are defined: DMRSConfigurationType, DMRSLength, DMRSAdditionalPosition, DMRSTypeAPositionm, N_{ID}, and $\overline{n}_{SCID}^{\overline{\lambda}}$ as established in equation 4.22. These parameters need to be correctly configured for the generation of the respective PDSCH-DMRS symbols and their indices.

The function nrPDSCH described in [89] also takes the nrCarrierConfig data structure and an nrPDSCHConfig data structure. It's important to note that the nrPDS-CHDMRSConfig structure is inserted inside the nrPDSCHConfig. Furthermore, nrPDSCH-Config also establishes the modulation order, N_{RB}, and N_{ID}. After obtaining the PDSCH symbols, allocation indices within the Resource Grid matrix can be generated using the function nrPDSCHIndices as described in [90].

4.3.3.4 Sounding Reference Signals - SRS

Frame-level synchronization for the Uplink differs somewhat from the method used in the Downlink. In the Downlink, the approach relied on signals forming the Synchronization Signal Block (SSB), with the Primary Synchronization Signal being crucial for providing time offset and frequency offset information. Unfortunately, in the Uplink, the PSS is not specified. The synchronization process is quite different, and the Physical Random Access Channel (PRACH) is employed. This channel goes beyond the scope of this work, and therefore, a simplification was made using the Sounding Reference Signal (SRS) directly.

The Sounding Reference Signal (SRS) for the Uplink is a signal capable of performing such synchronization, generated based on a Zadoff-Chu pseudo-random sequence [60]. This type of sequence finds extensive application in signal synchronization, a technique also employed by LTE for its Primary Synchronization Signal (PSS) synchronization [83].

The m-sequence and Zadoff-Chu sequences represent distinct types of signal sequences used in wireless communication. The m-sequence is a binary sequence and it is generated through a linear feedback shift register, offering valuable pseudo-random characteristics for spread spectrum and synchronization purposes [48]. Conversely, Zadoff-Chu sequences, complex in nature, serve communication systems by providing robust autocorrelation traits, low cross-correlation interference, and reliable channel estimation properties. These sequences find significant utility in Orthogonal Frequency Division Multiplexing (OFDM) systems like 5G NR [49], specifically in generating Sounding Reference Signals (SRS) and addressing synchronization requirements due to their advantageous properties suited for modern communication needs.

According [47], the SRS is defined by Equation 4.24.

$$
\begin{aligned}
&r^{(p_i)}(n, l') = w_{TDM}^{(p_i)}(l') r_{(u,v)}^{(\alpha_i, \delta)}(n) \\
&0 \leq n \leq M_{sc,b}^{SRS} - 1 \\
&l' \in \{0, 1, ..., N_{symb}^{SRS} - 1\}
\end{aligned}
\tag{4.24}
$$

The expression $r_{(u,v)}^{(\alpha_i, \delta)}(n)$, described in equation 4.25, characterizes the signal being analyzed. For a single antenna port indicated by $p_i = 1$, $w_{TDM}^{(p_i)}(l')$ is set to 1. The parameter δ corresponds to $log_2(K_{TC})$, where K_{TC} represents a transmission combination $\in \{2, 4, 8\}$. In line with simplifications from [47], K_{TC} is standardized to 2 for this analysis. Furthermore, $M_{sc,b}^{SRS}$ denotes the count of subcarriers assigned for SRS within a Resource Block, consistently set at 6 for simplification purposes. In this project, the SRS is allotted only one slot-symbol, resulting in $N_{symb}^{SRS} = 1$. Finally, α signifies the cyclic frequency shift, with further specifics available in [67]; however, for this particular implementation, $\alpha = 0$

and it indicates that no frequency shift is employed.

$$r_{(u,v)}^{(\alpha_i,\delta)}(n) = e^{j\alpha n}\bar{r}_{u,v}(n)\,,\, 0 \leq n \leq M_{ZC} \tag{4.25}$$

In equation 4.25 the $M_{ZC} = mN_{sc}^{RB}/2^\delta$ is the Zadoff-Chu sequence length, $m = 4$ is the total number of Resoure Blocks used to SRS [47], $\delta = log_2(K_{TC}) = 1$ and $N_{sc}^{RB} = 12$. Therefore, $M_{ZC} = 24$. Equation 4.26 shows the $\bar{r}_{u,v}(n)$ for $M_{ZC} = 24$.

$$\bar{r}_{u,v}(n) = e^{j\phi(n)\pi/4}\,,\, 0 \leq n \leq M_{ZC} - 1 \tag{4.26}$$

where $\phi(n)$ values for $M_{ZC} = 24$ are defined in [83] and available in Appendix C.

For SRS allocation, an extensive and complex formula is detailed in [47]. However, to simplify, Resource Block number 12 (positioned near the Resource Grid's midpoint) is considered. Assuming $K_{TC} = 2$, this results in $M_{ZC} = 24$, spread across 4 resource blocks. Consequently, 6 SRS symbols will be distributed over 4 Resource Blocks during a single slot-symbol. The Figure 43 illustrates the allocation of SRS symbols. The allocation begins at subcarrier $N_{start}N_{sc}^{RB} = 12 \times 12 = 144$ and spans across 4 Resource Blocks, continuing until subcarrier 196.
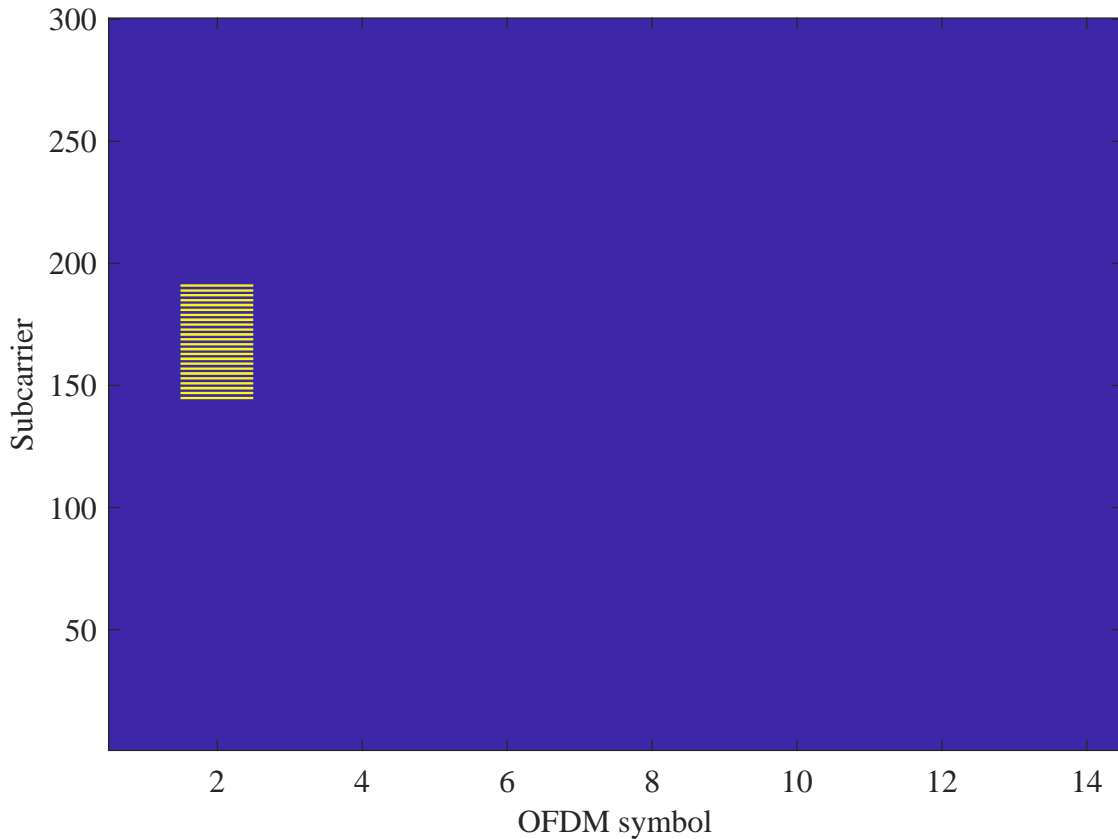
Figure 43 – Sounding Reference Signals allocation starts from Resource Block 12 until Resource Block 16

The generation of SRS symbols follows the same pattern as the others. The function nrSRS produces the symbols of the Zadoff-Chu sequence as described in [91], and the function nrSRSIndices [92] is used to obtain the corresponding indices. Only the nrCarrierConfig parameters and the nrSRSConfig data structure are required as input. The nrSRSConfig structure defines N_{symb}^{SRS}, K_{TC}, $M_{sc,b}^{SRS}$, and m, which are parameters defined in Equations 4.24 and 4.25 to generate SRS and SRS Indices and map them to the Resource Grid matrix.

4.3.3.5 Physical Uplink Control Channel - PUCCH

Similar to the Downlink, the Physical Uplink Control Channel (PUCCH) exists for the Uplink. However, unlike the Downlink, the Uplink introduces the concept of PUCCH Formats [47]. Essentially, the distinction between PUCCH Formats lies in the number of slot symbols and the bits that will be modulated.

PUCCH Format	Slot Symbols	Number of bits
0	1-2	≤ 2
1	4 - 14	≤ 2
2	1-2	> 2
3	4-14	> 2
4	4-14	> 2

Table 6 – Different PUCCH formats with detailing of the slot-symbol used and the quantity of bits inserted into the physical channel.

The PUCCH Format 2 has been chosen for this implementation, following the details in the specification [93] due to the fact that this PUCCH format was designed to send ACK/NACK control information. This implementation includes the presence of PDCCH-DMRS symbols mapped within the physical channel. Across all implementations, the symbols are modulated using QPSK. As per the specification outlined in [47] for PUCCH, 16 Resource Elements are allocated for the PUCCH symbols and 8 Resource Elements for PUCCH-DMRS decoding.

The specification [69] outlines that unlike DCI, the UCI can be mapped by both PUCCH and PUSCH depending on the scenario. However, in this project, the use of UCI will be confined to PUCCH, while PUSCH will be entirely dedicated to transmitting the payload via UL-SCH.

As per [69], UCI will be exclusively employed to transmit ACKNOWLEDGE information (ACK/NACK). The 5G NR incorporates a mechanism called Hybrid Automatic Repeat reQuest (HARQ), crucial for error correction during transmission. It combines retransmission techniques and error coding to enhance wireless communication reliability. HARQ allows a receiver to request retransmissions of corrupted or lost data packets.

HARQ operates at the MAC layer and, as discussed, isn't the primary focus of this project. In this case, the User Equipment (UE) checks errors in DL-SCH and sends ACKs in the Uplink via PUCCH Uplik Control Information. The UCI significantly differs from PDCCH; only the ACK and NACK bits will be transmitted in this project's implementation. Furthermore, it is assumed that the Uplink will utilize the same modulation order and coderate as the MCS decoded in the PDCCH DCI. This approach aligns with other communication systems in IoT systems like LoRaWAN for example [94], which maintains the same spreading factor in the Uplink upon receiving a subsequent Downlink.

Therefore, in the case of an ACK sent via UCI, the bit sequence will be $[1, 0]$, whereas a NACK corresponds to the sequence $[0, 1]$. Additionally, as previously discussed, 16 subcarriers are allocated for PUCCH, modulated in QPSK, requiring 32 bits in the UCI. As mentioned earlier for PDCCH and PBCH, the control channel bits do not undergo the polar encoding specified in the 5G NR standard. These have been simplified. Similar to PDCCH, the 2-bit ACK/NACK sequence is repeated 16 times to form the 32-bit UCI allocation.

Similar to the PDCCH, the PUCCH also incorporates DMRS symbols for channel estimation and equalization, referred to as PUCCH-DMRS. The PUCCH DMRS symbols was defined by equation 4.17 and 4.18, the c_{init} for PUCCH is defined in equation 4.27, note that the c_{init} for PUCCH is identical to the PDCCH formula. 4.22:

$$c_{init} = (2^{17}(N_{symb}^{slot}n_s + l + 1)(2N_{ID} + 1) + 2N_{ID}) \, mod \, 2^{31} \tag{4.27}$$

where l represents the number of slot-symbols used ($l = 2$), $N_{symb}^{slot} = 14$ denotes the number of symbols within a slot. Additionally, n_s signifies the number of slots in a radio frame; for $\mu = 0$, $n_s = 1$, and N_{ID} represents the cell number. The key divergence from the PDCCH is that the PUCCH utilizes two slot symbols, unlike the PDCCH, which uses only a single slot symbol.

The allocation of PUCCH-DMRS for PUCCH Format 2 is simple. Due to the limited number of DMRS symbols, the allocation simplifies to Resource Elements $1, 4, 7, 10$ from the start Resource Element within each Resource Block allocated, resulting in a total of 8 allocated DMRS symbols. Similar to the SRS, the PUCCH symbols have been shifted to the middle of the Resource Grid, all starting from Resource Block 12. The Figure 44 illustrates the allocation of the PUCCH-DMRS on the Resource Grid.

In Figure 45, the symbols allocated for PDCCH-DMRS, along with the retained PDCCH symbols and the SRS symbols intended for the synchronization process, are depicted.

Even without HARQ implemented, the UE sends an ACK/NACK to the gNodeB. The gNodeB then tries to resend the packet up to three times. If it retransmits, the 'New
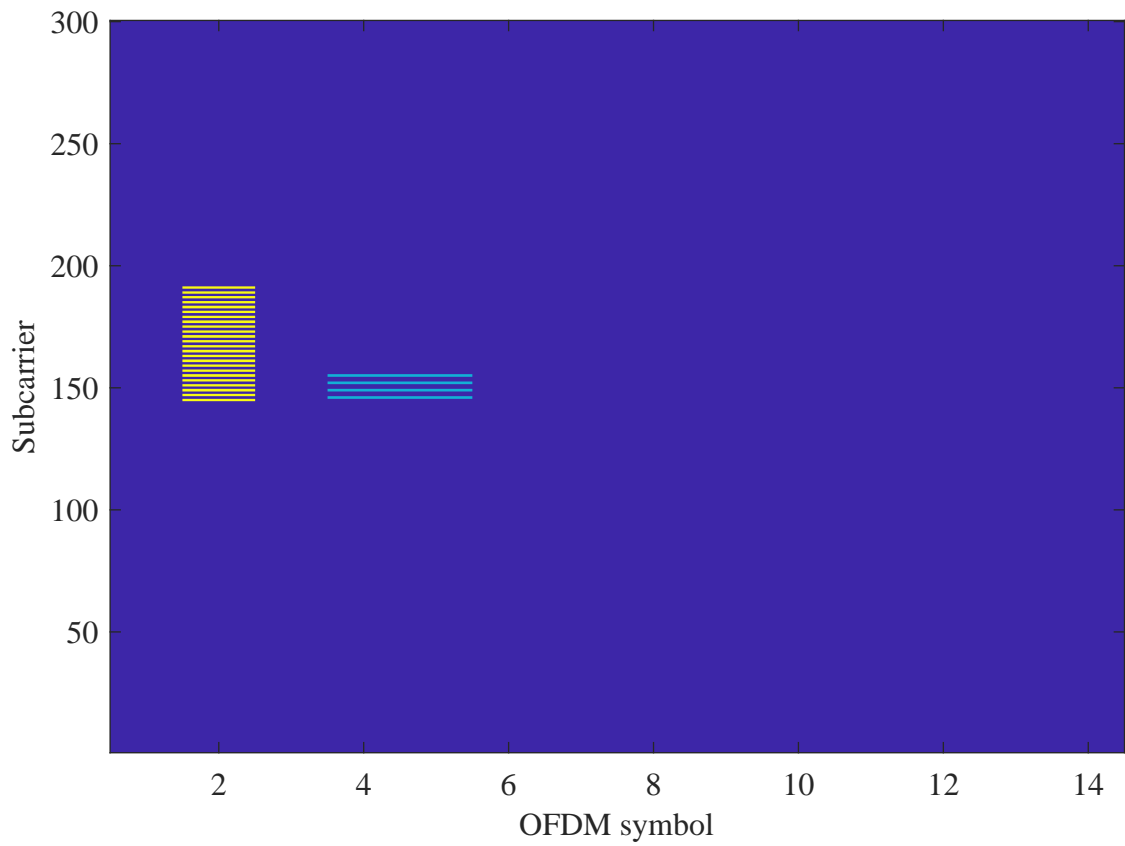
Figure 44 – PUCCH DMRS allocation into a Resource Grid with SRS symbols
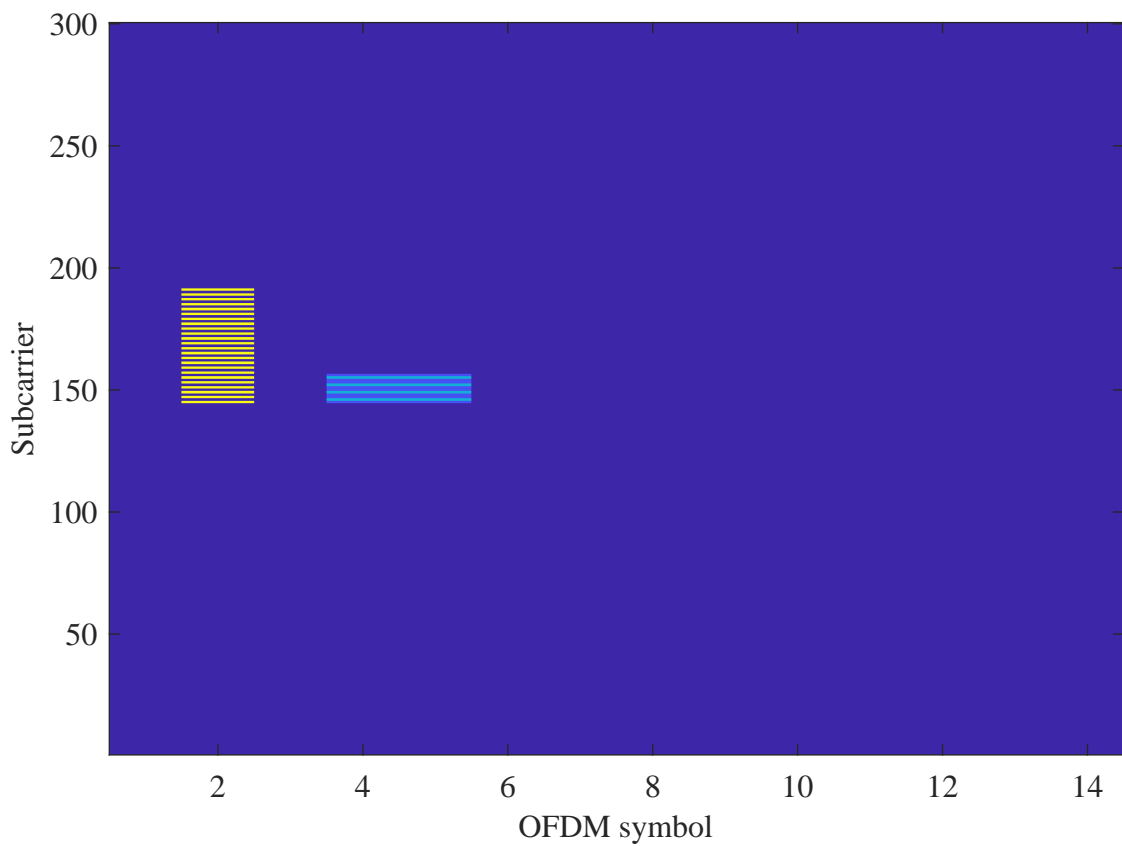
Figure 45 – All PUCCH symbols, comprising both DMRS and regular PUCCH symbols, have been allocated within the Resource Grid, alongside the SRS symbols.

Data' field in the DCI (shown in Table 4) becomes zero. After three attempts without receiving an ACK from the UE, the gNodeB moves on to the next Radio Frame. The reader may note that does not exist any ACK/NACK field in DCI from the gNodeB to inform the UE about successful reception. Indeed, in the prototype, the flow control was only implemented for the Downlink. Moreover, the PUCCH becomes the most important channel in the Uplink. The implementation of PUSCH happened opportunistically, as the UL-SCH was already established; it was merely mapped up to PUSCH and used for payload transmission, lacking reception control.

Unlike PDCCH-DMRS, the symbols and indices for PUCCH-DMRS are obtained by two separate functions: nrPUCCHDMRS [95] and nrPUCCHDMRSIndices [96]. These two functions, in turn, utilize the data structures nrCarrierConfig and nrPUCCHConfig, where the following parameters are defined: N_{ID}, n_s, l. There is also a parameter called symbol allocation, intended to indicate which columns of the Resource Grid will be used; in this case, SymbolAllocation = [3,4]. Finally, the functions nrPUCCH [97] and nrPUCCHIndices [98] perform modulation of the bits [ACK;NACK], repeated until they form a set of 32 bits in QPSK modulation, for mapping onto the Resource Grid matrix.

4.3.3.6 Physical Uplink Shared Channel - PUSCH

According to reference [47], the scheduling of the Physical Uplink Shared Channel (PUSCH) is typically based on DCI Formats. However, the only considered implementation so far has been DCI Format 2. Therefore, for simplification purposes, the PUSCH will be scheduled in the next nine subsequent subframes in the Frame Allocation. Similar to other channels, the PUSCH comprises data symbols and DMRS (Demodulation Reference Signal) symbols. For the PUSCH DMRS, they are generated analogously to PDSCH DMRS. In this case, the Resource Elements of the PUSCH DMRS will be mapped by the symbols using the equation 4.17, with initialization c_{init} as proposed in equation 4.23. Furthermore, the PUSCH DMRS will be configured in the same way as PDSCH DMRS, with mapping type A, configuration Type 1, length $L = 1$, and one additional slot symbol for DMRS. Figure 46 shows the allocation of DMRS symbols within the Resource Grid.

Similar to the PDSCH, the PUSCH utilizes the UL-SCH transport channel, which works just like the DL-SCH. Here, the payload bits of the PUSCH undergo a series of steps: initial error checks (CRC attachment), segmentation into smaller units (Code Blocks), additional error checks, a specific type of encoding (LDPC), and then adjustment of data rate (See 4.3.2.1). Furthermore, the modulation method and data rate used align with the instructions received from the gNodeB via the Downlink Control Information (DCI) in PDCCH, as discussed in section 4.3.3.5. In the remaining 9 subframes, a payload was applied to the available Resource Elements, excluding the DMRS. Figure 47 illustrates the complete allocation of the Uplink Resource Grid after the allocation of PUSCH symbols.
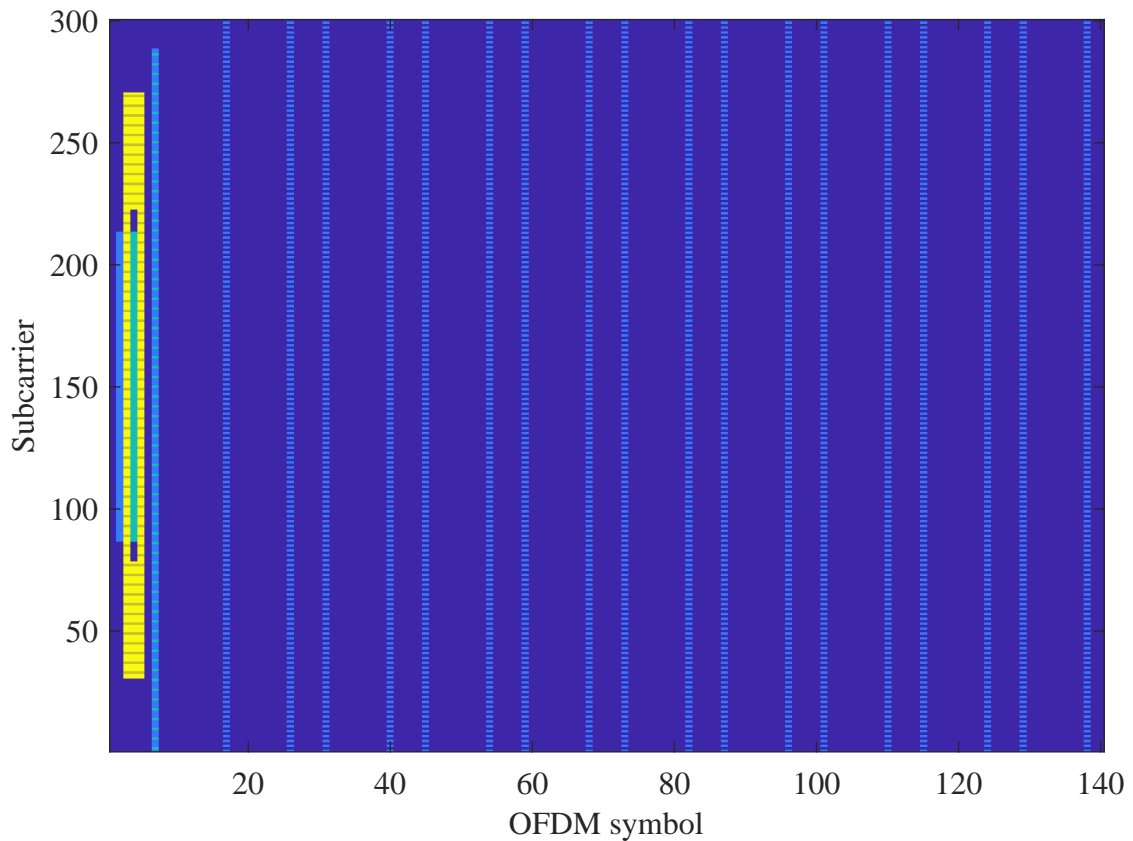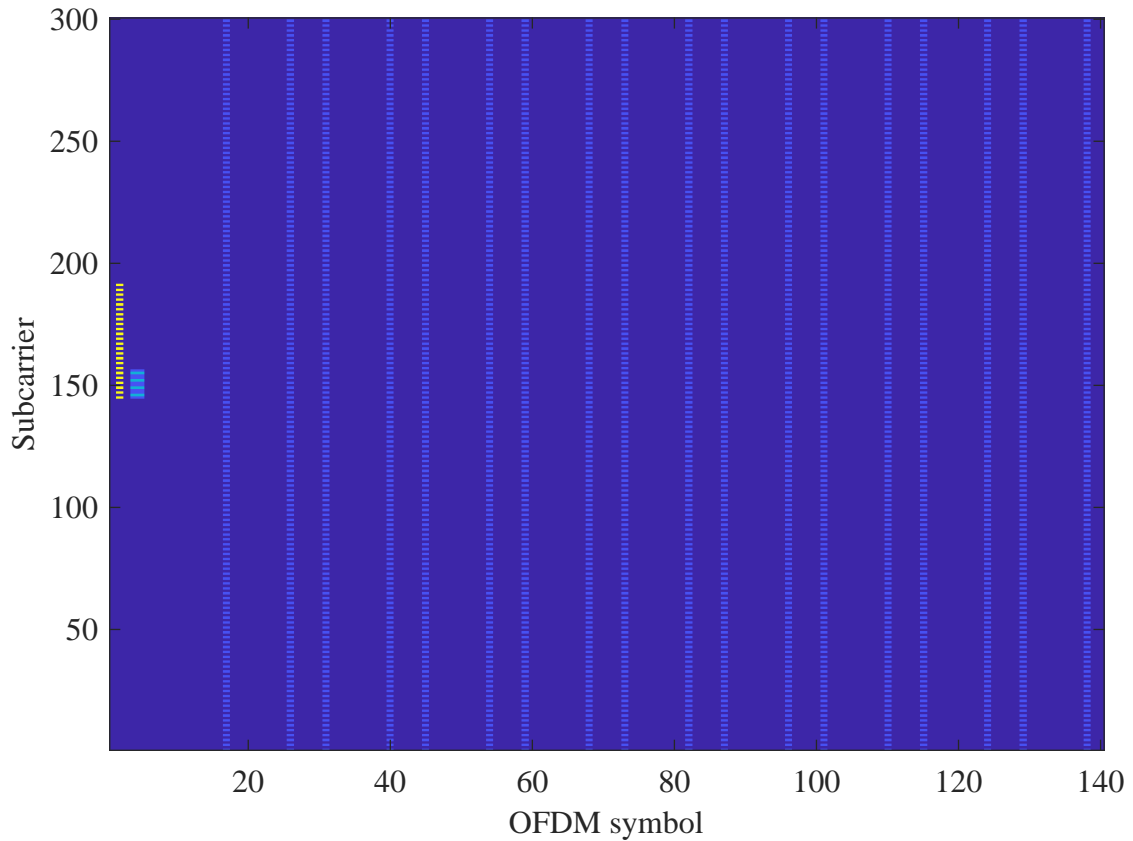
Figure 46 – Allocation of PUSCH-DMRS elements with mapping type A, configuration type 1, and length L = 1 and a additional DMRS.

In section 4.3.3.5, it's highlighted that the primary channel for sending ACK/NACK bits in the Uplink is the PUCCH. The addition of PUSCH here was due to its similarity to PDSCH. During the experiments, when the UE sends ACK/NACK to the gNodeB in the Uplink, random data is inserted into the nine assigned PUSCH parts. This serves to demonstrate the Uplink's potential. The primary focus of this project is the utilization of the VLC channel and in-depth study of the Uplink. Exploring methods for controlling data flow and rectifying errors using RF will be considered for future research.

The allocation of symbols for PUSCH is entirely analogous to PDSCH. In this case, for the uplink, the functions nrPUSCHDMRS [99] and nrPUSCHDMRSIndices [100] are used. The parameterization of the nrCarrierConfig and nrPUSCHDMRS structures is also analogous to the downlink case. Furthermore, the functions that digitally modulate the uplink symbols also follow the same concept as the downlink. For the uplink, the functions nrPUSCH [101] and nrPUSCHIndices [102] are used, with identical parameterization to PDSCH.

4.3.3.7   Datarate calculation

As proposed in [103] the maximum theorical datarate in 5G NR is exihibited in equation 4.3.3.7.

$$DR_{Mbps} = 10^{-6} \sum_{j=1}^{J} (v_{layers}^{(j)} Q_m^{(j)} f^{(j)} R \frac{N_{PRB}^{Bw(j),\mu} 12}{T_s^{\mu}} (1 - OH^{(j)}))$$ (4.28)

In the experiment, where J represents the maximum number of aggregated carriers, only $J = 1$ is considered. v_{layers} denotes the number of layers, essentially indicating how many Resource Grids can be simultaneously transmitted for this experiment ($v_{layers} = 1$). f indicates a scaling factor from high layers to adapt the UL-DL TDD, not used in this case because the UL only answer DL calls. The term Q_m expresses the level of employed digital modulation, such that $Q_m = \log_2(M)$. R is the coderate parameter. N_{PRB} indicates the number of Resource Blocks, and for the set numerology, $\mu = 0$, implying SCS = 15 kHz and bandwidth Bw = 5 MHz, hence $N_{PRB} = 25$ Resource Blocks. T_s^{μ} stands for the average symbol time for a given numerology, where $T_s^{\mu} = \frac{10^{-3}}{14.2^{\mu}}$. Lastly, the term OH represents the overhead from the utilized signaling, considering the use of PDSCH (Physical Downlink Shared Channel), where 2 slot-symbols allocate half of their subcarriers for PDSCH-DMRS signals. Therefore, $OH = \frac{2 \times 150}{14 \times 300} \approx 0.08$. With these considerations the equation is simplified to equation 4.29.
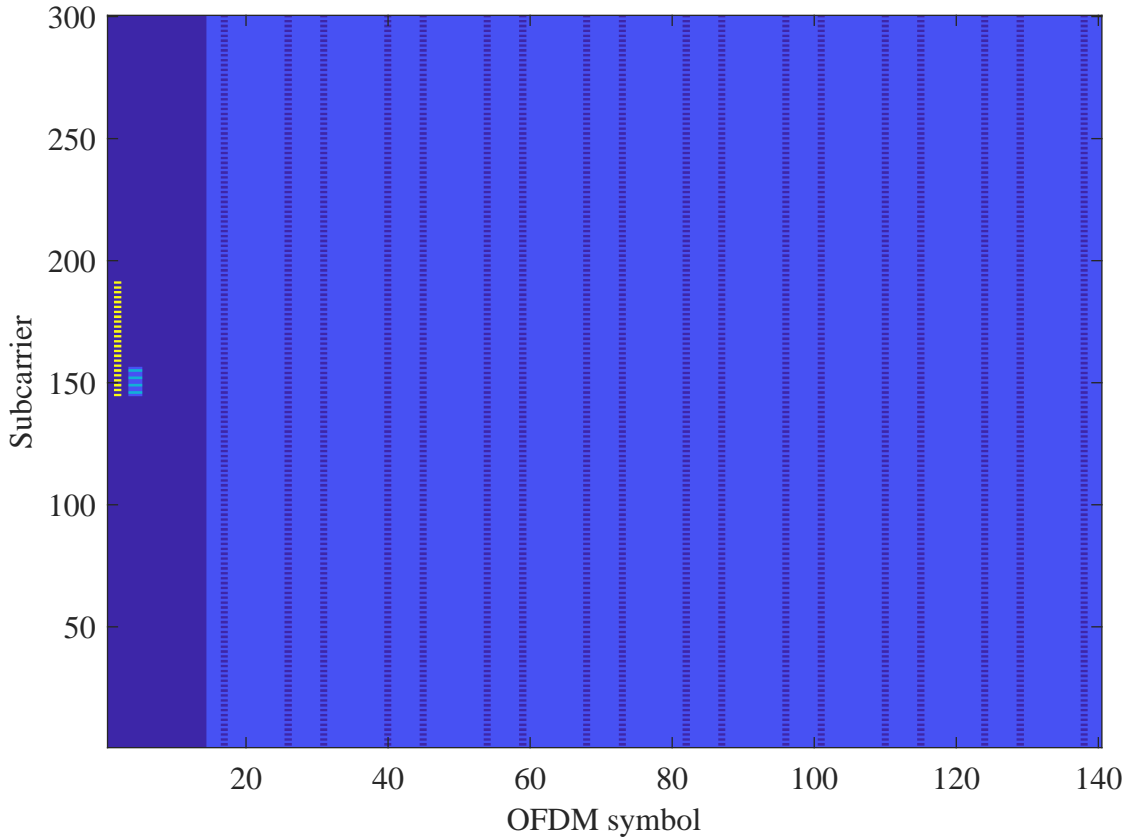
Figure 47 – The Uplink Resource Grid (SRS + PUCCH + PUSCH)

$$DR_{Mbps} = 10^{-6} \sum_{j=1}^{1} (1) Q_m^{(j)} (1) R \frac{25 \times 12}{T_s^{\mu}} (1 - (0.08))$$

$$DR_{Mbps} = 10^{-6} (log_2(M) \times R \times \frac{300}{7.14 \times 10^{-5}} \times 0.92) \qquad (4.29)$$

$$DR_{Mbps} = 10^{-6} (log_2(M) \times R \times \frac{300}{7.14 \times 10^{-5}} \times 0.92)$$

$$DR_{Mbps} = 3.86 \times R \times log_2(M)$$

It's crucial to emphasize that when considering parameters such as coderate and overhead rate, Equation 4.29 actually represents the transmission rate of information. This differs from stating the total data rate transmitted, which would involve the transmission of LDPC parity bits and DMRS subcarriers. Consequently, a more comprehensive assessment of the overall transmission rate, capturing the intricacies of the data transmission process in greater detail, would be obtained.

5 Experimental Setup

The main components, configurations and functions of the elements involved in the experimental setup are described in this Chapter. The chapter is subdivided by the means of the communication channels (VLC and RF), as well as the combination of both on the full-duplex prototype. The setup limitations are presented in order to pave the way towards future improvements.

5.1 Visible Light Communication Setup

Figure 48 provides a high-level overview of the primary components used in the VLC system. Firstly, it should be note that the ADALM 2000 module, used in both gNodeB and User Equipment sides, is responsible for generating the OFDM 5G NR signals. These 5G NR signals require amplification and a DC level to achieve a unidirectional current, preventing clipping by the LED. The LED acts as a transmitter, while a set of lenses collimates the light beams in order to concentrate the maximum luminous power onto the photodetector area. The photodetector, in turn, converts the light signal into an electrical one. However, the electrical signal in this instance has a very low amplitude, thus requiring a transimpedance amplifier (TIA) to, among others, adapt the received signals to the UE's ADALM 2000 amplitude detection range. The subsequent Subsections provide details of each modules depicted in Figure 48.

5.1.1 ADALM 2000 - M2K

The ANALOG Devices ADALM 2000 board was chosen due to its availability and because it meets the project's needs for streaming 5G NR signals using the VLC channel. The ADALM2000 (M2K) Active Learning Module stands as an affordable USB-powered data acquisition module. Equipped with 12-bit ADCs running at 100 MSps and DACs operating at 150 MSps, this module excels in collecting and producing analog signals. Additionally, the ADALM 2000 hosts an embedded Linux Operating System
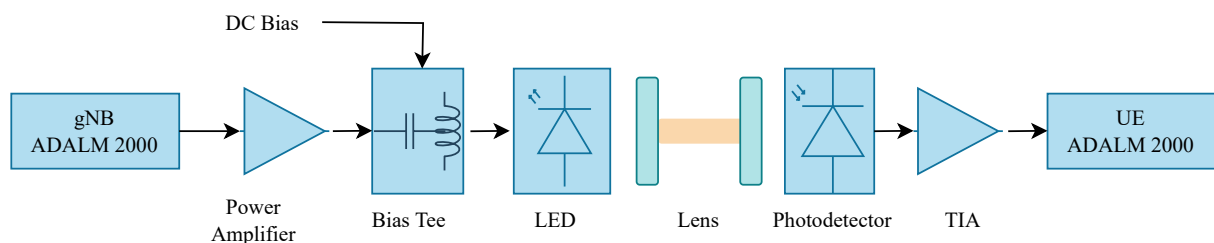
Figure 48 – High Level Block Diagram of a Visible Light Communications Setup

Figure 49 – a) ADALM 2000 Evaluation Board Overview. b) Digilent BNC Adapter Overviewn. c) Connection between ADALM 2000 and BNC Adapter Board

and internal DDR Memory, as detailed in [104]. The ADALM 2000 can be connected with MATLAB software through the USB Port and an Analog Devices library called Industrial Input/Output (IIO), facilitating data streaming between the computer and the ADALM2000, as outlined in [105]. Figure 49.a) displays the ADALM2000 Evaluation Board Kit. It's worth noting in Figure 49.a) that there are no specific connectors (SMA, BNC, TNC, among others) commonly used in communication channels. Consequently, an adapter had to be introduced, as depicted in Figure 49.b).

Figure 49.b) illustrates the utilization of the BNC Adapter manufactured by Digilent [106]. This BNC Adapter board accommodates four BNC connectors, more specifically two for input and two for output, all configured with a matched impedance of 50 Ω. As mentioned in [107], while the BNC board was initially intended for Scope Probes, this project exclusively utilized the BNC 50 Ω cables. The BNC adapter also offers the flexibility to operate in either AC or DC coupling, which is controlled by a blue jumper. Throughout this project, a consistent employment of DC coupling was ensured. Figure 49.c) exhibits the connection setup between the ADALM 2000 and the Digilent BNC Board. As described in the ANALOG Devices Documentation provided in [104], the ADALM2000 offers the following fundamental configurations:

- two-channel oscilloscope with differential inputs;

- two-channel arbitrary function generator;

- 16-channel digital logic analyzer supporting 3.3V CMOS and 1.8 V or 5 V tolerance, operating at 100 MS/s;

- 16-channel pattern generator employing 3.3 V CMOS at 100 MS/s;

- 16-channel virtual digital I/O;

- two input/output digital trigger signals, designed to interlink multiple instruments, operating at 3.3 V CMOS;

- two-channel voltmeter catering to AC, DC, and ± 25 V measurements;

- Network analyzer enabling Bode, Nyquist, Nichols transfer diagrams of a circuit, with a range from 1 Hz to 10 MHz;

- Spectrum Analyzer facilitating power spectrum and spectral measurements, encompassing parameters like noise floor, SFDR, SNR, and THD;

- Digital Bus Analyzers for SPI, I2C, UART, and Parallel interfaces;

- two programmable power supplies spanning 0 V to +5 V and 0 V to -5 V.

Figure 50 displays the internal architecture of the device [108]. It's evident that the hardware is equipped with a Xilinx Zynq XC7Z010 chipset, comprising an FPGA core and an additional core, the latter being an ARM A9 processor [109]. The ARM processor plays a pivotal role in the processing layer that incorporates the embedded Linux operating system. Furthermore, the presence of a 512MB DDR memory dedicated to the file system purpose.

Furthermore, in Figure 50, the presence of the AD9963 chip is notable. This chip features a dedicated clock generator facilitated through the ADF4360-9 [108]. As outlined in [110], the AD9963 specifies an output sampling rate of 150 MSps for the DAC. However, this value undergoes division by 2 in an interpolation process, resulting in an actual maximum sampling rate of 75 MSps. In contrast, the AD9963's ADC operates at 100 MSps. Additionally, the AXI_AD9963 entity is depicted in Figure 50, described in Hardware Description Language (HDL), defining the interface with the ADD963 chip. This interface can handle a Pseudo Random Binary Sequence (PRBS), predefined patterns, or the logical buffer within the memory accessed via Direct Memory Access (DMA). One of the primary focus of this work lies in establishing communication between a computer equipped with MATLAB, connected via USB to the ADALM 2000. The aim is to write data into a buffer and subsequently forward this buffer to the AXI_AD9963 interface for transmission to the analog port using DMA. This process also applies for data acquisition by the AD9963, which is then sent back to the computer via USB.
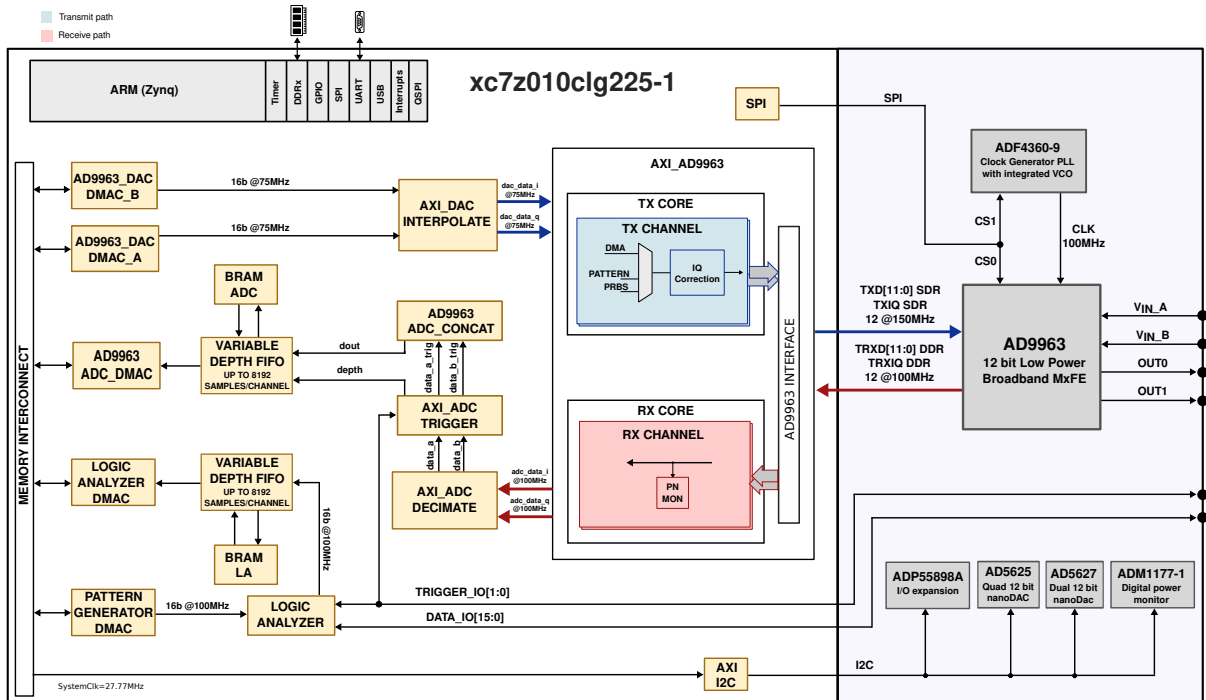
Figure 50 – ADALM 2000 Low Level Overview

For data transfer control, the Analog Devices-developed Linux platform known as libiio is employed. Libiio bridges this gap by offering comprehensive device abstraction and managing various IIO internals. It is a cross-platform tool that also offers different language bindings, enabling control of IIO devices from MATLAB [111]. The library abstracts the intricate low-level hardware details, and offers a straightforward yet comprehensive programming interface suitable for advanced projects. Linux Libiio comprises a high-level API and multiple backends, as outlined in Figure 51 [112]. These backends include the local backend, interfacing with the Linux kernel through the sysfs virtual filesystem, and the network backend, connecting to the iiod server via a network link.

The IIO Daemon (IIOD) server serves as an exemplary application utilizing libiio. It establishes a libiio context utilizing the local backend, sharing it across the network for any client application using the "network"backend of libiio connected to the server. Both Libiio and IIOD can be employed with a pre-compiled image -providing multiple avenues for data streaming. In this context, the primary Client Application was MATLAB, communicating with the IIOD Server through LibIIO Windows. MATLAB was chosen due to its extensive array of 5G NR functions developed within the 5G NR Toolbox.

Figure 52.a) depicts the setup assembly for characterizing the ADALM 2000 + BNC Adapter combination. In this configuration, the analog output was reconnected to the analog input using a 50 Ω impedance coaxial cable. Figure 52.b) displays the obtained frequency response. It is noticeable that the response remains fairly stable up to 10 MHz, with a slight low-pass characteristic after 6 MHz, resulting in minor attenuations at higher
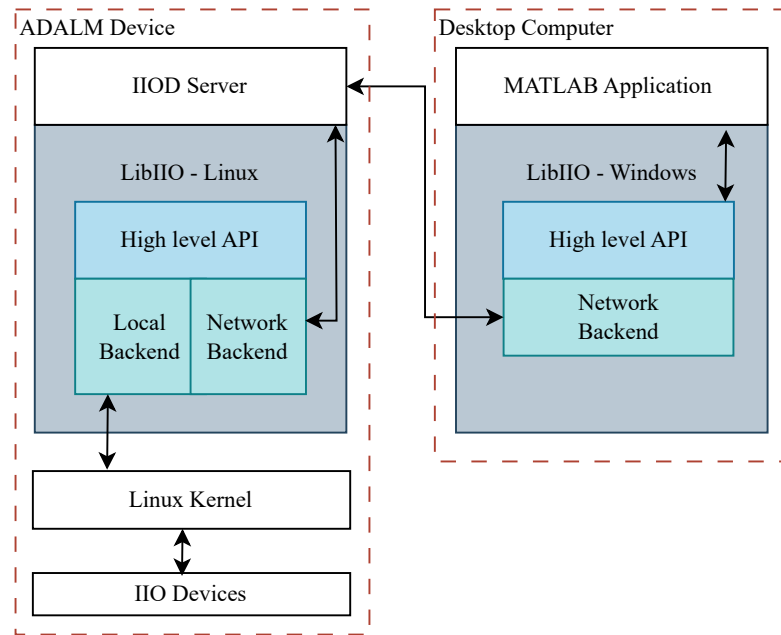
Figure 51 – Connection Schematic of Computer interfacing to ADALM Device using libiio
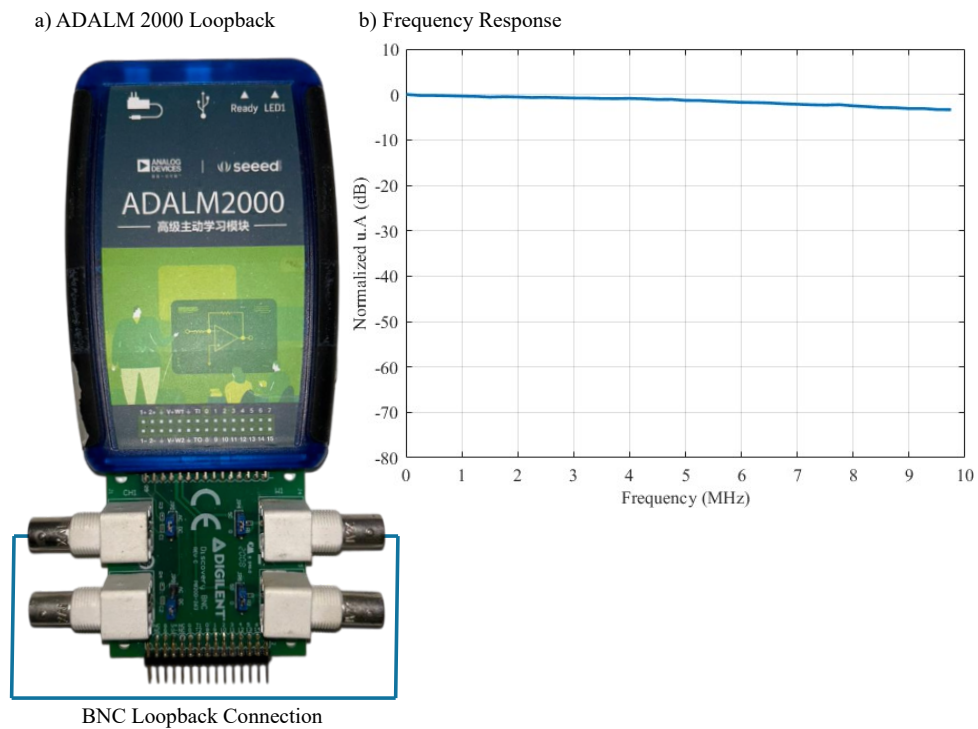
Figure 52 – a) Charecterization Loopback setup. b)Measured frequency response.

frequencies in the signal. The frequency response was obtained by generating various tones spaced 50kHz apart in frequency. These tones are generated in the time domain, and during reception, the energy of the impulse generated at each frequency is measured by calculating the FFT of the received tone. This process is carried out across the entire scanning range, and the result is displayed in the Figure 52.b).

Figure 53 – Juntek DPA-2698 Power amplified employed in the VLC Transmitter

5.1.2   Power Amplifier

The Juntek Model DPA-2698 power amplifier was used to amplify the electrical OFDM signals, with details illustrated in Figure 53. This particular amplifier features a maximum output of 25 Vpp and a 0.5 A output current, along with a 6 dB gain specifically designed for transmitting the 5G NR OFDM waveforms. As stated in [113], it is recognized as a low-distortion amplifier suitable for industrial and medical applications, as well as product line testing. To manage its high power output, the DPA-2698 is enclosed in aluminum and equipped with a fan to dissipate energy and regulate internal temperature. Figure 54.a) shows the characterization setup involving the ADALM 2000 + BNC Adapter + Juntek Amplifier, and Figure 54.b) presents the frequency response obtained from this arrangement. Notably, the Juntek amplifier's bandwidth spans 10 MHz, thereby causing minimal attenuation within the frequency response range between 0 and 10 MHz.

5.1.3   Bias Tee

The generation of OFDM signals was described in Chapter 3, also considering that these signals possess complex coefficients, which were handled by the Digital Up-converter. However, it's worth noting that the amplitudes of the OFDM signals reach both positive and negative levels. While a signal with positive amplitudes generates a current flowing through the LED, resulting in luminous power, the negative amplitudes would be clipped by the LED's PN junction. To address this issue, Section 2.1 introduced LED polarization by inserting a DC level, ensuring that all signals produce unidirectional currents.

To directly modulate the power emitted by the LED, the signal from the ADALM 2000 needs to be combined with the direct current driving the LED. For this purpose, the Bias Tee from Picosecond Pulse Labs (Model 5575A) shown in Figure 55 was employed. Notable characteristics include a bandwidth extending from 10 kHz to 12 GHz, a low rise time (30 ps), a resistance of 0.6 Ω, and limiting the low-frequency response for currents above 20 mA [114].

a) ADALM 2000 Loopback

b) Frequency Response
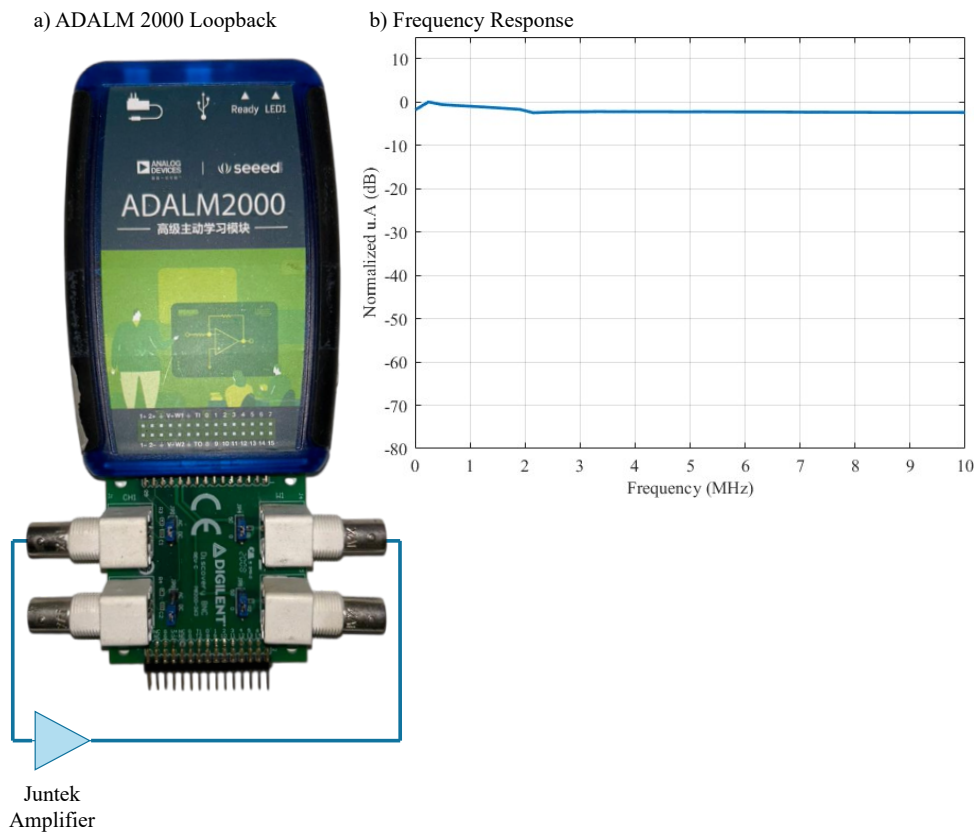
Juntek
Amplifier

Figure 54 – a) Setup used in Loopback + Juntek Amplifier charecterization. b) Measured frequency response.

DC In

AC In

AC + DC
Out
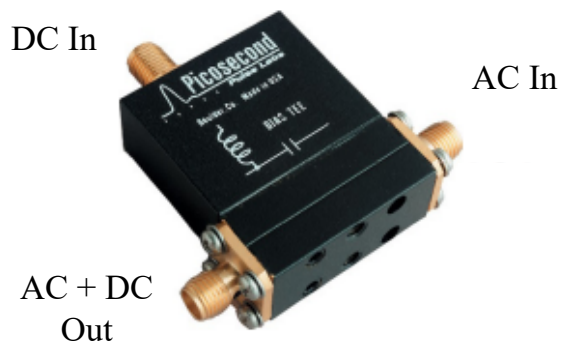
Figure 55 – Picosecond Pulse Labs Model 5575A for DC bias in the VLC setup. The LC combination imposes a high-pass filter characteristic on the signal entering the AC In port.
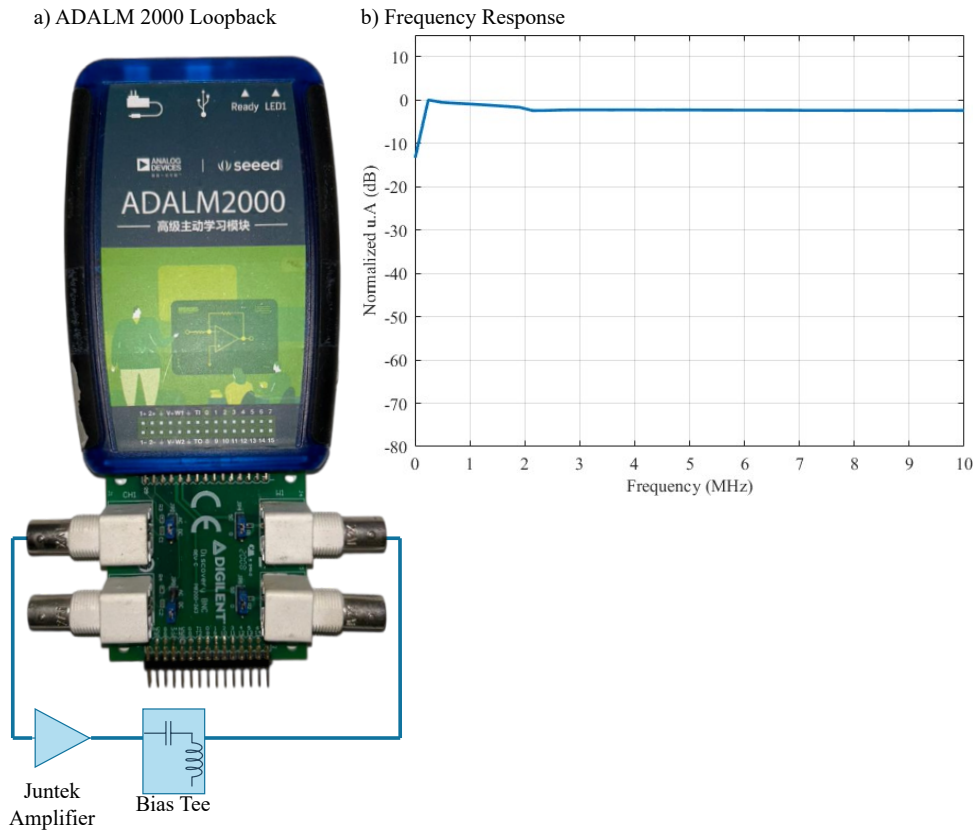
Figure 56 – a) Characterization of the Loopback + Juntek Amplifier + Bias Tee setup. b) In the Frequency Response, the -3dB frequency is evident at around 200 kHz, stabilizing into a steady-state around 300 kHz.

Due to the characteristics of an LC circuit as depicted in Figure 55, the Bias Tee imposes a high-pass filter characteristic on the signal entering the AC In port. As seen in the Frequency Response graph in Figure 56, this high-pass filter characteristic is clearly observed. It's notable that the response reaches a -3dB frequency at approximately 200 kHz and settles into a steady-state around 300 kHz. In addition to the necessity for real signals, this characteristic further emphasizes the need for the Digital Up-converter as it allows circumventing the attenuation issue near 0 Hz.

5.1.4 LED Transmitter

In this transmitter, the white LED LXML-PWC2 from LumiLED is used. To power the LED, a 50 Ω female BNC connector was installed. The LED/Heatsink assembly was adapted to fit into a lens holder from PHYWE, ensuring the stability of the VLC transmitter. The Figure 57 depicts the assembly of the LED in a holder, the insertion of the heatsink, and the BNC connection for signal acquisition.

As shown in Figure 58 from [115], the optical spectrum exhibits two peaks of radiant intensity. The first peak occurs in the blue light range, between 450 to 470 nm, and the second peak (with lower intensity compared to the first) occurs in the yellow
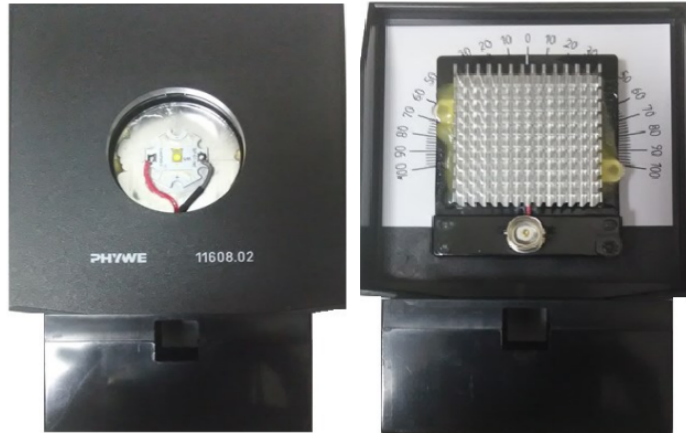
Figure 57 – The assembly of the LXML-PWC2 LED onto a PHYWE mount with the integration of a heat sink and a connection for a BNC cable.
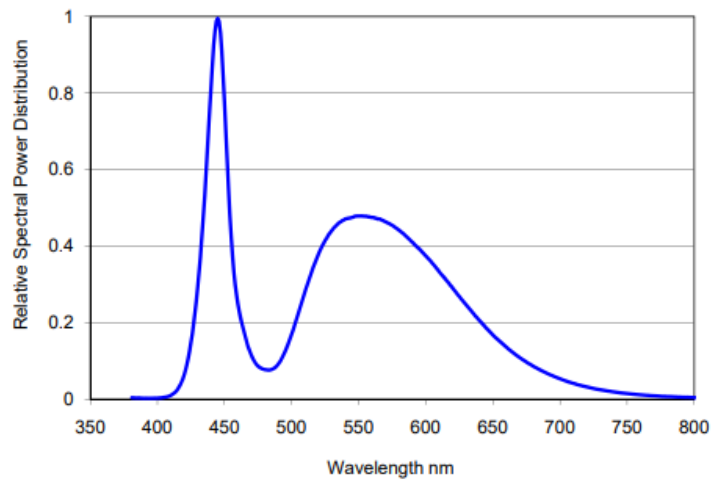
Figure 58 – Optical spectrum of the LED obtained from the manufacturer's datasheet

light range, between 565 to 580 nm. According to the manufacturer, this combination of wavelength peaks produces the Cool White color.

As discussed in Section 2.1, the LED exhibits non-linear behavior and saturation characteristics. Figure 59 a) illustrates the experiment conducted to assess the linearity of the LXML-PWC2 LED. A luxmeter was employed to measure luminous flux while the voltage source increased the forward current flowing through the LED. In Figure 59 b), it's evident that as the current rises beyond 1200mA, saturation in illuminance becomes noticeable. Furthermore, it's observed that as the current surpasses 1200mA, a substantial increase in the polarization current is required to produce a minimal increment in lux.

5.1.5 The Optical Collimator Lens

The communication channel used is free space. The optical link is configured as Line of Sight. As it is an LOS channel, the received power at the photodetector of the photodetection system remains approximately constant and signals reach the receiver
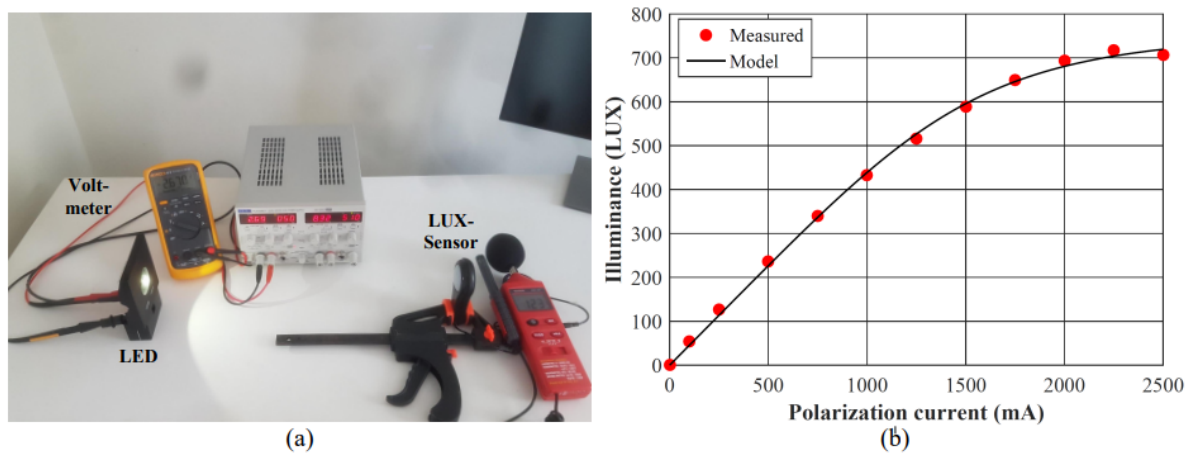
Figure 59 – a) The setup for collecting the LED saturation curve. b) Illuminance vs Polarization current (mA) curve demonstrates that the LXML-PWC2 LED exhibits saturation in illuminance after reaching 1200mA.

Figure 60 – Lenses used in optical collimation: a lens with f=+100mm was used for the Transmitter, and a lens with f=+50mm for the Receiver.

almost simultaneously, meaning multipath components are practically negligible.

For Visible Light collimation in the transmission channel, two biconvex glass lenses from the manufacturer PHYWE are used. These lenses exhibit converging behavior, where a ray incident parallel to the lens axis refracts through the focus, and a ray passing through the focus refracts parallel to the axis. The VLC transmitter lens has a focal length of +100 mm, while the receiver lens has a focal length of +50 mm. Figure 60 illustrates the two biconvex lenses used in beam collimation. Two lens supports from the mentioned manufacturer are used for positioning the lenses.

5.1.6 Custom Manufactured Optical Receiver

The PIN photodiode serves as a pivotal component within the photodetection system, responsible for converting optical signals into electrical ones. Illustrated in Figure 61, the photodetection system, developed collaboratively by LabTel and 2SOLVE researchers [116], is designed to detect and process optical signals from the VLC channel.

The initial stage of the photodetection system employs the OSRAM PIN SFH2400-
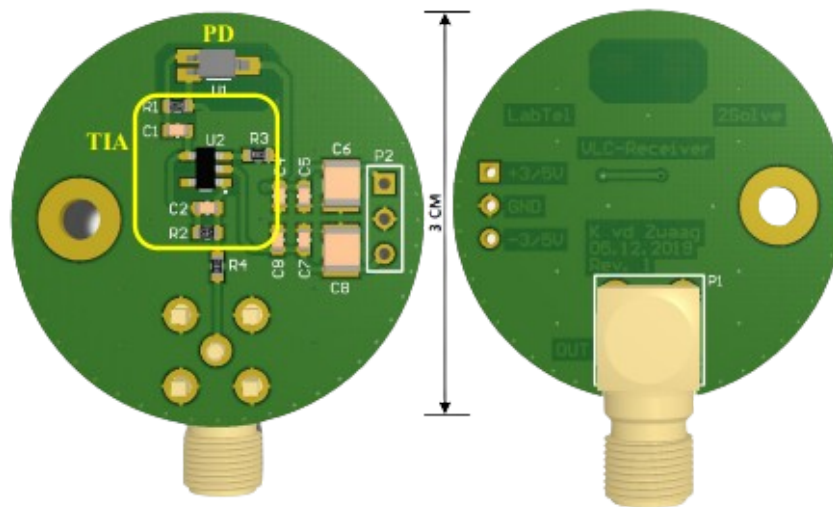
Figure 61 – Custom-designed Optical Receiver, based on the OSRAM PIN SFH2400-Z, developed by LabTel in partnership with 2Solve

Z photodiode. Subsequently, a transimpedance amplifier (TIA) is utilized in the second stage to convert the generated photocurrent into a voltage signal, amplifying it thereafter. The TIA configuration, utilizing the LMH6629 operational amplifier, boasts a bandwidth of 100 MHz and a gain of 1.8 kΩ. More details about the custom Photodetector schematics is available in Appendix D.

Figure 63 depicts the frequency response of the complete VLC setup, encompassing the amplifier, Bias tee, LED, lenses, and Custom photodetector. For a 5MHz centered OFDM 5G NR signal, with a bandwidth starting at 2.75MHz (-11.5dB attenuation) and ending at 7.25MHz (-25dB attenuation), substantial attenuation is evident.

For instance, a 1V amplitude signal would be reduced to approximately 70mV at 2.75MHz. However, as per the ADALM 2000 documentation, its resolution stands at $5/2^{12} = 1.3mV$ per division. In this scenario, at the 70mV range at the beginning of the band, the ADC would only utilize 6 bits to measure analog values, resulting in quantifying up to 83mV ($2^6 \times 1.3mV = 64 \times 1.3mV = 83mV$).

To address this issue with limited signal reading from the Photodetector, an additional amplification stage was introduced using the transimpedance amplifier TQP3M9037-LNA, which offers a gain of 20 dB, operational bandwidth ranging from 0.1MHz to 6GHz, and ultra-low noise as specified in [117]. The 20dB gain represents ten times the input value, enabling the utilization of the 0.7V range and allowing for the use of 10 bits of resolution. This modification resulted in significantly improved experimental outcomes. Figure 62 provides an overview of the TQP3M9037-LNA amplifier integrated into the extra amplification stage.

Finally, Figure 63 a) presents a schematic used to obtain the frequency response and

Figure 62 – The TQP3M9037-LNA was employed in the supplementary amplification stage for the photodetector.

63 b) shows the frequency response graph of the entire VLC setup. It should be noted that there's significant attenuation shortly after the 1 MHz frequency, extending to -30dB at 10 MHz. Severe attenuations are observed, justifying the insertion of an extra amplification stage. However, even though higher signal levels are achieved at higher frequencies using the extra amplification, dealing with this extensive attenuation during reception is necessary. Estimation of the channel through pilots sent in the DMRS symbols will be used to estimate the channel, and the equalizer will compensate for all the attenuation shown in Figure 63 b), ensuring correct Downlink reception

5.1.7 Downlink Detailed Transmission Blocks

In this section, a detailed discussion is presented regarding the 5G signal transmission and reception model through the visible light communication channel.

The waveform produced by a baseband OFDM signal, as denoted in Equation (3.7), comprises both real and complex coefficients. Some SDR devices utilize two internal paths to modulate these coefficients into two sinusoidal carriers, one cosine and the other sine, respectively. Subsequently, the sum of these two orthogonal signals is sent to transmitter element [118]. However, it's worth noting that, in this scenario, two Digital-to-Analog converters (DACs) are necessary for the baseband to passband conversion. Another approach, employing only one DAC, is depicted in Figure 64.a) in a strcuture called Digital Up-Converter (DUC). However, the digital carrier f_d is significantly lower than an analog carrier, since the DAC must have a sufficient sampling rate to generate the analog signal in the passband. Increasing the frequency of f_d requires an exceptionally fast DAC, consequently escalating project costs. The components $mr_1(m)$ and $mr_2(m)$ represent digitally matched-rate components to the Digital Carrier in-phase and quadrature phases, respectively. The Lowpass Digital Filter ensures that the signal is confined within the frequency band limits and does not produce any additional spectrum copies.
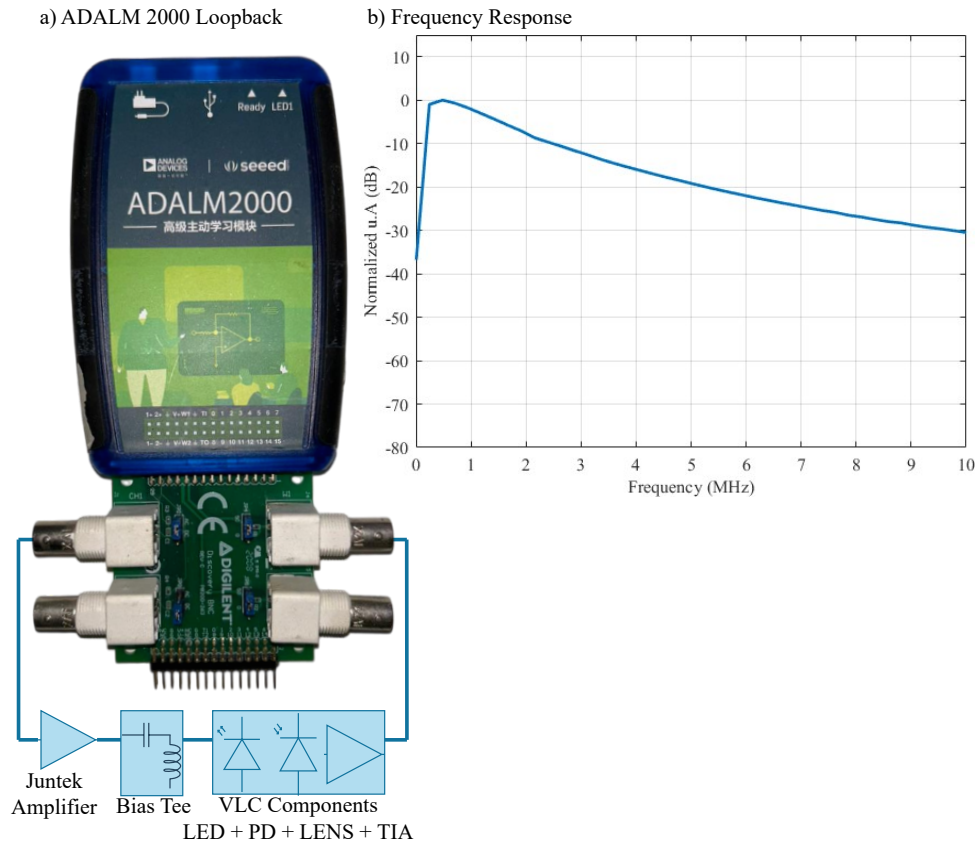
Figure 63 – a) Characterization of the Loopback + Juntek Amplifier + Bias Tee setup +
Optical Devices. b) Significant attenuation is evident from 1 MHz, extending
to 10 MHz, reaching -30dB
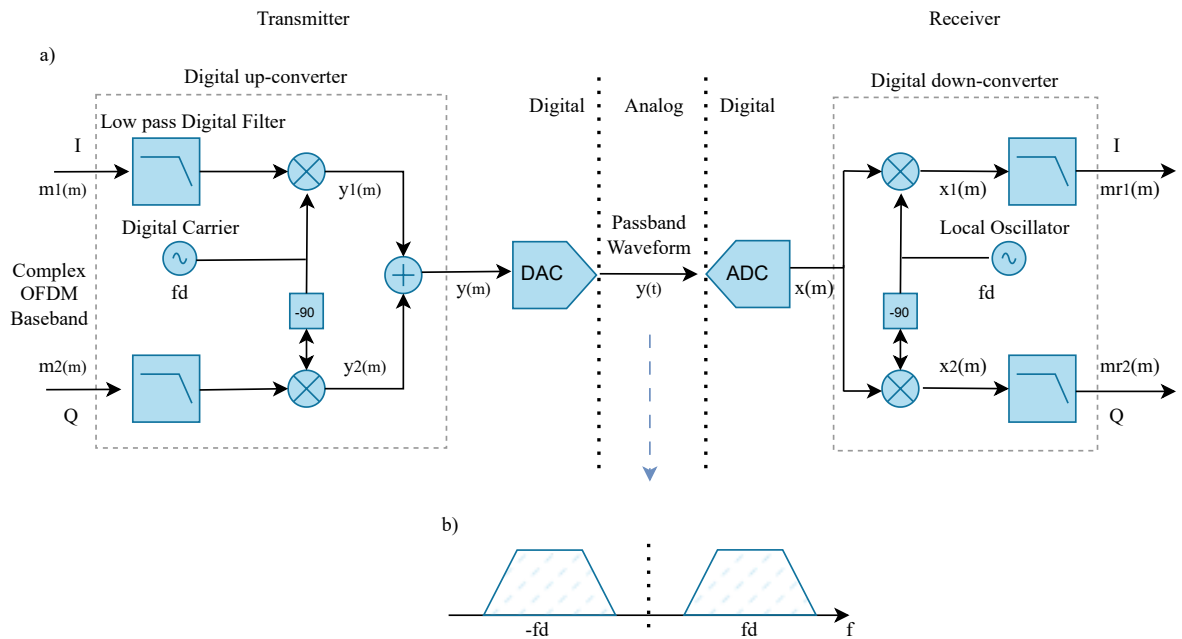
Figure 64 – a) Digital up-conveter architecture. b) Up-converted spectrum with two components centered at f_d and $-f_d$.

In Figure 64a) at the transmitter consider the real part of an M-QAM or M-PSK symbol at the input I, represented by the discrete component $m_1(m)$, and the imaginary part at the input Q, represented by $m_2(m)$. Both components undergo filtering by a low-pass digital filter to eliminate undesired frequency components. Subsequently, each component is mixed with two orthogonal digital carriers at a frequency f_d, as detailed and analyzed in [119]. This procedure results in digitally modulated signals $y_1(m)$ and $y_2(m)$, formulated as shown in Equation 5.1:

$$
\begin{aligned}
y_1(m) &= m_1(m)cos(2\pi f_d m) \\
y_2(m) &= m_2(m)sin(2\pi f_d m)
\end{aligned}
\tag{5.1}
$$

The signal $y(m)$ is formed by the sum of the components $y_1(m)$ and $y_2(m)$. After the addition of the two components by a processing unit, conversion to an analog value is performed through the digital-to-analog converter shown in Figure 64a), resulting in the continuous signal $y(t)$. The signal $y(t)$ is transmitted, and for simplicity in this case, it is assumed to arrive directly at the analog-to-digital converter of the receiver, resulting in the discrete signal $x(m)$. The received signal $x(m)$ is split into two paths where the sub-components $x_1(m)$ and $x_2(m)$ are generated by the product of two digital carriers that are generated within the receiver as shown in 5.2 and 5.3 and applying Trigonometric identities from Appendix A.2 and A.3.

$$
\begin{aligned}
x_1(m) &= y(m)cos(2\pi f_d m) \\
x_1(m) &= [m_1(m)cos(2\pi f_d m) + m_2(m)sin(2\pi f_d m)]cos(2\pi f_d m) \\
x_1(m) &= m1(m)cos^2(2\pi f_d m) + m_2(m)sin(2\pi f_d m)cos(2\pi f_d m) \\
x_1(m) &= m_1(m)\left[\frac{1}{2} + \frac{cos(4\pi f_d m)}{2}\right] + m_2(m)\left[\frac{sin(4\pi f_d m)}{2}\right]
\end{aligned}
\tag{5.2}
$$

$$
\begin{aligned}
x_2(m) &= y(m)sin(2\pi f_d m) \\
x_2(m) &= [m_1(m)cos(2\pi f_d m) + m_2(m)sin(2\pi f_d m)]sin(2\pi f_d m) \\
x_2(m) &= m_1(m)cos(2\pi f_d m)sin(2\pi f_d m) + m_2(m)sin^2(2\pi f_d m) \\
x_2(m) &= m_1(m)\left[\frac{sin(4\pi f_d m)}{2}\right] + m_2(m)\left[\frac{1}{2} - \frac{cos(4\pi f_d m)}{2}\right]
\end{aligned}
\tag{5.3}
$$

After mixing with two orthogonal carriers from the local oscillator in the receiver, as expressed in Equations 5.2 and 5.3, there emerge components with a frequency of $2f_d$. The Low Pass Digital Filter effectively eliminates all $sin(4\pi f_d m)$ and $cos(4\pi f_d m)$ components. Consequently, the resulting received signals $mr_1(m)$ and $mr_2(m)$ are described in Equation

5.4. It's important to note that the received digital components are a scaled version of $m_1(m)$ and $m_2(m)$ by a factor of $1/2$, and any necessary amplitude adjustment will be conducted during the equalization step.

$$mr_1(m) = 1/2(m_1(m))$$
$$mr_2(m) = 1/2(m_2(m))$$

(5.4)

One aspect to consider regarding the DUC is the digital nature of the carrier used, which necessitates accounting for the physical constraints of the hardware. The Digital-to-Analog Converter (DAC) has a maximum sampling rate, and the Light Emitting Diode (LED) utilized has a specific bandwidth. As a result of the DUC depicted in Figure 64b), the spectrum is a Double-Sideband Suppressed Carrier (DSB-SC). For the project outlined in this work, the employed LED has a bandwidth of 10 MHz, while the DAC has a maximum sampling rate of 100 MSps (Mega Samples per Second). Consequently, a digital carrier with a central frequency of $f_d = 5$ MHz and a signal bandwidth of 5 MHz was chosen, aligning with the 5G NR (New Radio) standard. The resulting signal will occupy the frequency range from 2.5 MHz to 7.5 MHz, as indicated in Figure 65. In this scenario, the LED frequency bandwidth does not impose any filtering.
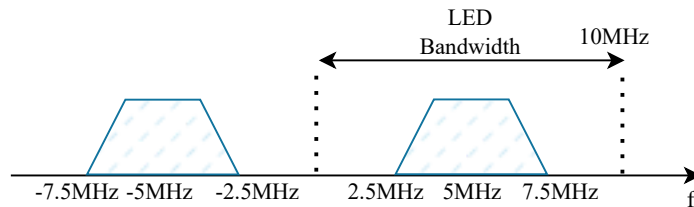
Figure 65 – Spectrum of the modulated using digital up-converter. The maximum frequency is inside the LED bandwidth and the LED doesn't require filtering.

Figure 66 shows the Low Level Design of the project. On the left side, the formation of the transmission Resource Grid is evident through the insertion of the Synchronization Signal Block (SSB), which includes essential components such as the Primary Synchronization Signal (PSS), Secondary Synchronization Signal (SSS), and Physical Broadcast Channel (PBCH). Notably, a specific codeword has been included in the PBCH mapping solely for testing purposes. Conversely, the Downlink Control Information (DCI) contains crucial information necessary for detection within the User Equipment (UE), as outlined in section 4.3.3.2. Subsequently, the discussion proceeds to introduce the Transport Blocks, which represent sets of bits designated for encoding within the DL-SCH.

The PBCH codeword, DCI, and the transport blocks were modulated and mapped to each channel: PBCH, PDCCH, and PDSCH, respectively. It's essential to highlight that PBCCH and PDCCH maintain a fixed modulation in QPSK, whereas PDSCH will exhibit

variable modulation and coderate, as discussed in Table 5. Once appropriately modulated and mapped, the Resource Grid is obtained, as previously discussed in detail in Figure 42. After the Resource Grid mapping, OFDM multiplexing is applied, followed by the insertion of the cyclic prefix (CP). It's noteworthy that Table 2 suggests the utilization of 25 Resource Blocks or 300 subcarriers for SCS = 15 kHZ and Bw = 5 MHz. To ensure efficiency in the IFFT algorithm, employing a multiplexing with the next power of 2, namely an IFFT of 512 points, is recommended.

According to [60], the baseband sampling rate for the 5G NR OFDM signal can be observed through Equation 5.5. This results in a baseband sampling rate of 7.68 MSps, as depicted in Figure 66, part a1), where the signal in baseband displays a typical OFDM spectrum. It's important to note that utilizing this signal would lead to substantial attenuation in lower frequencies due to the VLC channel response, as shown in Figure 63, part b). As discussed to obtain a signal of real components in digital passband, it is necessary to apply a Digital Up-Converter. However, before modulating through the digital carrier, it's crucial to upsample the baseband signal to achieve the same sampling rate used in digital carrier f_d. Figure 66, part a2), presents the upsampled signal with a FIR filter applied, resulting in a new sampling rate of $Fs2 = 75$ MSps, precisely matching the sampling rate supported by the ADALM 2000's DAC.

$$Fs_{baseband} = N_{FFT} \times SCS = 512 \times 15e3 = 7.68 \,\text{MSps} \tag{5.5}$$

Following the upsampling, the Digital up-converter is applied, wherein the real part is modulated by a cosine digital carrier, and the imaginary part by a sine digital carrier. Figure 66, part a3), demonstrates the band shifting result. The signal has been shifted to the central frequency of 5 MHz, with the maximum signal frequency obtained at 7.25 MHz. At this point, it's notable that the 75 MSps sampling rate used is approximately 10 times higher than the maximum frequency of the signal represented in Figure 66, part a3), which is a good practice in digital signal processing.

With the OFDM signal comprising real coefficients and band-shifted, it undergoes amplification, is subjected to a DC level addition to eliminate its negative component, and is then transmitted to the LED. The LED illuminates the Photodetector's reception area, and the photodetector's electrical signal is amplified by a transimpedance amplifier. As discussed in section 5.1.1, the DAC and ADC have different sampling rates. In this case, the signal obtained through the ADC sampling has a sampling rate of 100 MSps. Consequently, resampling along with a FIR filter is applied to match the same sampling rate as when the signal was band-shifted in Figure 66, part a3). Figure 66, part b3), demonstrates the received signal still in the passband. The Digital down-converter is applied to retrieve the complex signal in baseband. It can be observed in Figure 66, part b2), that the signal is now in baseband, howeever it is upsampled. Finally, downsampling

is performed to obtain the signal at the same baseband sampling rate of 7.68 MSps, as illustrated in Figure 66, part b1).

Subsequently, the Time Sync is applied to identify the Frame's start by correlating with the PSS. As discussed in section 4.3.3.1.1, there exist three N_{ID}^2 values depending on the cell id, thus testing is conducted for the three potential PSS, identifying the highest correlation peak among the three PSSs to acquire N_{ID}^2. Following this, frequency synchronization is executed through Pearson correlation with the reference PSS, obtaining the deviation between the oscillators of the gNB's and UE's ADALM 2000. At this stage, the received OFDM signal is already synchronized, necessitating only the removal of the cyclic prefix and execution of the OFDM demodulation by FFT.

Upon demodulating the signal, the received Transmission Resource Grid is acquired. The PDCCH-DMRS aids in the equalization of the PDCCH channel, enabling the decoding of the PDCCH bits, resulting in rxDCI. Subsequently, it becomes possible to obtain the modulation order and coderate through the MCS field. Finally, the PDSCH-DMRS symbols are utilized for the estimation and equalization of the PDSCH channel. With the received MCS, it becomes feasible to demodulate the PDSCH symbols and retrieve the transport block post LDPC decode.

5.2 Radio Frequency Transmission/Reception

Unlike the Downlink, which comprises several components, the Uplink is notably simpler. Essentially, the Uplink consists primarily of the ADALM PLUTO. Internally, the ADALM PLUTO already incorporates all the necessary components for transmission, including the IQ ZIF modulator illustrated in Figure 73 and the internal RF Amplifier.

5.2.1 ADALM PLUTO

In Figure 67, two subsystems are observed: the reception and transmission subsystems. The reception subsystem includes an LNA (Low Noise Amplifier) to amplify low-amplitude received signals. The Mixer performs the reverse shift from the passband to the baseband, while the filter bank removes components that generate aliasing during the demodulation process. The high-speed analog-to-digital converter digitizes the received signal for delivery to the processing device. Decimator filters perform downsampling, and finally, a non-recursive FIR (Finite Impulse Response) filter of order 128 is employed to generate the 12-bit output signal. The resulting signal, with its in-phase and quadrature (I/Q) components, is then directed to the baseband processor, the Xilinx SoC (System On Chip) [120].

The transmitter in Figure 67 accepts I/Q signals from the processor; an FIR filter ensures that the baseband signal remains within the bandwidth limits. Subsequently, the
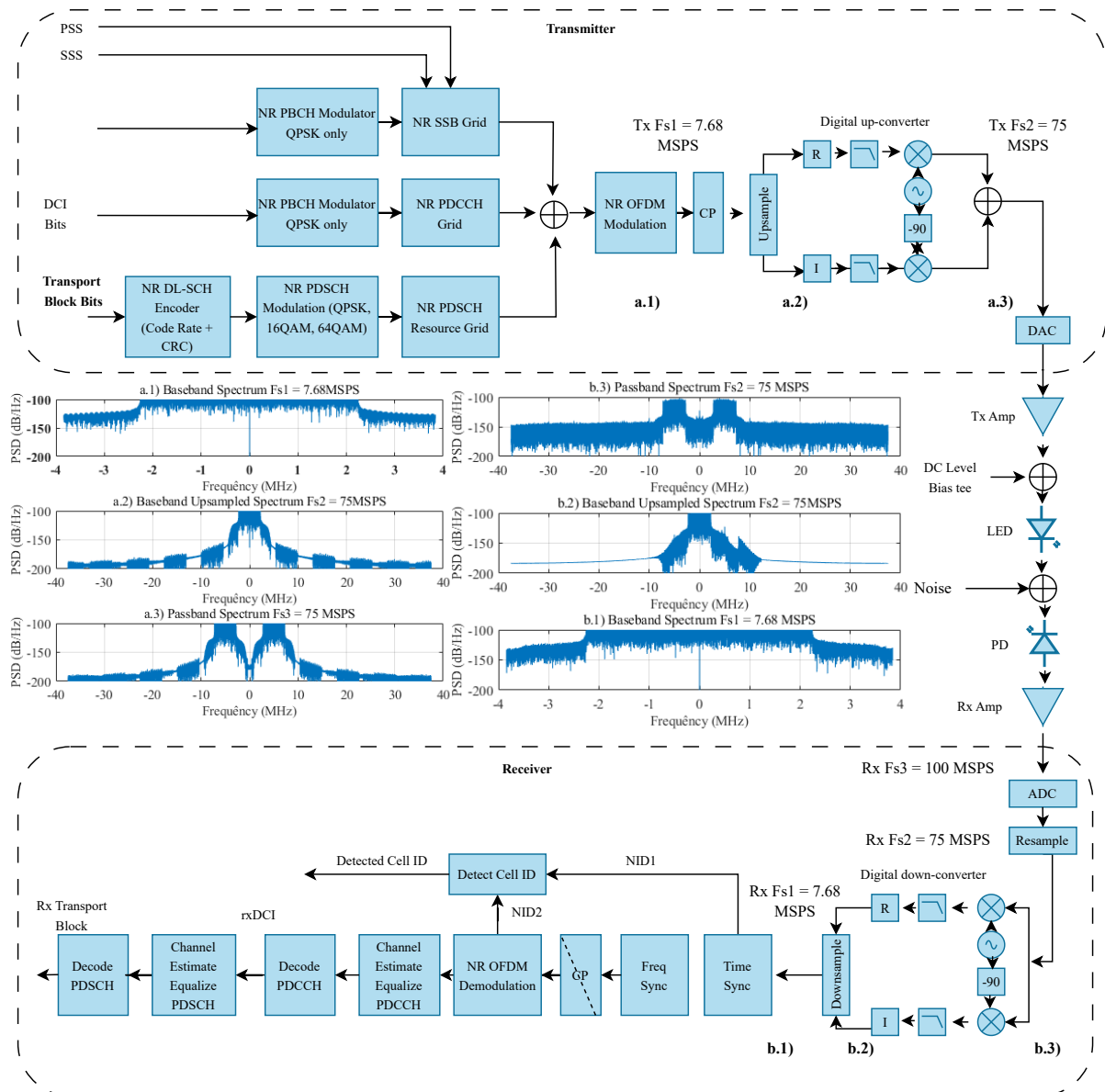
Figure 66 – The Low Level Design architecture of transmission utilizing the VLC channel is depicted as follows: a1) Displays the Downlink OFDM signal in baseband with Fs1 = 7.68 MSps. a2) The signal remains in baseband but has been resampled to a DAC rate of 75MSps. a3) The signal, resampled to 75MSps, has been shifted to a digital carrier with a central frequency of 5 MHz. b3) Illustrates the signal received by the UE's ADALM 2000, sampled at 100 MSps and resampled to 75 MSps. b2) The received signal has been demodulated, recovering the baseband signal; however, at this point, the baseband signal is upsampled. b1) The signal has been resampled to the baseband sampling rate of 7.68 MSps, enabling further processing by the receiver.

filter performs digital interpolation, and then, a high-speed digital-to-analog converter transforms the interpolated signal into an analog one. In the analog section, a filter removes potential additional harmonic components resulting from digital transformations; the mixer performs the modulation process with a shift in the passband after selecting a carrier. Finally, a small power amplifier is used before delivering the analog signal to the SMA
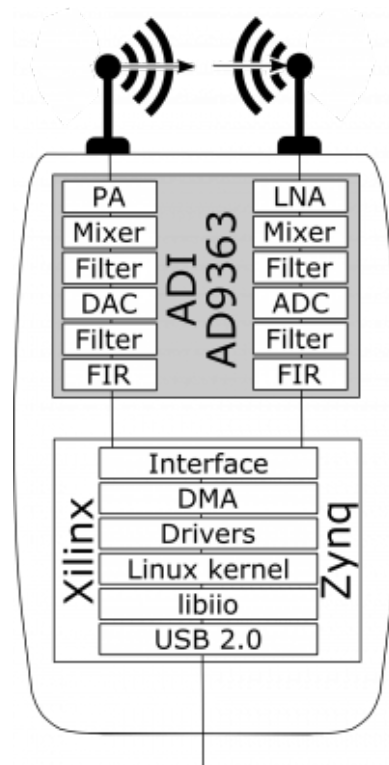
Figure 67 – The internal block diagram of Analog Devices' SDR ADALM PLUTO clearly depicts two distinct subsystems: the signal transmitter and the signal receiver.

output.

The Xilinx SoC interface is common to both the transmitter and receiver. It comprises digital ports, hardware with direct memory access (without involving clock cycles), various Linux system interface drivers, a libiio library with diverse functionalities for manipulation in Linux, and a USB interface [120]. The components of the Xilinx-Zynq layer establish the connection between the computer running programming language code and the ADALM PLUTO SDR device.

The ADALM Pluto also utilizes the structure of libiio as depicted in Figure 51 [112]. Furthermore, MathWorks has developed an API with a set of functions in MATLAB [121] that streamline the data transfer process using libiio. After the generation of 5G NR signals, these signals are handed over to the MATLAB API. Subsequently, this API communicates with the libiio driver on the Windows computer, which, in turn, communicates with the driver IIOD illustrated in Figure 51. Ultimately, this connects to the internal libiio, interfacing with the Linux kernel, and thereby transmitting the signals to the DAC and Antenna. Figure 68 illustrates the architecture at a lower level of the AD9361 chip used by the ADALM PLUTO. Note that there are two well-defined major blocks for Transmission and Reception.

In Transmission, observe that the digital signals from Ch1 I/Q and Ch2 I/Q are separated at the entrance of the Tx Channel. The real part follows the I path, and the
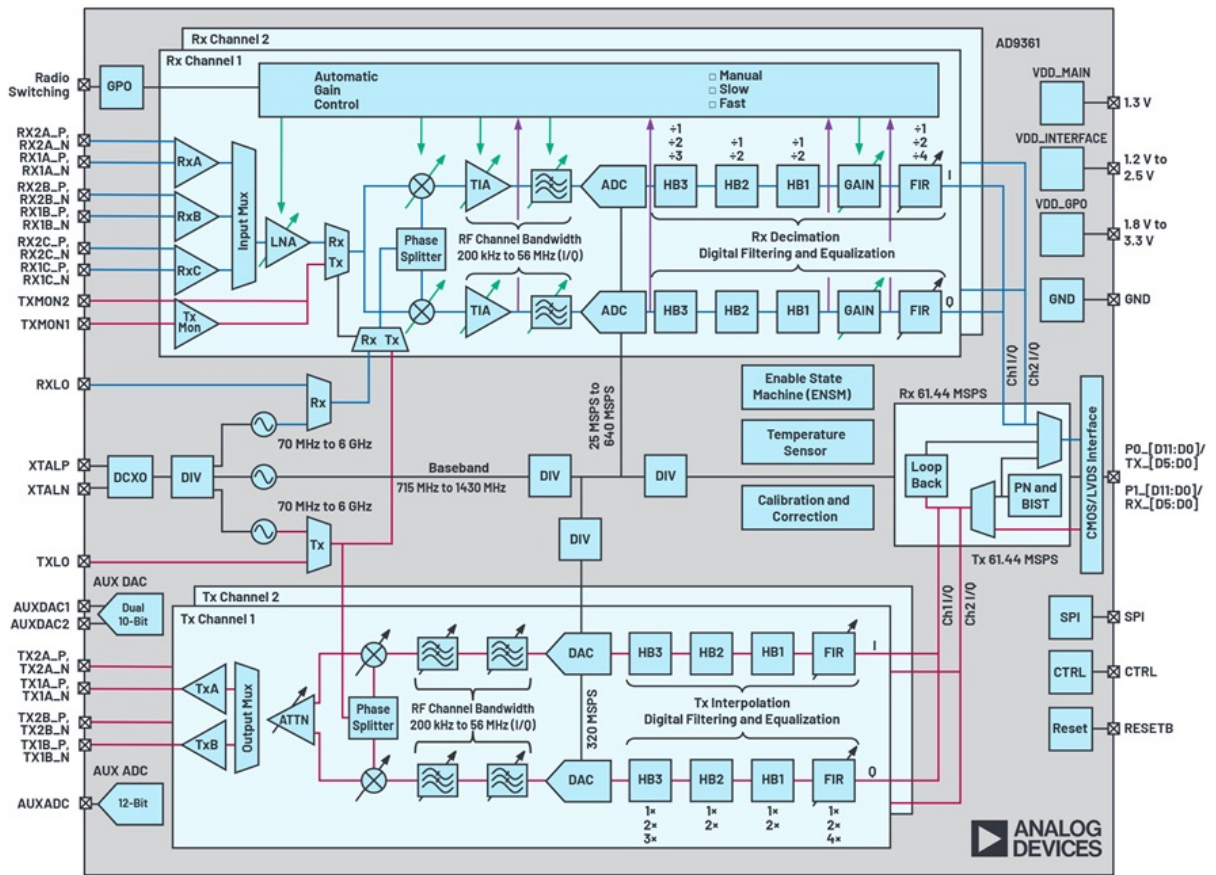
Figure 68 – ADALM PLUTO Low Level Overview

imaginary part follows the Q path (In-phase and Quadrature, respectively). Note that both the real and imaginary parts pass through a sequence of filters: FIR, HB1, HB2, HB3 before being directed to the DAC. The only programmable filter within the architecture is the poly-phase FIR filter, which is capable of performing interpolation and filtering functions [122], as depicted in Figure 68. In contrast, the remaining filters, namely HB1, HB2, and HB3, exclusively serve as interpolators with interpolation rates set at [1,2], [1,2], [1,2,3] respectively. For the design of the FIR Filter in the TX Channel, the approach involved utilizing the proposal for the LTE Filter with $B_w = 5$ MHz provided by Analog Devices, as outlined in [123]. This design process was executed using the AD9361 Filter Design tool implemented in MATLAB [124].

Table 7 delineates specific parameters: F_{pass} represents the maximum frequency within the passband, F_{stop} signifies the endpoint frequency of the transition band. A_{pass} denotes the allowable variation in the passband, while A_{stop} indicates the attenuation in the rejection band. Figure 69 provides a graphical representation illustrating the parameters detailed in Table 7 [123].

An important consideration is the sampling rate alignment with the characteristics of the ADALM-PLUTO. Referencing Figure 68, there's a PLL (Phase Locked Loop) bus responsible for generating the operating clock for both the ADC and DAC. It's evident

Filter specification	
Bandwidth Specification	5 MHz
Bandwidth Occupied	4.5 MHz
Baseband Sample Rate	7.68 MSps
F_{pass}	2.25 MHz
F_{stop}	2.75 MHz
A_{pass}	0.1 dB
A_{stop}	80 dB

Table 7 – FIR Digital Filter used in Tx/Rx Channel specification
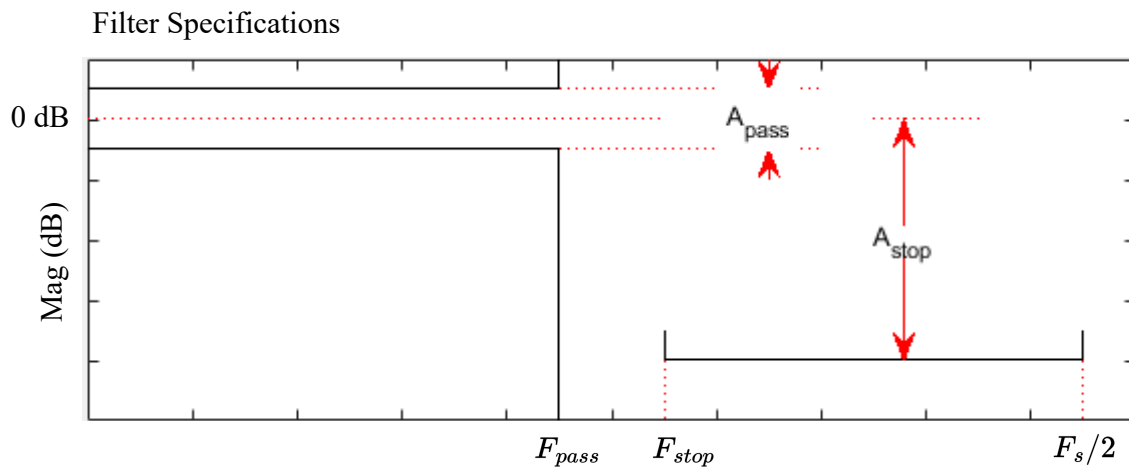
Figure 69 – FIR Digital Filter used in Tx/Rx Channel specification. Illustrative view of parameters indicated in Table 7

from the figure that the PLL can assume frequencies within the range [715-1430] MHz. However, it's noteworthy that while the DAC can operate at a maximum sampling rate of 320 MSps, the ADC's range is limited to [25-640] MSps. Clock divider circuits within the PLL can generate divided clock frequencies of [1,2,4,8,16,32,64].

The Figure 70 illustrates the utilization of the AD9361 Filter Wizard for the 5MHz LTE Filter for both the Tx and Rx Channels. Notably, in the AD936x Interpolation Rate section, the designed FIR filter have a 2x upsampling, resulting in a new sampling rate of 15.36 MSps. This upsampled signal is windowed by the FIR Filter as shown in the Figure 70. The HB1, HB2, and HB3 filters interpolated the signal by a factor of 2 as well. Consequently, the final sampling rate reached $F_{sfinal} = 122.88$ MSps.

Furthermore, it's observed that the PLL Clock Divider, Div, is set at 8. Hence, the DAC's PLL clock must be $122.88 \times 8 = 983.04$MHz, this clock rate is in the PLL's operational limit of [715-1430] MHz. Additionally, this final DAC sampling rate complies with the hardware limitation of a maximum of 320 MSps.

After the DAC stage, the analog section in Figure 68 becomes prominent. Note the presence of analog filters designed to shape the signals within the established operating
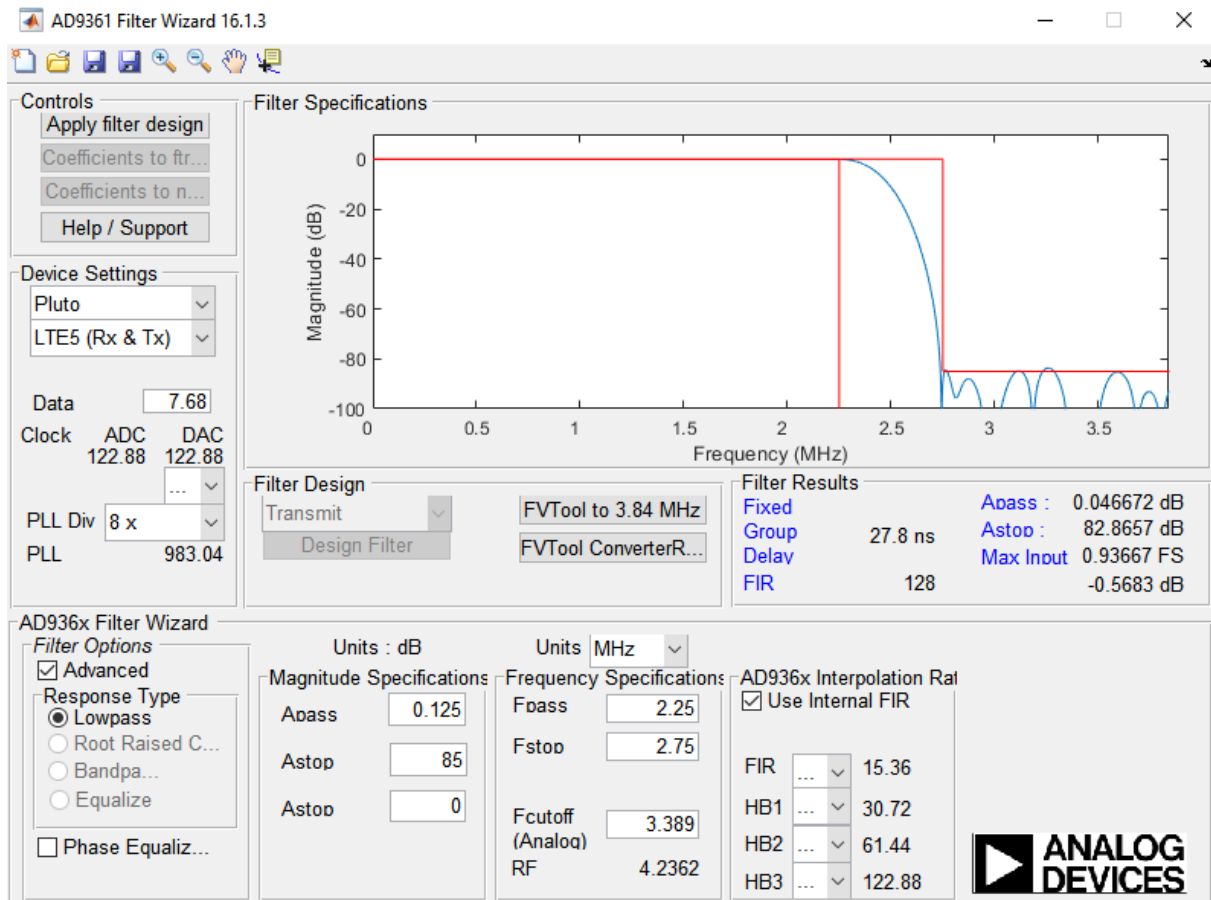
Figure 70 – The AD9361 Filter Design Tool orchestrates signal processing steps crucial for optimizing signal integrity. Primarily, the FIR Polyphase interpolation filter significantly enhances the baseband signal, increasing its sampling rate from 7.68 MSps to 15.36 MSps, while effectively applying a filter response with a passband frequency set at $F_{pass} = 2.25$MHz. Additionally, the subsequent stages—HB1, HB2, and HB3—execute a dual-rate interpolation, resulting in a consolidated final sampling rate of $F_{sfinal} = 122.88$ MSps. Moreover, the PLL Div, operating at 8 times, successfully configures the original PLL Clock to 983 MHz, precisely within the requisite operational range of [715-1430] MHz, aligning perfectly with the PLL clock's operational criteria.

bandwidth of the device (200kHz to 56MHz). Subsequently, modulation occurs the ATTN module combines the modulated real and imaginary parts and applies a gain. It's crucial to exercise caution here; during loopback testing, attenuation is necessary to prevent potential damage to the receiving module. Finally the signal goes through the Antenna Port.

The Rx Channel closely resembles the Tx Channel. The received signal undergoes amplification by the Low Noise Amplifier (LNA) and subsequently passes through ZIF demodulation. The signal is then amplified within the ADALM PLUTO's operating range (200kHz to 56 MHz) using a transimpedance amplifier (TIA) specifically tuned for this frequency band. Following this, the ADC digitizes the received analog signal, which has
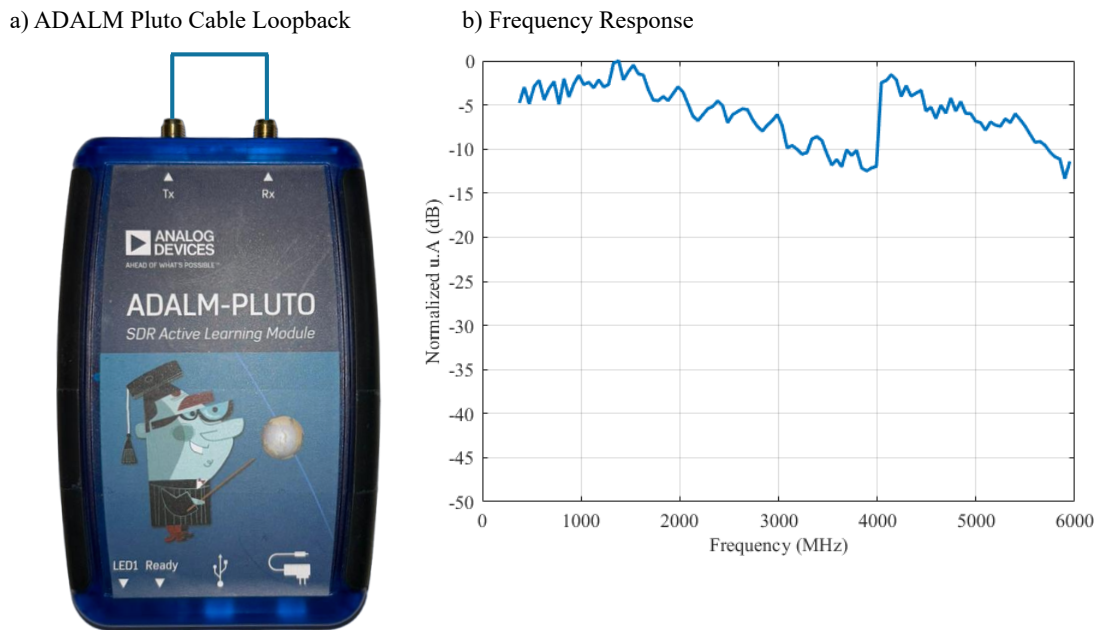
Figure 71 – a) Charecterization Loopback setup. b)Frequency Response

been filtered and amplified.

As depicted in Figure 70, both the ADC and DAC are tuned to operate at the same sampling rate. In this scenario, the ADC samples at 122.88 MSps and then decimates the signal down to its original baseband at 7.68 MSps. The received signal is subsequently returned to MATLAB via libiio for demultiplexing and decoding.

To characterize the ADALM Pluto, the setup depicted in Figure 71 is employed. An SMA cable links the TX and RX ports. To capture the frequency response, a process similar to that of the ADALM 2000 is utilized: tones are generated and used to span the entire spectrum. The amplitude of the received impulse after the Fast Fourier Transform (FFT) is recorded and normalized. The only difference is that a fixed 1MHz tone is used (due to the baseband analog filter operating from 200kHz to 56MHz), and 1MHz must be subtracted from the frequency used within the passband. This 1MHz tone traverses the complete passband, starting from 325MHz up to 6GHz. Additionally, note that the original ADALM Pluto operates up to 3.8 GHz; however, it's possible to extend its operational range up to 6GHz through customization, as discussed in [125].

In Figure 71 part. b), a peak in amplitude is noticeable at 1.4 GHz, followed by attenuation up to 3.8 GHz. Beyond 3.8 GHz, the hardware exhibits a different behavior, increasing the gain within this range before adopting an attenuation stance once more up to 6 GHz.

When characterizing the ADALM PLUTO using the antenna as depicted in Figure 72 part a), a different behavior is observed compared to the wired medium. The antenna model employed is the JCG401 by Jinchang Electron, featuring a 50Ω impedance, 2dBi
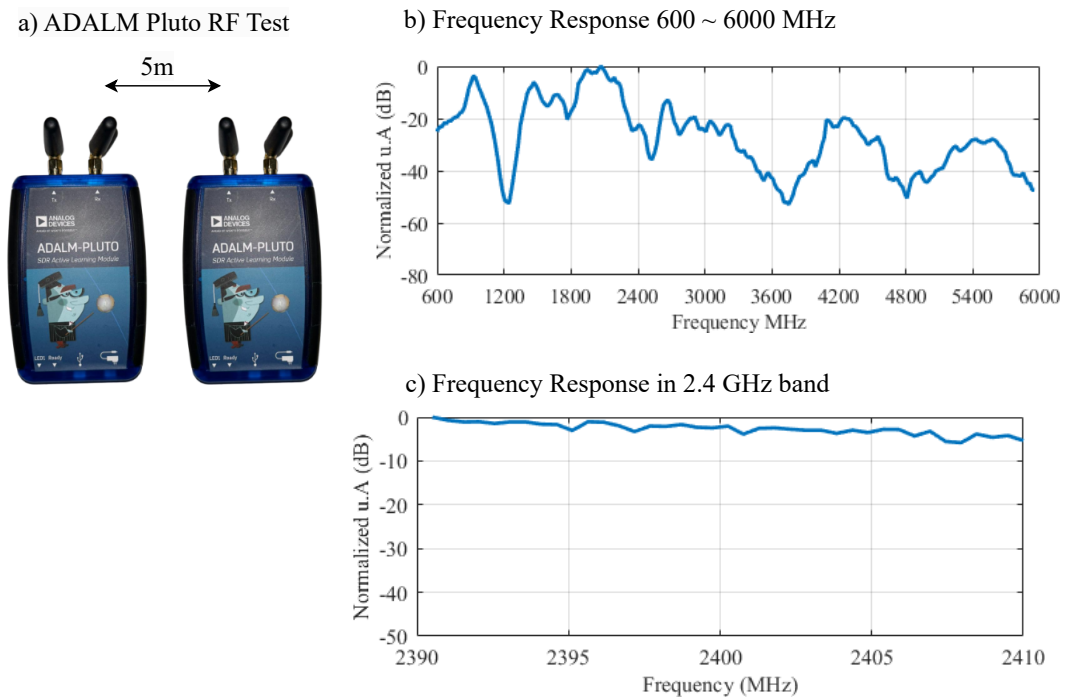
Figure 72 – a) Charecterization Loopback setup with JCG491 antennas . b) Full band Frequency Response c) Frequency response in operation band limits

gain, and an operational range of [824-894] MHz and [1710-2170] MHz [126]. To assess the RF link frequency response using the ADALM PLUTO and its respective antennas, two ADALM PLUTOS were employed, spaced 5 meters apart due to physical limitations of the USB cables that need to be connected to the computer. As recommended for such measurements, it is ideal to keep the antennas separated by at least 10 wavelengths [127] to avoid near-field interference [128]. Due to distance limitations, only the frequency response from 600 MHz was evaluated. The experimental results in Figure 72 part b) show a significantly broader operational range than specified in its documentation. A gain peak is observed in the range [720 - 900] MHz and in region between [1700-2200] MHz.

However, for this project, the frequency of 2.4 GHz was utilized due to its unlicensed status in Brazil. It's evident that this frequency experiences severe attenuation. Nevertheless, upon analyzing a narrower range within the exact channel frequency in Figure 72 part c), a response close to flatness is observed. This can be addressed in the received signal's equalization process.

5.2.2 Uplink Detailed Transmission Blocks

This section delves into a comprehensive exploration of the 5G signal transmission and reception model via the Radio Frequency channel.

Unlike the ADALM2000, the ADALM-PLUTO employs two internal paths to modulate the real and imaginary coefficients into two sinusoidal carriers, one cosine

and the other sine, respectively. Subsequently, the sum of these two orthogonal signals is transmitted to the antenna [118]. However, it's important to note that, in this configuration, two Digital-to-Analog converters (DACs) are required to modulate the baseband signal to passband. The Front-end modulator depicted in Figure 73.a) is recognized as a Zero-Intermediated Frequency (ZIF) modulator, as proposed, analyzed, and discussed in detail in [129]. Figure 73.b) illustrates the passband spectrum, featuring a positive component at f_c and a negative component at $-f_c$.

In Figure 73a) at the Transmitter, consider the real part of an M-QAM or M-PSK symbol at the input I, denoted by the discrete component $m_1(m)$, and the imaginary part at the input Q, denoted by $m_2(m)$. Both parts are converted to their continuous forms $m_1(t)$ and $m_2(t)$ respectively after passing through the two digital-to-analog converters. From there, the two components modulate two orthogonal carriers of the same frequency, giving rise to the two modulated signals $y_1(t)$ and $y_2(t)$ and them showed in Equation 5.6.

$$y_1(t) = m_1(t)cos(2\pi f_c t)$$
$$y_2(t) = m_2(t)sin(2\pi f_c t)$$

$$(5.6)$$
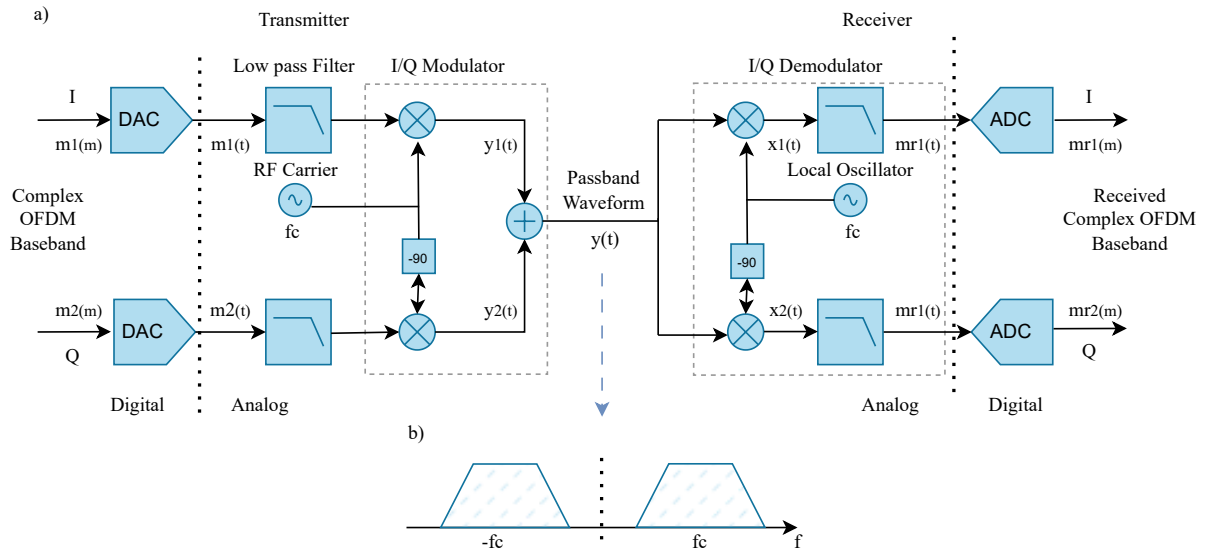
Figure 73 – a) ZIF architecture of the analog and digital divisions b) Spectrum with positive and negative components.

The baseband waveform is the summation of these two orthogonal components, where $y(t) = y_1(t) + y_2(t)$. In Figure 73a), the receiving part is also depicted. Note that the signal $y(t)$ is again split and then multiplied by waveforms generated from a local oscillator tuned to the same carrier frequency, resulting in two components $x_1(t)$ and $x_2(t)$.

As noted in the DUC strategy, the signal $y(t)$ at the receiver is mixed with two local carriers tuned to the frequency f_c. Similarly, the signals $x_1(t)$ and $x_2(t)$ can be obtained

by multiplying the received signal by the local carrier and expanding the identities from Appendix A.3 and A.4, resulting in Equations 5.7 and 5.8.

$$
\begin{aligned}
x_1(t) &= y(t)cos(2\pi f_c t) \\
x_1(t) &= [m_1(t)cos(2\pi f_c t) + m_2(t)sin(2\pi f_c t)]cos(2\pi f_c t) \\
x_1(t) &= m_1(t)cos^2(2\pi f_c t) + m_2(t)sin(2\pi f_c t)cos(2\pi f_c t) \\
x_1(t) &= m_1(t)\left[\frac{1}{2} + \frac{cos(4\pi f_c t)}{2}\right] + m_2(t)\left[\frac{sin(4\pi f_c t)}{2}\right]
\end{aligned}
\tag{5.7}
$$

$$
\begin{aligned}
x_2(t) &= y(t)sin(2\pi f_c t) \\
x_2(t) &= [m_1(t)cos(2\pi f_c t) + m_2(t)sin(2\pi f_c t)]sin(2\pi f_c t) \\
x_2(t) &= m_1(t)cos(2\pi f_c t)sin(2\pi f_c t) + m_2(t)sin^2(2\pi f_c t) \\
x_2(t) &= m_1(t)\left[\frac{sin(4\pi f_c t)}{2}\right] + m_2(t)\left[\frac{1}{2} - \frac{cos(4\pi f_c t)}{2}\right]
\end{aligned}
\tag{5.8}
$$

Equation 5.9 illustrates the recovered baseband signals $mr_1(t)$ and $mr_2(t)$, representing the In-phase and Quadrature components, respectively. Moreover, it is evident that $mr_1(t)$ and $mr_2(t)$ are directly proportional to $m_1(t)$ and $m_2(t)$ with a reduced amplitude by a factor of 1/2. In practical systems, signal attenuation due to the channel is also encountered, and the amplitude of the received signal is digitally adjusted in the equalization stage. Finally, the received digital component $mr_1(m)$ is obtained after analog-to-digital conversion in the ADC. Figure 73b) also illustrates the spectrum $Y(f)$ of the signal $y(t)$ generated during transmission. Note that a Double Side Band - Suppressed Carrier (DSB-SC) signal is observed.

$$
\begin{aligned}
mr_1(t) &= 1/2(m_1(t)) \\
mr_2(t) &= 1/2(m_2(t))
\end{aligned}
\tag{5.9}
$$

Depicted in Figure 74 as the Low Level Design of the project. The left side of the figure vividly illustrates the construction of the transmission Resource Grid, highlighting the pivotal role of the Sounding Reference Signal (SRS) in ensuring synchronization. Additionally, within the Uplink Control Information (UCI) lies crucial ACK/NACK data. This information prompts the gNodeB to request the retransmission of the last frame in the event of NACK reception see section 4.3.3.5. Subsequent to this, the discussion progresses to introduce the concept of Transport Blocks, serving as designated sets of bits earmarked for encoding within the UL-SCH.

The DCI codeword and transport blocks undergo modulation and mapping onto specific channels: PUCCH for DCI and PUSCH for transport blocks. PUCCH maintains

a constant QPSK modulation, while PUSCH exhibits variable modulation and coderate, as outlined in Table 5. Once modulation and mapping are completed, the Resource Grid is generated. Subsequently, OFDM multiplexing is applied, followed by the insertion of the cyclic prefix (CP). Referencing section 4.3.3.2, it's noted that the Uplink employs the same modulation order and coderate as the received MCS in the downlink.

As detailed in section 5.1.7, the baseband sampling rate stands at 7.68 MSps for SCS = 15 kHz and Bw = 5 MHz. Figure 74 (part a.1) displays the baseband spectrum of the OFDM waveform with a sampling rate of 7.68 MSps. Following this, the application of a polyphase FIR filter with two times interpolation is shown, thereby increasing the sampling rate to 15.36 MSps. However, the FIR filter deals with spectrum copies by applying attenuation at 2.25 MHz, as seen in section 5.2.1.

Subsequently, three interpolators: HB1, HB2, and HB3 are applied, each doubling the sampling rate, resulting in a sampled signal at $F_s = 122.38$ MSps, as observed in Figure 74 part a.3). Finally, the performance of the ZIF modulator is assessed. At this stage, the signal becomes analog and holds a central frequency of $F_c = 2.4$ GHz according to 74 part a.4) . The analog signal then passes through an amplifier and is directed to the antenna for propagation into space.

The Radio Frequency signal emitted by the UE propagates to the gNB's receiving antenna. Upon reception, the signal is amplified by a Low Noise Amplifier, as depicted in Figure 74 part b.4), showcasing the received signal within the passband. Subsequently, the entire interpolation process carried out by the transmitter is reversed through the decimation process.

In Figure 74 part b.3), the demodulated signal is displayed after the ZIF. The signal shown in part b.3) maintains a sampling rate of $F_s = 122.38$ MSps, which corresponds to the interpolated signal. Following this, the decimation process is applied, as shown in Figure 74 part b.2), where the signal is recovered at $F_s = 15.36$ MSps. Subsequently, the designed FIR filter is implemented, returning the signal to its initial sampling rate of 7.68 MSps, as exhibited in Figure 74 part b.1).

Starting from signal 74 part b.1), the synchronization process in both time and frequency is initiated to prepare the signal for the demultiplexing and decoding of the received OFDM signal.

Upon completing the OFDM demultiplexing, the outcome is the received Resource Grid. From this Resource Grid, symbols are extracted for channel estimation and equalization of the PUCCH and PUSCH channels. Following this step, digital demodulation is performed for both PUCCH and PUSCH. Additionally, the PUSCH entails an extra complexity involving LDPC decoding of the received symbols.

It's important to note that unlike the Downlink, there's no necessity to decode the

PUCCH before the PUSCH in this scenario. Here, the modulation order and coderate are predetermined, as the gNodeB has previously transmitted this data in the MCS within the PDCCH. The UE assumes these values for the PUSCH accordingly and with this MCS the PUSCH decode is performed.

5.3   Combined VLC + RF Setup

The Figure 75 illustrates the assembly of the prototype used for 5G NR communication, employing Downlink via VLC and Uplink via RF. In addition to the components previously mentioned in this work, a DC source for unipolar voltage was used to generate the DC level carried to the Bias Tee. Additionally, a second set of two DC sources was employed to create a symmetrical source, providing power to the Photodiode board.

The ADALM 2000 devices communicate with a laptop running MATLAB software through USB ports. However, conventional laptops have limited USB ports. To address this limitation, the ADALM PLUTO devices were interconnected via a USB-Ethernet converter and connected to the same Ethernet network as the laptop.

Figure 76 illustrates the logical testing procedure. Initially, the Modulation Coding Scheme to be inserted into the Downlink Control Information (DCI) is defined, as shown in Table 5 and detailed in section 4.3.3.2. At this stage, all repetition loop counters are reset.

The initial Downlink begins with the DCI New Data field set to True. A complete Resource Grid for the Downlink is initialized and then multiplexed using OFDM with numerology $\mu = 0$. This Downlink signal is transmitted from the gNB through the LED VLC channel and received at the UE via the photodetector.

At the User Equipment, the reception process involves reception, synchronization, equalization, and decoding of the Received Frame. Initially, the UE identifies the PDCCH, decodes the DCI, and retrieves the MCS, providing information about the modulation order, code rate, and whether it's new or repeated data.

With the modulation order and code rate, the UE performs LDPC decoding to recover the received bits. Errors in transmission are identified by checking the CRCs of each received Transport Block. "It's important to note that the algorithm depicted in Figure 76 isn't the official 5G NR data flow control algorithm. This control would typically be managed by the Hybrid Automatic Repeat Request (HARQ) mechanism [130], requiring several implementations within the MAC layer. Hence, for simplification purposes, the strategy adopted here involves evaluating error bits and requesting retransmissions via the UE's Uplink ACK/NACK.

The program iterates 10 times, and it's noteworthy that 9 slot-symbols were used
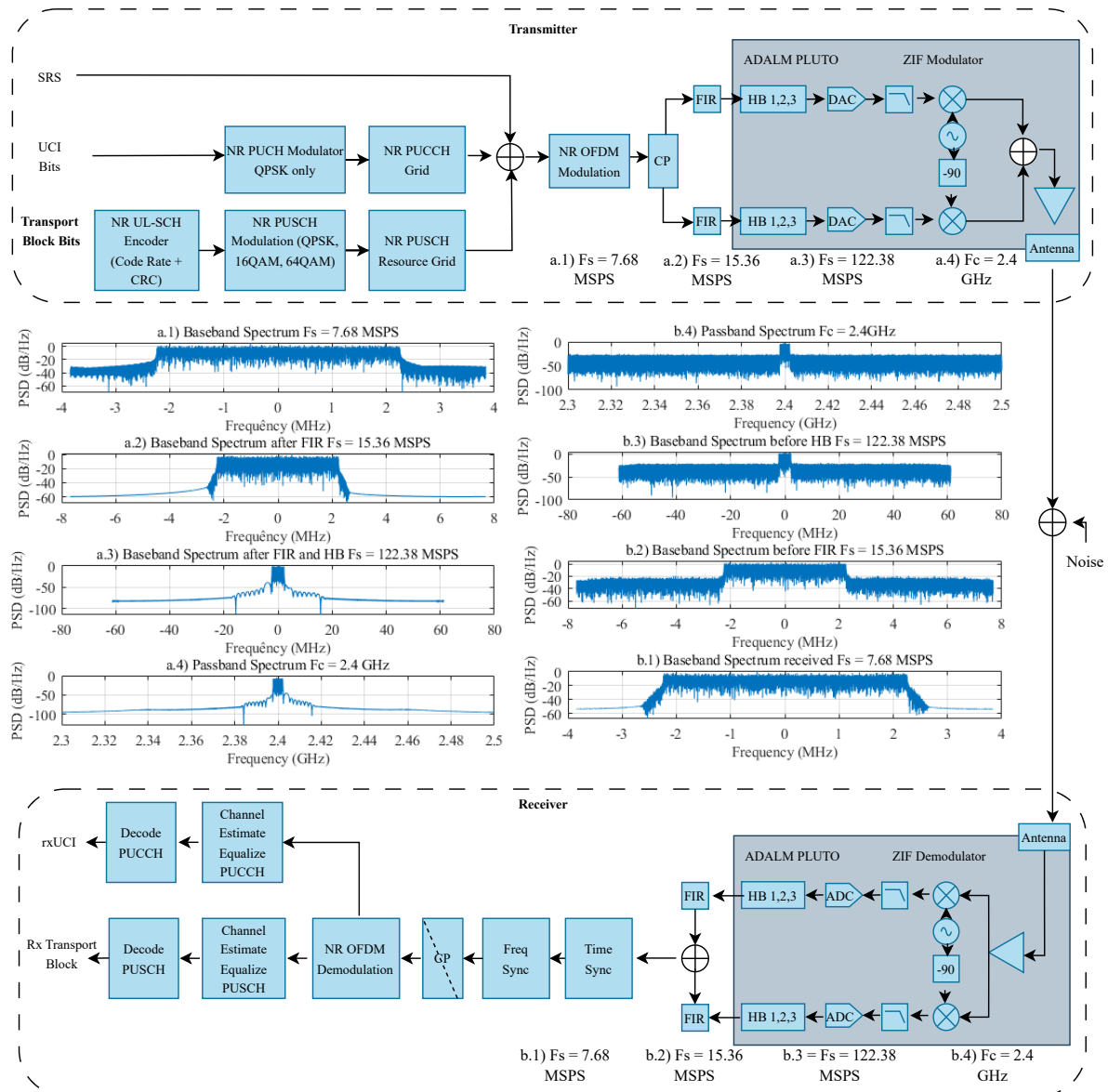
Figure 74 – The architecture for transmitting signals through the RF channel follows a sequential process: Initially, in a1) the Uplink OFDM signal is presented in baseband with a sampling rate Fs = 7.68 MSps. Following this, in a.2) the signal remains in the baseband but undergoes resampling to Fs = 15.36 MSps by the FIR polyphase filter. Subsequently, in a.3) the signal is further resampled to 122.36 MSps after passing through HB1, HB2, and HB3 interpolators. This resampled signal is then modulated by the ZIF Modulator in a.4) shifting it to Fc = 2.4 GHz. On the reception side, b.4) shows the signal received by the gNodeB in the passband. Moving to b.3) the received signal undergoes demodulation, reverting it back to the baseband. However, at this stage, the baseband signal is upsampled, operating at Fs = 122.36 MSps. Further in b.2) the signal is resampled back to the sampling rate of 15.36 MSps. Finally, in b.1) the FIR filter is applied, successfully recovering the signal at the initial sampling rate of Fs = 7.68 MSps.
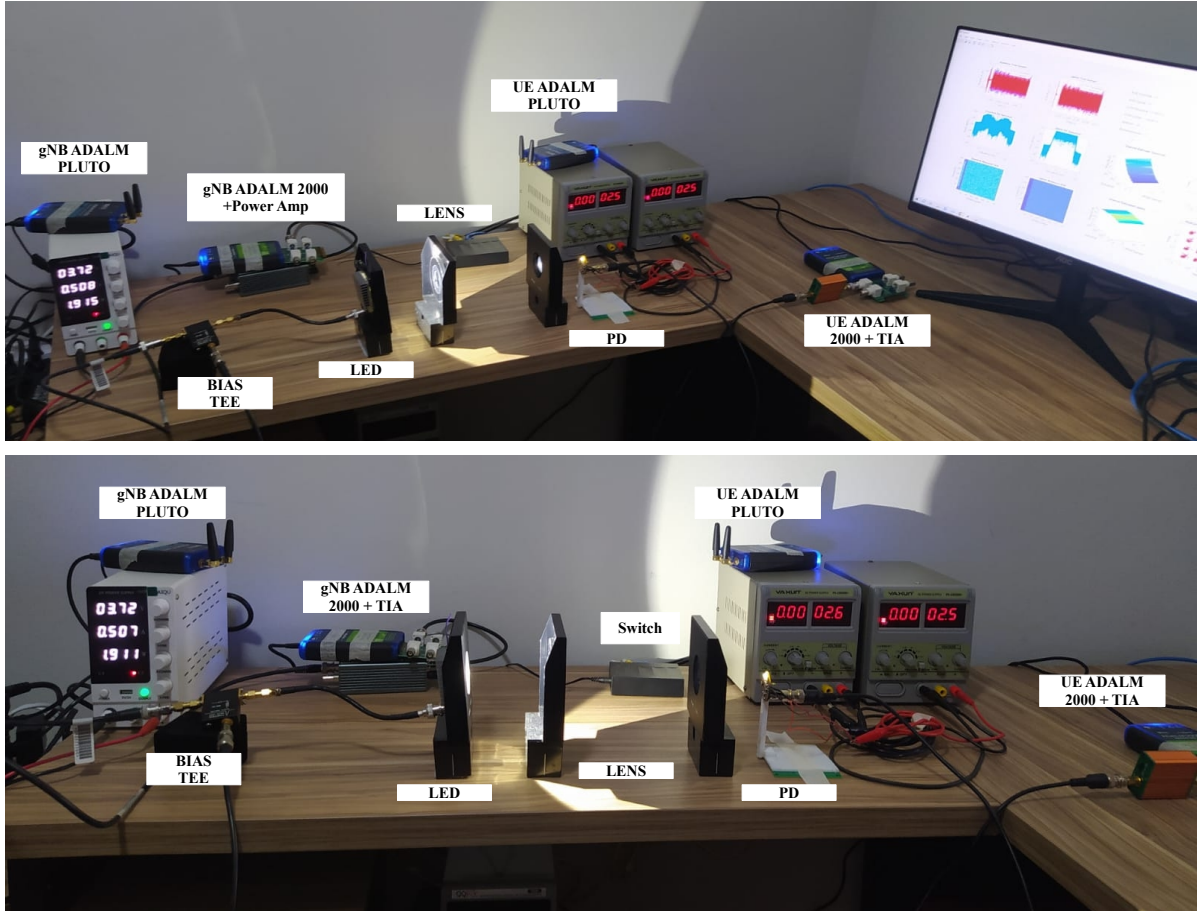
Figure 75 – Assembly of Combined VLC + RF Setup

for the PDSCH, as outlined in section 4.3.3.3. Therefore, these are the data considered for BER (Bit Error Rate) and EVM (Error Vector Magnitude) analysis. It's important to observe that 9 slot-symbols are dedicated to the PDSCH, resulting in a raw bit count calculated by Equation 5.10.

$$
\begin{aligned}
\text{total bits} &= log_2 Q_m N_{rep}[N_{symbols}^{slot} N_{subframes} N_{SC} - (L_{DMRS} N_{SC}^{DMRS})] \\
&= log_2 Q_m \times 10 \times [14 \times 9 \times 300 - 2(150)]
\end{aligned}
\tag{5.10}
$$

Where Q_m represents the modulation order, $N_{symbols}^{slot}$ denotes the fixed number of slot-symbols (set at 14). $N_{subframes}$ indicates the number dedicated to PUSCH/PDSCH. Additionally, N_{SC} stands for the number of subcarriers available when $\mu = 0$ and $B_w = 5$ MHz. $L_{DMRS} N_{SC}$ signifies the quantity of slot-symbols allocated to PDSCH/PUSCH DMRS, $\times N_{rep}$ is the number of repetitions in the experiment and N_{SC}^{DMRS} refers to the number of subcarriers allocated in the DMRS.

It's worth mentioning that Equation 5.10 and Table 8 shows the total amount of bits inserted into the Resource Grid. The effective payload bits depend on the size of the Transport Block Size according to the DL/UL-SCH (Downlink/Uplink Shared Channel) as shown in Figure 25. Table 8 presents the effective payload bits transmitted, considering

Transmitted bits	
QPSK	7.5e5
16QAM	1.5e6
64QAM	2.25e6

Table 8 – Total Bits send per modulation order

MCS	Modulation Order	Coderate	TBS (bits)	Total (bits)	BER max
1	QPSK	120/1024	848	7.6e4	2.5e-4
5	QPSK	602/1024	4224	3.8e5	1.2e-5
6	16QAM	378/1024	5248	4.72e5	1.5e-5
11	16QAM	658/1024	9224	8.3e5	2.7e-5
12	64QAM	466/1024	9736	8.7e5	2.9e-5
20	64QAM	873/1024	18432	1.65e6	0.5e-6

Table 9 – The Transport Block Size, Total Effective Payload Bits, and Maximum Bit Error Rate (BER) should be calculated with a 95% confidence level, taking into account LDPC encoding, code rate, modulation order, and the number of subcarriers occupied for DMRS.

the code rate, number of symbols dedicated to DMRS (Demodulation Reference Signal), modulation order, and TBS Size. Once calculated the TBS Size, the total effective bits amount to $TBS \times 9 \times 10$.

For BER calculations, it's a good practice to use a value around three times the desired BER level. For instance, to measure a BER of 10^{-3}, it would require 3×10^3 bits to measure this BER with 95% confidence [131]. In this case, refer to Table 9, which shows the maximum BER that can be confidently calculated for each test conducted. Consequently, some experiments might show a BER of 0. However, this doesn't necessarily mean the system is immune to errors. For instance, with MCS=1 employing QPSK modulation and a lower code rate, it would require a significantly large number of iterations, leading to extensive testing time to find transmissions errors.

In Section 4.3.3.7, an exploration into the derivation of the effective data rate is undertaken, which depends on the chosen code rate and modulation order, as elucidated by Equation 4.29. Table 9 presents six distinct Modulation and Coding Schemes (MCS), each resulting in varying data rates, succinctly consolidated in Table 10. Additionally, a comprehensive study highlighted in [132] offers invaluable insights into future bandwidth requirements. It underscores that the minimum throughput necessary for streaming HD video is approximately 5 Mbps, while for 4K video, it escalates to at least 15 Mbps. In light of this analysis, it's discernible that MCS options 6, 11, 12, and 20 suffice for HD video streaming, while MCS 20 alone meets the requisites for streaming 4K video content.

Conversely, simpler applications have been mapped in [132], such as those involving speech transmission, like Podcasts. In these cases, only 0.5 Mbps would already meet

MCS	Modulation Order	Coderate	Datarate (Mbps)
1	QPSK	120/1024	0.9
5	QPSK	602/1024	4.54
6	16QAM	378/1024	5.7
11	16QAM	658/1024	9.92
12	64QAM	466/1024	10.54
20	64QAM	873/1024	19.74

Table 10 – Effective Datarate taking in account coderate and modulation order for all tested scenarios.

Parameter	Decription	Value
μ	Numerology	0
SCS	Subcarrier Spacing	15kHz
B_w	Bandiwdth	5 MHz
B_weff	Bandiwdth Effective	4.5MHz
T_s	OFDM symbol duration	66.67ms
CP_L	Cyclic Prefix Length	4.69ms
MCS	Modulation Coding Scheme	[1,5,6,11,12,20]
Q_m	Modulation Order	[QPSK, 16QAM, 64QAM]
R	Coderate	[120, 602, 378, 658, 466, 873]/1024
L_{LOS}	VLC Link LOS Legnth	[20, 30, 40, 50,..., 250] cm
I_{DC}	DC Current Bias Point	[250, 500, 750, 1000, 1250, 1500] mA
F_c^{DUC}	DUC Central Frequency	5 MHz
F_c^{RF}	Central Frequency of RF Carrier	2.4 GHz

Table 11 – Summary of Parameters Utilized in the Practical Experiment.

the requirement; thus, all MCSs from Table 10 would suffice. For online gaming, the requirement would start from 5 Mbps, hence fulfilled starting from MCS 6.

Studies presented in [133] and [134] outline throughput requirements for devices in a smart home, such as smart speakers, smart plugs, smart thermostats, and other sensors. Only 0.5 Mbps would be necessary in these cases, while residential security cameras in SD would require just 2 Mbps. This clearly demonstrates the feasibility of sharing part of the connection demand with VLC medium and the rates achieved in a device like the one proposed in this work.

The algorithm depicted in Figure 76 outlines the logical part of the experiment. However, various other physical parameters were also considered and varied, such as the VLC link size, which ranged from [20cm, 30cm, 40cm,...250cm], and the DC current bias spanning [250mA, 500mA,...,1500mA]. Table 11 summarizes all the parameters used in the experiment.
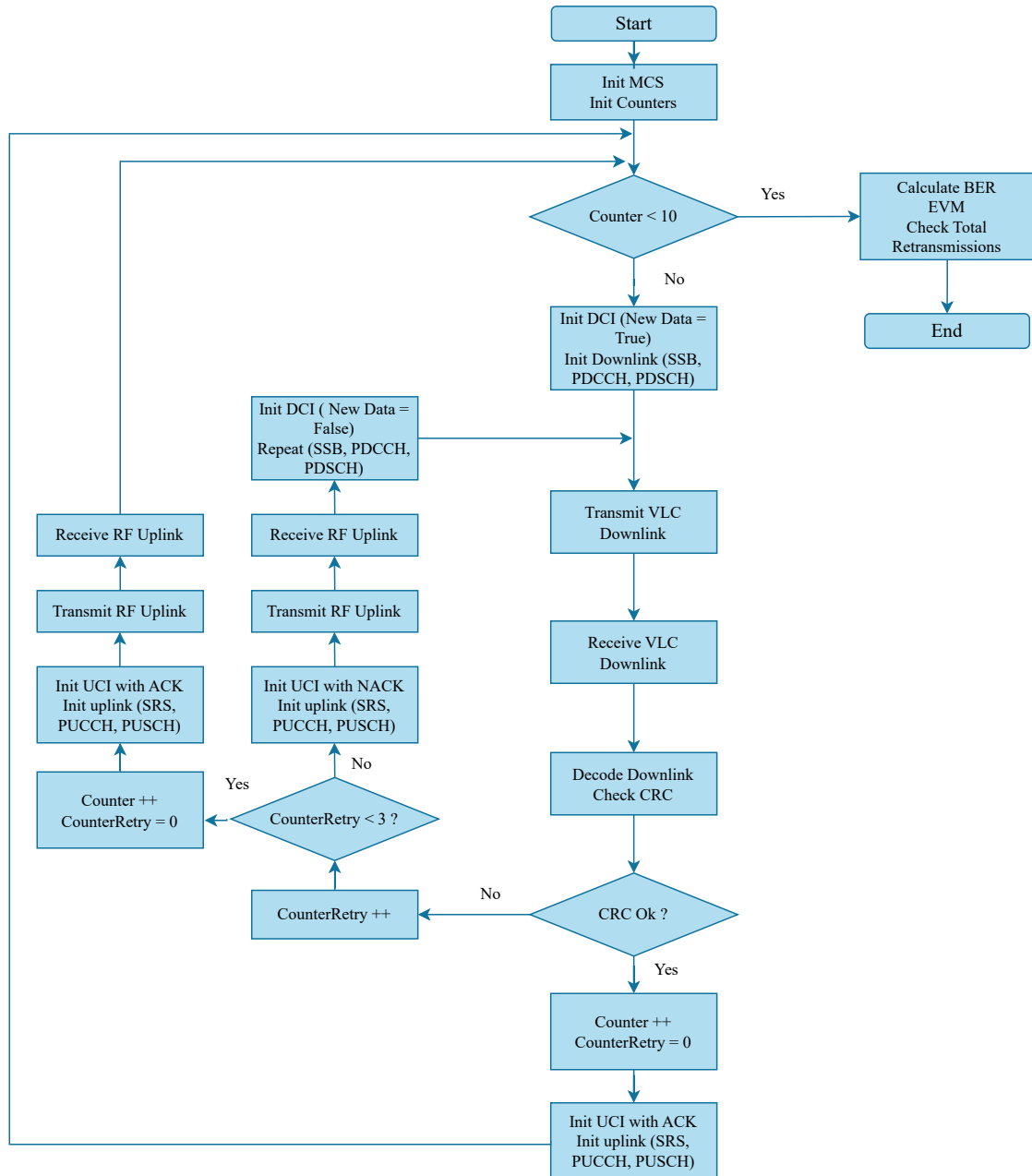
Figure 76 – Algorithm executing the logical test of the prototype. Essentially, the downlink is transmitted from the gNB to the UE. The UE processes the data and sends an ACK or NACK depending on whether there's an error in reception. If the UE receives three error-laden packets consecutively, it abandons requesting retransmission from the gNB and moves to the next frame scheduled for reception. Upon completing the transmission of 10 frames, the algorithm concludes, evaluating BER, EVM, and the total number of retransmissions

5.4 Setup Limitations

As discussed in the sections on physical channels 4.3.3, only the PDSCH and PUSCH channels employ data encoding for transmission, utilizing LDPC encoding as discussed in 4.3.2.1. However, for the other physical channels: PBCH, PDCCH, and PUCCH bits are left uncoded as a simplification, as implementing a different coding technique for these channels would be necessary. Instead, these bits are repeated until they occupy all available OFDM symbols in the Slot-symbol of the Resource Grid.

Due to bandwidth limitations of the LED, only the 5G NR signal of Bw = 5 MHz was evaluated. Considering the effective bandwidth $B_{\text{eff}} = 4.5$ MHz, it has been shifted to the central frequency $F_c = 5$ MHz, reaching the limits of [2.25,7.25]MHz. As discussed in section 4.3.3.1.3, the PBCH requires 240 fixed subcarriers. Therefore, only with a subcarrier spacing of SCS = 15 kHz would there be sufficient Resource Elements for the PBCH. For other numerologies, this wouldn't be feasible, hence the study was confined to SCS = 15 kHz and Bw = 5 MHz.

In Appendix B, Table 12 displays all the Modulation Coding Schemes outlined in the 5G NR specification. However, conducting tests with all of them would be time-consuming. Therefore, only MCS = [1, 5, 6, 11, 12, 20] were utilized. These selections represent, for each modulation order $Q_m = $ [QPSK, 16QAM, 64QAM], both strong and weak coderates for each modulation order.

Due to the available cable lengths, particularly for the USB connection, the maximum size of the VLC link to be evaluated had to be limited to 250cm. However, experiments were conducted ranging from 20cm up to 250cm, with increments of 10cm between each iteration. The bias current varied in increments of 250mA, starting from 250mA and reaching up to 1500mA. Increasing the current beyond this point could potentially damage the Bias Tee and thus was restricted to this value. Nonetheless, it was sufficient to assess the non-linear behavior of the employed LED.

Conversely, for the Uplink transmission, no specific metric was established to vary the distance between devices. This omission stemmed from the primary research focus on adapting visible light communication, compounded by time constraints. Similarly, in the algorithm depicted in Figure 76, there's no provision for an ACK/NACK signal from the Downlink confirming the correct reception of the Uplink. This aspect was simplified, with the Uplink operating as a transmission echo, indicating the message was correctly received at the UE. However, it's worth noting that this area remains a potential area for evaluation in future research endeavors.

6 Experimental Results and Discussions

The experiments were conducted following the sequence of operations outlined in the algorithm in Figure 76, while varying the parameters from Table 11. The initial result showcased is the consolidated EVM for the QPSK constellation, varying the distance between the LED and Photodetector, direct current polarization, and coderate, as detailed in Figure 77. It is observed that the shortest distances, between 20 to 40 cm, yielded the poorest performance in terms of EVM. This primarily occurred due to Photodetector saturation. The extremely close proximity between luminous power and the Photodetector caused a non-linear saturation effect, impairing symbol detection. As the link distance increased beyond 50 cm, the EVM tended to stabilize around approximately 4.9%. However, another non-linear factor emerged: LED saturation. Even after 50 cm, with a 1500mA current polarization, there was noticeably inferior performance around 5.2%. This is due to the non-linearity induced by the high LED current, as previously demonstrated in Figure 59. Moreover, with a 1250mA current, the behavior during optical link length variation ranked as the second poorest, stabilizing around 5.1%. Furthermore, as depicted in Figure 77, it's evident that lower currents, especially at 250mA, exhibited the best outcomes. This is attributed to this polarization exploring a more linear operating range of the LED and causing minimal photodetector saturation. The constellations are displayed for a distance of 20cm, with a 1500mA polarization current and a coderate of 602/1024 (worst case), and for the distance of 50cm, with a 250mA current and coderate 120/1024 (best case). In both constellations, a well-distributed and concentrated set of symbols is visible, without apparent deviations that would hinder the decision regarding the received symbol.

Similarly, Figure 78 depicts the EVM performance curve against distance for 16QAM constellation. It is noticeable in this scenario that the same saturation effect occurs at a distance of 20cm, followed by EVM stabilization after 50cm. Additionally, the saturation effect of the LED indicates its detrimental impact in the case of 16QAM as well. The best results are observed at 250mA. The EVM values remain practically the same concerning distance compared to QPSK. In this case, it's apparent that the constellation does not significantly influence EVM performance. The constellation diagrams for the worst-case scenarios at 20 cm and 50 cm were considered, as shown in Figure 78. Unlike QPSK, which exhibits a well-separated constellation, this is only the case for 16QAM with the constellation at 50 cm, using a 250 mA polarization current and a coderate of 658/1024. It can be verified that, in this scenario, with an EVM of 4.7%, the constellation points become well-separated. However, for the worst-case scenario at a distance of 20 cm, 1500 mA, and a coderate of 378/1024, the constellation shows symbols bordering the decision zone. In this instance, direct detection without encoding methods would result in
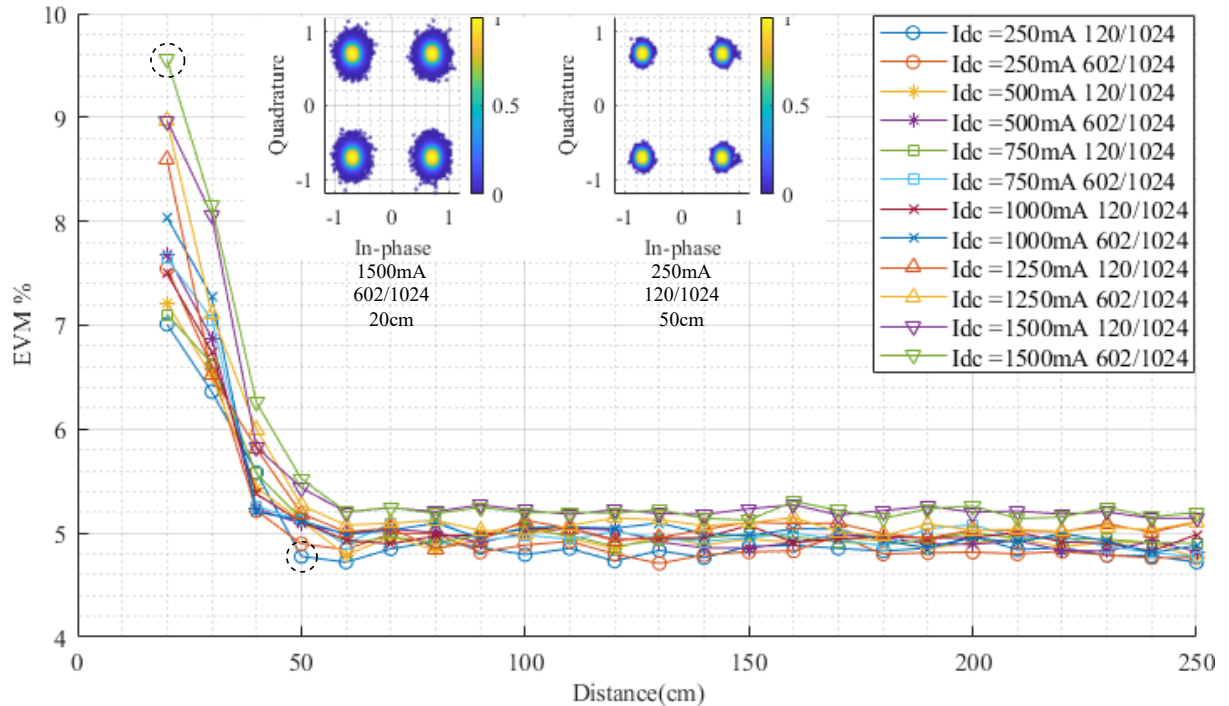
Figure 77 – The study evaluated EVM performance across various distances and polarization currents using QPSK modulation. At 20cm with I_{DC} = 1500 mA and a coderate of 602/1024, the constellation diagram showed an EVM of 9.5%. Similarly, at 50cm with I_{DC} = 250 mA and a coderate of 120/1024, the EVM was 4.7%. Both constellation diagrams exhibited well-distributed symbol patterns.

error detections.

The analysis of EVM performance against distance for the 64QAM case, as shown in Figure 79, concludes that similar saturation effects observed in QPSK and 16QAM cases are noted for the photodetector at 20cm and LED at currents of 1250mA and 1500mA, resulting in poor outcomes. Contrary to the expectations, percentage EVM does not directly correlate with constellation levels and coderate, as varying these parameters yields similar results when keeping the polarization current and distance fixed. Figure 79 presents two constellations: one for the worst-case scenario at 20cm and another at 50cm. Despite stabilized EVM performance, errors in reception could occur due to the high symbol density in decision zones, justifying the use of encoding methods to mitigate potential reception errors.

Due to limitations in the physical setup assembly, we were able to investigate the behavior of the wireless optical link up to a maximum distance of 250cm. However, it is essential to consider that with a potential increase in distance, there would be a more pronounced opening of the optical beam, leading to dispersion of luminous energy. Additionally, free-space attenuation would be more evident, and alignment precision would become more sensitive, posing a potential point of concern. Taking these factors into
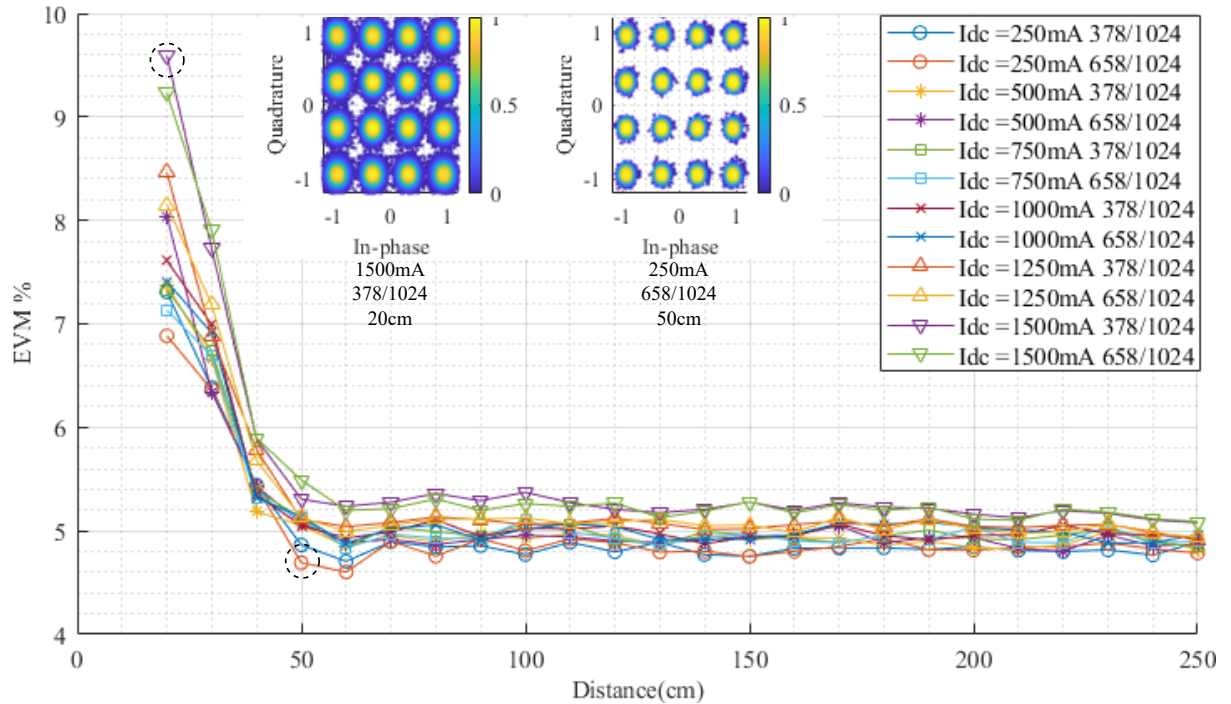
Figure 78 – The EVM performance concerning distance variations and polarization currents using 16QAM modulation. At 20cm with $I_{DC} = 1500$ mA and a coderate of 378/1024, the constellation diagram showed 9.6% EVM. Conversely, at 50cm with $I_{DC} = 250$ mA and a coderate of 658/1024, the EVM was 4.7%. While symbols were well-distributed in the 50cm diagrams, the 20cm constellation displayed an abundance of symbols in the decision zone, potentially affecting reception accuracy.

account, it is expected that for greater distances, the EVM (Error Vector Magnitude) will progressively increase due to signal degradation along the path.

Figure 80 illustrates the relationship between Bit Error Rate (BER) and distance for 16QAM modulation, showing data before decoding, indicating the raw state of the bits. These results are closely related to the Error Vector Magnitude (EVM) displayed in Figure 78. At a distance of 20 cm, despite an apparent peak in the BER curve, the values remain close and are approximately 10^{-4}. However, a significant drop in BER to around 10^{-6} is observed as the experiment progresses, starting from a distance of 50 cm, correlating with a notable reduction in EVM within this distance range. Post LDPC decoding, the reception reveals a BER $= 0$ at all distances, indicating that errors in the transferred bits cannot be observed with the number of bits used after decoding.

Furthermore, Figure 80 also presents the received spectra at 20 cm with 1500 mA during the experiment using the coderate 378/1024. A component with significant energy near 0 Hz was observed, attributed to saturation nonlinearities, even though the transmission is passband through a digital carrier. Notably, for distances of 50 cm and 250 mA, the highlighted components observed in the spectrum at 1500 mA were not present. The photodiode model takes into account its non-linearity [135]. In [136], a detailed
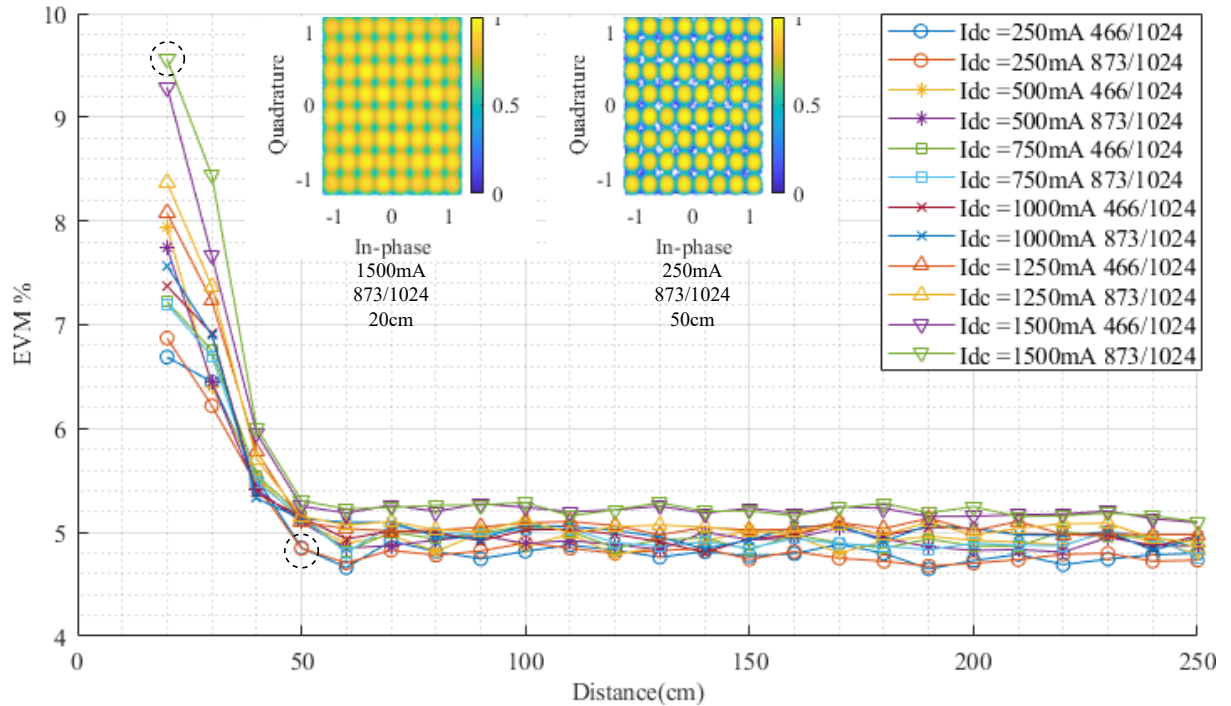
Figure 79 – The EVM performance across varying distances and polarization currents using 64QAM modulation. At a 20cm distance with $I_{DC} = 1500$ mA and a coderate of 873/1024, the constellation diagram showed 9.6% EVM. In contrast, at 50cm with $I_{DC} = 250$ mA and the same coderate, the EVM was 4.9%. Both diagrams displayed numerous symbols in the decision zone, which could affect reception accuracy.

mathematical model is presented regarding the detection process in the photodetector. A current i_{PIN} is generated proportional to the square of the incident light energy, which in turn gives rise to a low-frequency Intermodulation Distortions (IMD) known in the literature as Signal-to-Signal Beating Interference (SSBI). This event can be mitigated by using a sufficient guard band to avoid the IMDs. Another approach is to minimize the incident signal power on the photodetector. With project limitations, reducing the incident power involves increasing the distance between the LED and the photodetector. As a result, at greater distances, IMD effects are not observed.

As discussed for Figure 80, a comparative analysis of BER vs. Distance was conducted for 64QAM modulation. Figure 81 depicts the performance curve. Notably, at 20cm, the combination of high EVM and the elevated modulation level results in a considerably high BER, rendering communication impractical based on these outcomes. However, beyond the 50cm range, the BER stabilizes around 10^{-4}. Additionally, akin to the 16QAM scenario, an unwanted spectral component near 0 Hz is also observed.

Figure 82 illustrates the BER vs. Distance after employing LDPC decoding. Even after decoding, errors persist at 20cm for 1500mA in both coderates and for 1250 with coderate 873/1024. However, the initial BER, initially around 10^{-2}, was reduced by two
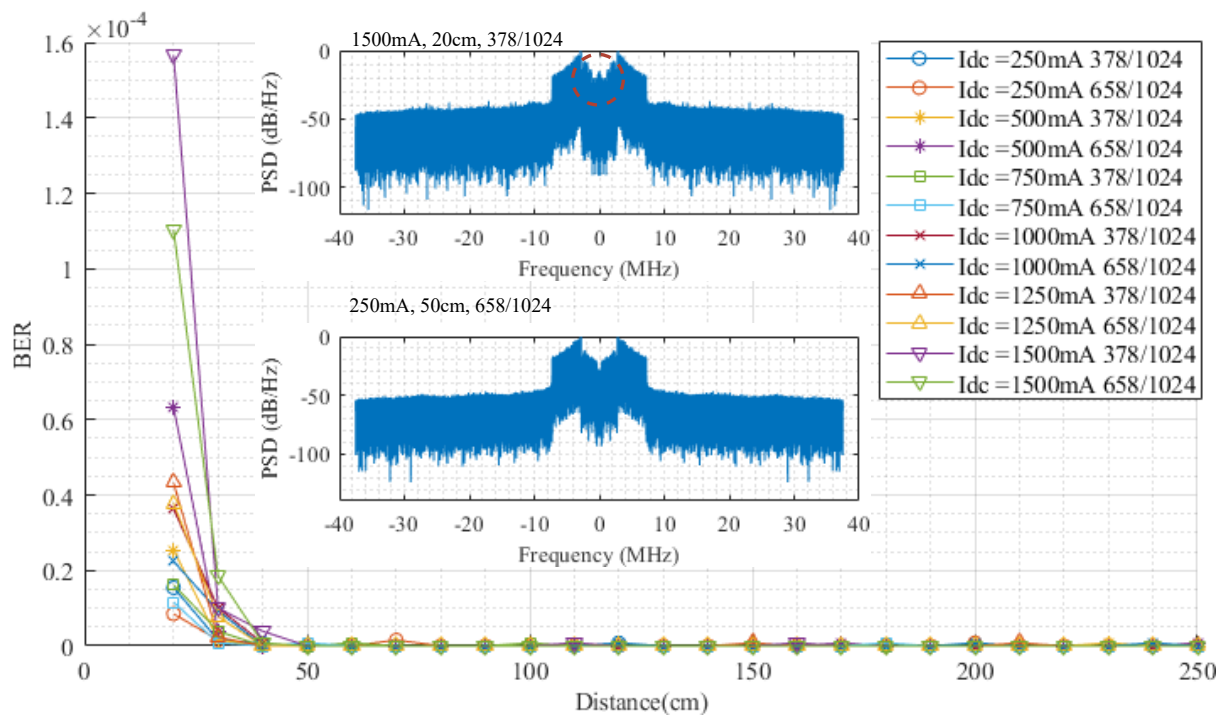
Figure 80 – The BER vs. distance graph using 16 QAM modulation shows a peak at 20cm with 1500mA currents due to photodetector saturation. Beyond 50cm, the BER stabilizes around 10^{-6}. At 1500mA, the spectrum displays an undesired component near the DC level, absent at 250mA polarization current.
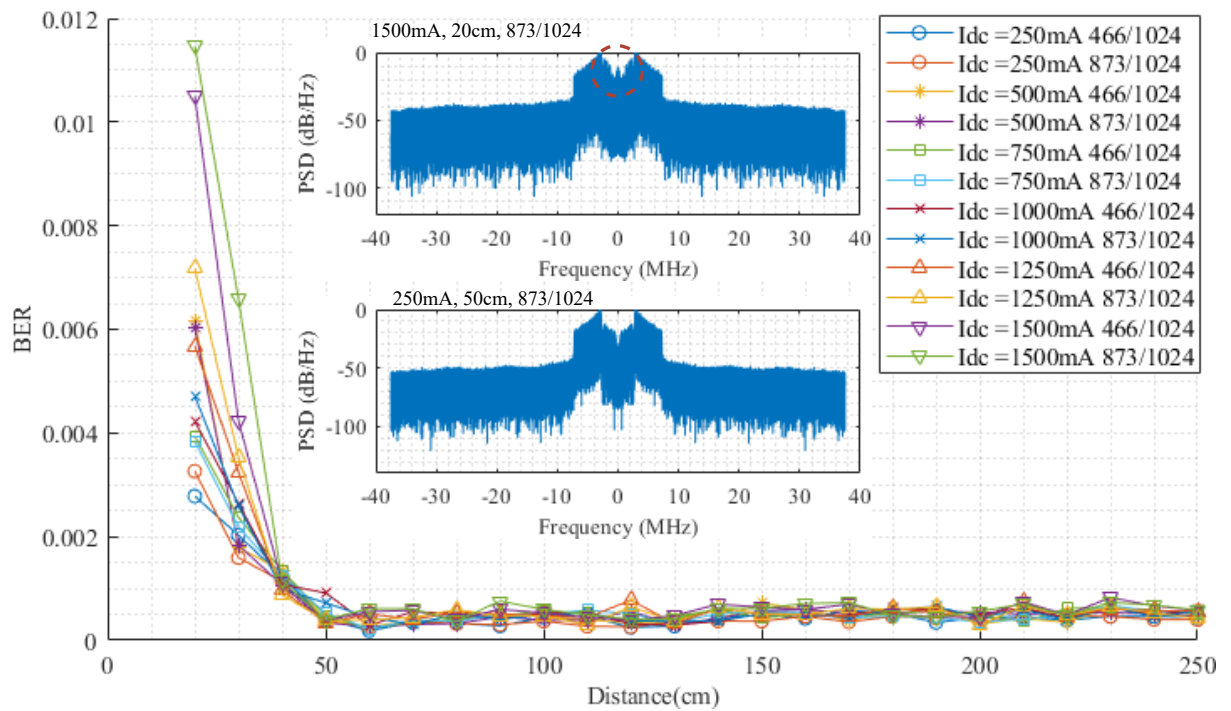
Figure 81 – The BER vs. distance graph using 64 QAM modulation shows a peak at 20cm with 1500mA currents due to photodetector saturation. Beyond 50cm, the BER stabilizes around 10^{-4}. At 1500mA, the spectrum displays an undesired component near the DC level, absent at 250mA polarization current.
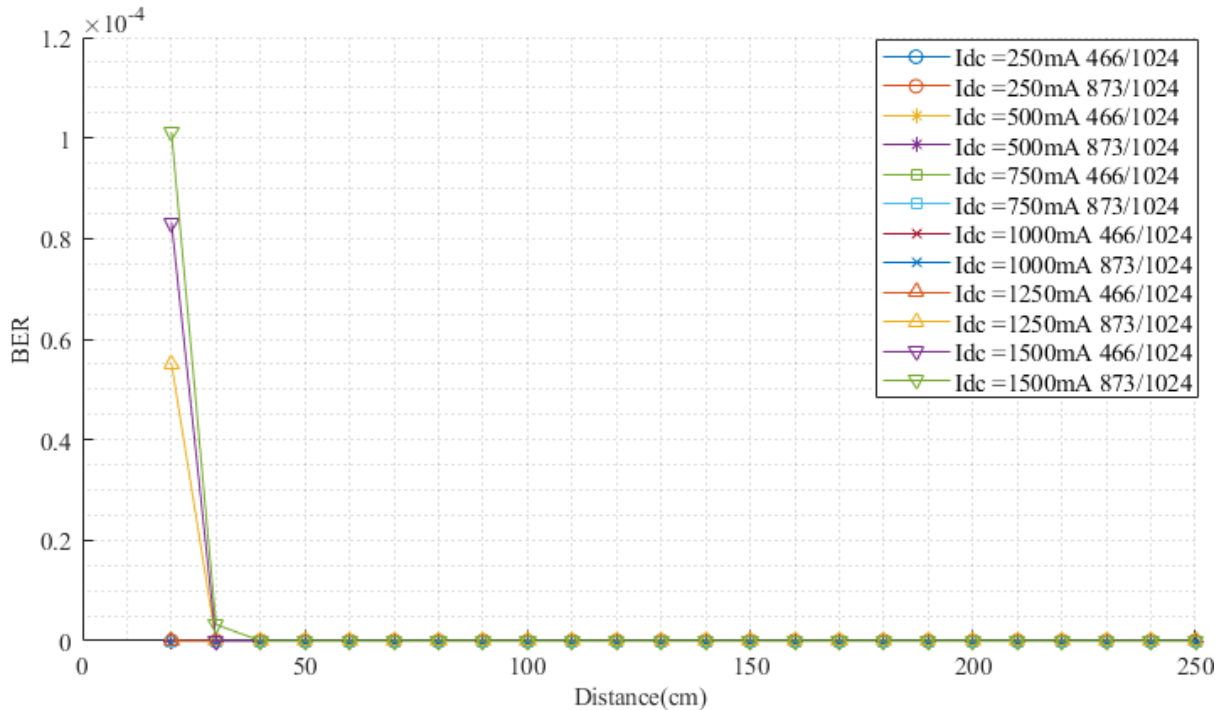
Figure 82 – The BER vs. distance graph using 64 QAM modulation reveals a peak at 20cm with 1500mA, but this significantly reduces upon applying LDPC decoding. Beyond 40cm, no more erroneous packets were received.

orders of magnitude to 10^{-4}. At 30cm, under 1500mA and R = 873/1024, a minimal BER of approximately 10^{-6} was observed, with no further errors detected beyond 40cm. Nonetheless, similar to the discussion on 16QAM, this doesn't imply total immunity to errors; rather, with the volume of data and iterations, no instances of incorrect bits were encountered. Although a BER of 10^{-3} is acceptable for sensor transmission [137] and voice signals [138], it has been observed that in saturation scenarios, a BER of the order of 10^{-2} is encountered. Furthermore, the optical link was limited in distance, and an increase in the physical distance between the transmitter and receiver would result in an increase in EVM. In these scenarios of long links and nonlinear effects, it is beneficial to employ a channel coding mechanism such as LDPC as proposed in the technical specification of 5G. Additionally, various coderates are provided for in the 5G NR, hence, in cases of low EVM, a coderate with many data bits can be utilized, whereas in high EVM scenarios, a coderate with fewer data bits can be employed, thus managing the reliability of the optical link.

Figure 83 displays the total number of retransmissions. In this scenario, it is observed that at 20cm with I_{DC} = 1500mA and coderate 873/1024, there were 30 retransmitted downlinks. This indicates that all three retransmissions per downlink were used, suggesting that no frame was error-free upon reception. On the other hand, at a distance of 20cm, with I_{DC} = 1500 mA and a less aggressive code rate of 466/1024, the count was 21 retransmissions, suggesting that some packets were sent with retransmission but received without error. Upon deeper analysis, three packets were lost after three retransmissions
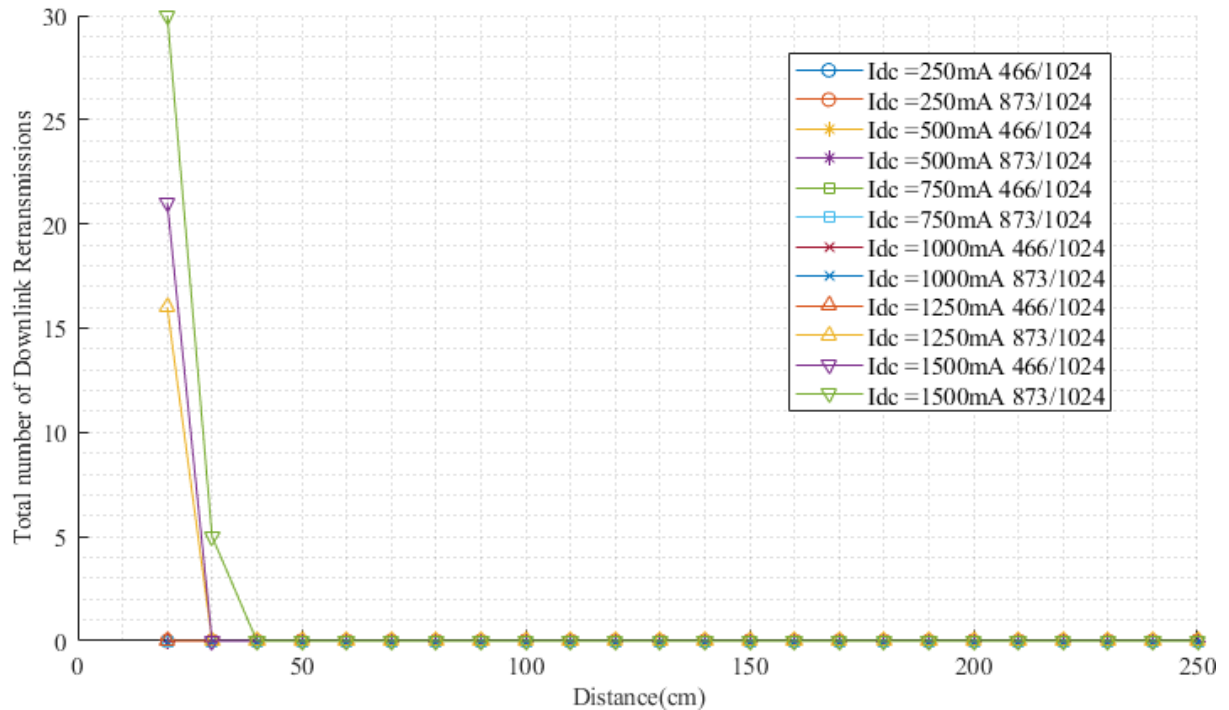
Figure 83 – The graph depicting Retransmissions vs. distance in 64 QAM modulation shows a peak at 20cm with 1500mA. As the BER reduces, the number of retransmissions also decreases. In the initial peak, there were 30 retransmission events, indicating that all packets were retransmitted.

series, while the remaining seven were received with one or two retransmissions. The quantity of retransmissions decreases with the EVM, as seen with $I_{DC} = 1250$ mA, where only 16 retransmissions occurred, one packet was lost, and nine were received with one, two, or zero retransmissions. Lastly, at a distance of 30cm, where the BER was in the order of 10^{-6}, there was a further reduction in the number of retransmissions to just 5, and no packets were lost.

In uplink constellation from Figure 84 observing the received constellation, it's apparent that although the constellation, particularly in QPSK, appears well spread out, the region moving away from the symbol's reference center exhibits significantly lower density. Additionally, there's a noticeable concentration of the yellowish color at the center of the constellation.

Similar to the downlink, there were no observed phenomena correlating EVM with modulation order or coderate in Figure 84, which showcases constellations gathered over 10 operation repetitions. The EVM ranges around 3%, and due to this low EVM, no instances of Bit Error Rate (BER) were observed after LDPC decoding in any case.
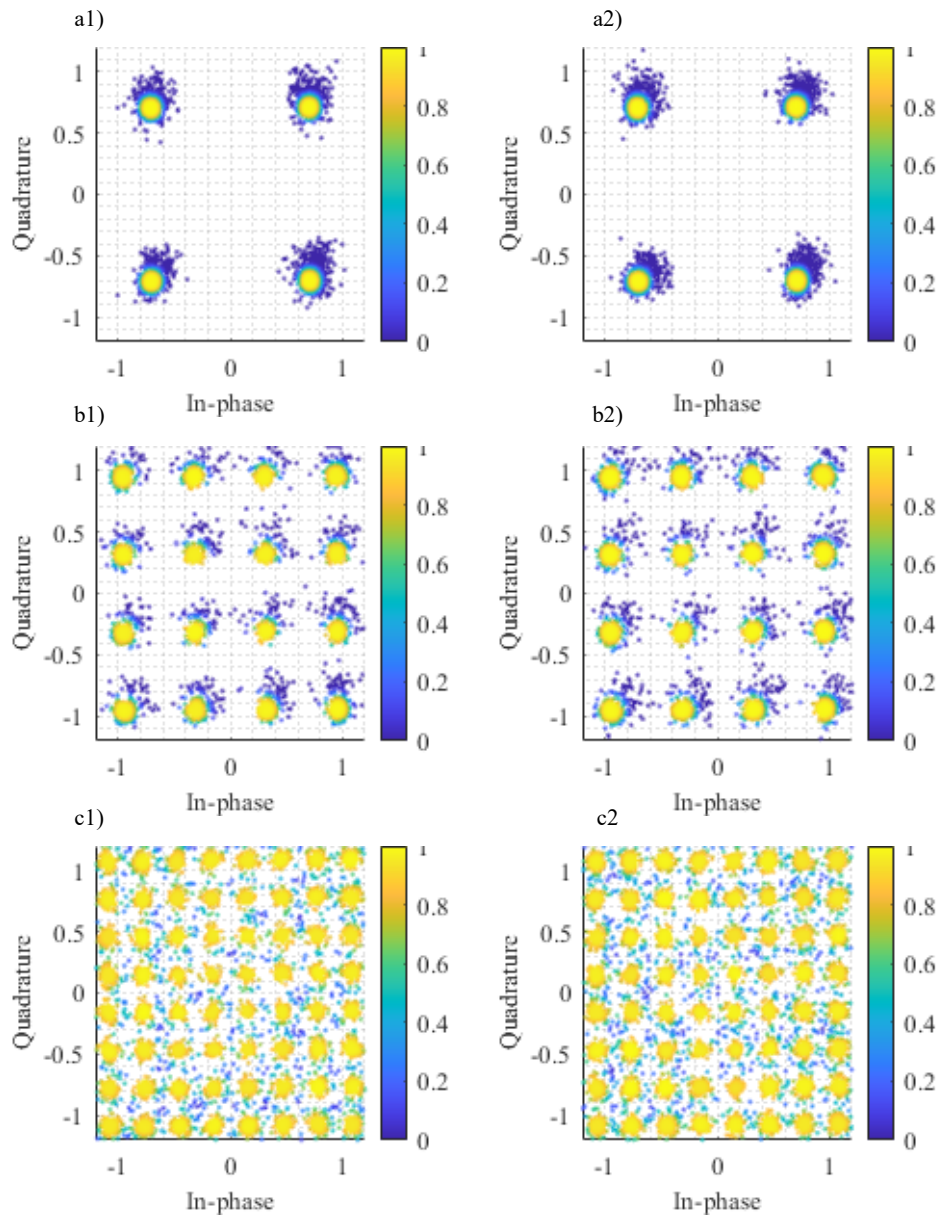
Figure 84 – A summary of the obtained constellations for the uplink includes a1) QPSK, R=120/1024, EVM=2.99% a2) QPSK, R=602/1024, EVM=3.15% b1) 16QAM, R=378/1024, EVM=3.07% b2) 16QAM, R=658/1024, EVM=2.94% c1) 64QAM, R=466/1024, EVM=2.87% c2) 64QAM, R=873/1024, EVM=2.92%

7 Conclusions and Future works

Communication systems, especially within the mobile sector, are in a constant state of evolution, largely driven by initiatives like 3GPP, which releases a new Mobile Communication Release annually. This highlights the ongoing need for prototyping devices such as the ADALM 2000/PLUTO hardware. Furthermore, such prototyping has played a crucial role in the development of hybrid hardware capable of utilizing both Visible Light Communication and Radio Frequency for data transfer. With the rapid advancement of telecommunication systems, as demonstrated by the progress made in 3GPP, Software Defined Radios have unequivocally emerged as powerful tools for prototyping and experimentally validating novel modulations and transmission techniques.

This master's dissertation presented a hardware and software prototype applying functionalities similar to those of 5G gNodeB and User Equipment. The implemented gNodeB was responsible for transmitting Downlink Orthogonal Frequency Division Multiplexing frames in the 5G New Radio standard and receiving Uplink OFDM in the 5G NR standard. Simultaneously, the User Equipment received 5G Downlinks and sent 5G Uplinks containing ACK/NACK feedback to enhance transmission reliability.

Each component, both the gNodeB and User Equipment, was equipped with two ANALOG Devices devices: an ADALM 2000 for VLC communication and an ADALM PLUTO for RF communication. Downlink functionalities such as Synchronization Signal Blocks (SSB), Physical Downlink Shared Channel (PDSCH), Physical Downlink Control Channel (PDCCH), and Uplink functionalities like Sounding Reference Signal (SRS), Physical Uplink Control Channel (PUCCH), and Physical Uplink Shared Channel (PUSCH) were implemented. Furthermore, for payload channels PUSCH/PDSCH, their respective Uplink Shared Channel (UL-SCH) and Downlink Shared Channel (DL-SCH) transport channels were established, incorporating Low-Density Parity-Check (LDPC) coding.

Due to the internal architecture of the ADALM 2000, which has only one input and output DAC/ADC, a strategy for generating OFDM signals solely with real coefficients was necessary. To achieve this, a Digital Up-Converter was employed, performing a baseband shift to a digital carrier with a central frequency $F_c = 2.5$ MHz. This shift also helped address the issue of the high-pass characteristic obtained during the characterization of the Visible Light Communication channel. However, due to the LED's bandwidth being limited to just 10 MHz, it constrained the prototype to operate only within a 5MHz bandwidth for the VLC channel. This bandwidth restriction consequently limited the use of 5G to only numerology $\mu = 0$, employing a Subcarrier Spacing of 15kHz.

Performance analysis and results initially involved assessing Error Vector Magni-

tude versus distance with varying bias current and coding rate. In the case of QPSK, the received constellation was clearly defined, devoid of symbols within decision zones even at LED and photodetector saturation/IMD points. Conversely, for 16QAM, decision zone symbols were observed at 20cm, resulting in a Bit Error Rate of approximately 10^{-4} in that region, stabilizing at 10^{-6} beyond the photodetector saturation/IMD point. Post LDPC decoding, no reception errors were observed. Concerning 64QAM, the significance of LDPC implementation became even more apparent. Without coding, an expected BER of approximately 10^{-2} was predicted within the saturation region at 20cm, stabilizing around 10^{-4}. However, with LDPC applied, the BER reduced from 10^{-2} to 10^{-4} within the saturation/IMD area, with no reception errors observed beyond 40cm. This strongly highlighted the critical role of data coding in ensuring transmission reliability. The retransmission mechanism complements LDPC encoding, where for 64QAM, retransmissions saved 7 packets for 1500mA at 20cm with a code rate of 466/1024, as well as for 1500mA at 30cm with a code rate of 873/1024, where all packets were received with only 5 retransmissions.

Observations from the Uplink transmission results revealed that the EVM remained around 3%. However, it's important to note that the transmission and reception amplifiers were empirically tuned for the test, resulting in this EVM value. This tuning was made for a specific and stationary distance between these two ADALMS: in gNB and UE. In other scenarios, an automatic gain control (for future works) would be a significant enhancement in this prototype.

Upon examining both the uplink and downlink throughput, it becomes evident that all proposed MCSs from 1 to 20 would meet the basic demands of a smart home, where the requirement is 0.5 Mbps for devices such as sensors, smart speakers, smart bulbs, and even for audio and speech streaming. In this context, it's noticeable that by increasing the modulation order, it was also possible to increase the throughput of devices. Even with QPSK and MCS 5, it would be feasible to play back video from an SD residential monitoring camera, which requires approximately 2 Mbps of throughput. From 16QAM with MCS 6 onwards, the use of the VLC medium for online gaming and HD video streaming becomes possible, as the requirement for these cases is 5 Mbps. Furthermore, upon reaching 64QAM levels, the transmission rate surpasses 10 Mbps, and with 64QAM and MCS 20, a rate of 19.74 Mbps is achieved, enabling 4K video transmissions. Therefore, it becomes evident that the prototype could supplement the demand for various connections in a household setting, for instance.

In summary, it is concluded that the prototype has yielded satisfactory results in executing the proposed activities. However, there is room for various enhancements, left for future work:

- Evaluation of the RF Link varying distances.

- Implementation of Automatic Gain Control for transmission and reception.

- Automatic coderate control to enhance the link reliability.

- Introduction of the HARQ mechanism for transmission/reception flow control and frame retransmission.

- Incorporation of Polar coding for control channels.

- Implementation of the remaining channels in the Transport and Logic layer.

References

1 LIN, X. An overview of 5g advanced evolution in 3gpp release 18. *arXiv preprint arXiv:2201.01358*, 2022.

2 GAI, R. et al. A summary of 5g applications and prosprcts of 5g in the internet of things. In: IEEE. *2021 IEEE 2nd International Conference on Big Data, Artificial Intelligence and Internet of Things Engineering (ICBAIE)*. [S.l.], 2021. p. 858–863.

3 ADEBUSOLA, J. A. et al. An overview of 5g technology. In: IEEE. *2020 International Conference in Mathematics, Computer Engineering and Computer Science (ICMCECS)*. [S.l.], 2020. p. 1–4.

4 GUPTA, A.; JHA, R. K. A survey of 5g network: Architecture and emerging technologies. *IEEE access*, IEEE, v. 3, p. 1206–1232, 2015.

5 LIN, X. et al. 5g new radio: Unveiling the essentials of the next generation wireless access technology. *IEEE Communications Standards Magazine*, IEEE, v. 3, n. 3, p. 30–37, 2019.

6 VOOK, F. W. et al. 5g new radio: Overview and performance. In: *2018 52nd Asilomar Conference on Signals, Systems, and Computers*. [S.l.: s.n.], 2018. p. 1247–1251.

7 DILLI, R. Analysis of 5g wireless systems in fr1 and fr2 frequency bands. In: IEEE. *2020 2nd International Conference on Innovative Mechanisms for Industry Applications (ICIMIA)*. [S.l.], 2020. p. 767–772.

8 RODRIGUEZ, J. *Fundamentals of 5G mobile networks*. [S.l.]: John Wiley & Sons, 2015.

9 MATHEUS, L. E. M. et al. Visible light communication: concepts, applications and challenges. *IEEE Communications Surveys & Tutorials*, IEEE, v. 21, n. 4, p. 3204–3237, 2019.

10 KUMAR, N.; LOURENCO, N. R. Led-based visible light communication system: a brief survey and investigation. *J. Eng. Appl. Sci*, v. 5, n. 4, p. 296–307, 2010.

11 CHINCHERO, H. F.; ALONSO, J. M.; ORTIZ, H. Led lighting systems for smart buildings: a review. *IET Smart Cities*, IET, v. 2, n. 3, p. 126–134, 2020.

12 NABAVI, P.; YUKSEL, M. Comprehensive design and prototype of vlc receivers with large detection areas. *Journal of Lightwave Technology*, v. 38, n. 16, p. 4187–4204, 2020.

13 GUZMAN, B. G. et al. Prototyping visible light communication for the internet of things using openvlc. *IEEE Communications Magazine*, v. 61, n. 5, p. 122–128, 2023.

14 PATHAK, P. H. et al. Visible light communication, networking, and sensing: A survey, potential and challenges. *IEEE Communications Surveys Tutorials*, v. 17, n. 4, p. 2047–2077, 2015.

15 MAHDY, A.; DEOGUN, J. Wireless optical communications: a survey. In: *2004 IEEE*

Wireless Communications and Networking Conference (IEEE Cat. No.04TH8733). [S.l.: s.n.], 2004. v. 4, p. 2399–2404 Vol.4.

16 ALSULAMI, O. et al. *Optical Wireless Communication Systems, A Survey*. 2018.

17 CHOWDHURY, M. Z. et al. A comparative survey of optical wireless technologies: Architectures and applications. *IEEE Access*, v. 6, p. 9819–9840, 2018.

18 LEE, K.; PARK, H.; BARRY, J. R. Indoor channel characteristics for visible light communications. *IEEE Communications Letters*, v. 15, n. 2, p. 217–219, 2011.

19 VAVOULAS, A. et al. A survey on ultraviolet c-band (uv-c) communications. *IEEE Communications Surveys Tutorials*, v. 21, n. 3, p. 2111–2133, 2019.

20 RAJAGOPAL, S.; ROBERTS, R. D.; LIM, S.-K. Ieee 802.15.7 visible light communication: modulation schemes and dimming support. *IEEE Communications Magazine*, v. 50, n. 3, p. 72–82, 2012.

21 IDRIS, S. et al. A survey of modulation schemes in visible light communications. In: *2019 3rd International Conference on Trends in Electronics and Informatics (ICOEI)*. [S.l.: s.n.], 2019. p. 1–7.

22 MEJIA, C. E.; GEORGHIADES, C. N. Coding for visible light communication using color-shift keying constellations. *IEEE Transactions on Communications*, v. 67, n. 7, p. 4955–4966, 2019.

23 WILSON, S.; DOBRE, O. Chapter 9 - multicarrier transmission in a frequency-selective channel. In: WILSON, S. K.; WILSON, S.; BIGLIERI, E. (Ed.). *Academic Press Library in Mobile and Wireless Communications*. Oxford: Academic Press, 2016. p. 333–367. ISBN 978-0-12-398281-0. Disponível em: <https://www.sciencedirect.com/science/article/pii/B9780123982810000090>.

24 LEBA, M.; RIUREAN, S.; LONICA, A. Lifi — the path to a new way of communication. In: *2017 12th Iberian Conference on Information Systems and Technologies (CISTI)*. [S.l.: s.n.], 2017. p. 1–6.

25 HAZAREENA, A.; MUSTAFA, B. A. A survey:on the waveforms for 5g. In: *2018 Second International Conference on Electronics, Communication and Aerospace Technology (ICECA)*. [S.l.: s.n.], 2018. p. 64–67.

26 AFGANI, M. et al. Visible light communication using ofdm. In: *2nd International Conference on Testbeds and Research Infrastructures for the Development of Networks and Communities, 2006. TRIDENTCOM 2006.* [S.l.: s.n.], 2006. p. 6 pp.–134.

27 WANG, Z.; MAO, T.; WANG, Q. Optical ofdm for visible light communications. In: *2017 13th International Wireless Communications and Mobile Computing Conference (IWCMC)*. [S.l.: s.n.], 2017. p. 1190–1194.

28 KIM, H.-S. et al. Single side-band orthogonal frequency division multiplexing signal transmission in rf carrier allocated visible light communication. *IET Optoelectronics*, v. 7, n. 6, p. 125–130, 2013. Disponível em: <https://ietresearch.onlinelibrary.wiley.com/doi/abs/10.1049/iet-opt.2013.0074>.

29 ALWIS, C. D. et al. Survey on 6g frontiers: Trends, applications, requirements, technologies and future research. *IEEE Open Journal of the Communications Society*, v. 2, p. 836–886, 2021.

30 CHI, N. et al. Visible light communication in 6g: Advances, challenges, and prospects. *IEEE Vehicular Technology Magazine*, v. 15, n. 4, p. 93–102, 2020.

31 ARIYANTI, S.; SURYANEGARA, M. Visible light communication (vlc) for 6g technology: The potency and research challenges. In: *2020 Fourth World Conference on Smart Trends in Systems, Security and Sustainability (WorldS4)*. [S.l.: s.n.], 2020. p. 490–493.

32 NG, X.-W.; CHUNG, W.-Y. Vlc-based medical healthcare information system. *Biomedical Engineering: Applications, Basis and Communications*, v. 24, n. 02, p. 155–163, 2012. Disponível em: <https://doi.org/10.4015/S1016237212500123>.

33 SEDRA, A. S.; SMITH, K. C. *Microelectronic Circuits*. fifth. [S.l.]: Oxford University Press, 2004.

34 LORENZ, K.; MARQUES, J.; MONTEIRO, T. Diodos emissores de luz e iluminação. *Gazeta de Física da Universidade de Lisboa. Lisboa*, 2015.

35 SHI, D. et al. A device identification method based on led fingerprint for visible light communication system. In: . [S.l.: s.n.], 2020. p. 1–7.

36 YUN, I. *Photodiodes: From Fundamentals to Applications*. [S.l.]: BoD–Books on Demand, 2012.

37 GHASSEMLOOY, Z. et al. *Visible Light Communications: Theory and Applications*. [S.l.]: CRC-Taylor Francis Group, 2017.

38 OKHONIN, S. et al. A dynamic operation of a pin photodiode. *Applied Physics Letters*, AIP Publishing, v. 106, n. 3, 2015.

39 JIANG, H.; YU, P. Equivalent circuit analysis of harmonic distortions in photodiode. *Photonics Technology Letters, IEEE*, v. 10, p. 1608 – 1610, 12 1998.

40 CUI, K. et al. Line-of-sight visible light communication system design and demonstration. In: *2010 7th International Symposium on Communication Systems, Networks Digital Signal Processing (CSNDSP 2010)*. [S.l.: s.n.], 2010. p. 621–625.

41 LI, Y. G.; STUBER, G. L. *Orthogonal frequency division multiplexing for wireless communications*. [S.l.]: Springer Science & Business Media, 2006.

42 CHIDE, N.; DESHMUKH, S.; BOROLE, P. Implementation of ofdm system using ifft and fft. *International Journal of Engineering Research and Applications (IJERA)*, Citeseer, v. 3, n. 1, p. 2009–2014, 2013.

43 BATARIERE, M.; BAUM, K.; KRAUSS, T. P. Cyclic prefix length analysis for 4g ofdm systems. In: IEEE. *IEEE 60th Vehicular Technology Conference, 2004. VTC2004-Fall. 2004*. [S.l.], 2004. v. 1, p. 543–547.

44 ZEPERNICK, H.-J.; FINGER, A. *Pseudo random signal processing: theory and application*. [S.l.]: John Wiley & Sons, 2013.

45   TIMOSHENKO, A. et al. Zadoff-chu sequences synchronization system performance with technological imbalance. In: *2017 Systems of Signal Synchronization, Generating and Processing in Telecommunications (SINKHROINFO)*. [S.l.: s.n.], 2017. p. 1–4.

46   OMRI, A. et al. Synchronization procedure in 5g nr systems. *IEEE Access*, v. 7, p. 41286–41295, 2019.

47   3GPP. *TS 38.211 NR; Physical channels and modulation*. [S.l.], 2023. Version 17.6.0.

48   LIN, J.; WANG, M. The primary synchronization signal of 5g nr. In: *14th International Conference on Wireless Communications, Networking and Mobile Computing (WiCOM 2018)*. [S.l.: s.n.], 2018.

49   SUN, B. et al. A comparative study of 3d ue positioning in 5g new radio with a single station. *Sensors*, MDPI, v. 21, n. 4, p. 1178, 2021.

50   WYGLINSKI, A. et al. *Software-Defined Radio for Engineers*. Artech House, 2018. (Artech House mobile communications series). ISBN 9781630814595. Disponível em: <https://books.google.com.br/books?id=cKR5DwAAQBAJ>.

51   FISHER, R. A. Statistical methods for research workers. In: *Breakthroughs in statistics: Methodology and distribution*. [S.l.]: Springer, 1970. p. 66–70.

52   OUYANG, X. *Digital signal processing for fiber-optic communication systems*. Tese (Doutorado) — University College Cork, 2017.

53   VILAR, F. C. Implementation of zero forcing and mmse equalization techniques in ofdm. Universitat Politècnica de Catalunya, 2015.

54   PENNA, F.; KWON, H.; BAI, D. Noise variance estimation in 5g nr receivers: Bias analysis and compensation. In: *2021 IEEE Global Communications Conference (GLOBECOM)*. [S.l.: s.n.], 2021. p. 1–6.

55   CARCEL, J. L. et al. Imt-2020 key performance indicators: Evaluation and extension towards 5g new radio point-to-multipoint. In: *2019 IEEE International Symposium on Broadband Multimedia Systems and Broadcasting (BMSB)*. [S.l.: s.n.], 2019. p. 1–5.

56   INC., T. M. *5G Toolbox Simulate, analyze, and test 5G communications systems*. Natick, Massachusetts, United States: The MathWorks Inc. Disponível em: <https://www.mathworks.com/products/5g.html>.

57   JEON, J. Nr wide bandwidth operations. *IEEE Communications Magazine*, v. 56, n. 3, p. 42–46, 2018.

58   DING, Y.; KWON, H. Doppler spread estimation for 5g nr with supervised learning. In: *GLOBECOM 2020 - 2020 IEEE Global Communications Conference*. [S.l.: s.n.], 2020. p. 1–7.

59   LIEN, S.-Y. et al. 5g new radio: Waveform, frame structure, multiple access, and initial access. *IEEE Communications Magazine*, v. 55, n. 6, p. 64–71, 2017.

60   KOTTKAMP, M. et al. *5G New Radio: Fundamentals, Procedures, Testing Aspects*. Rohde & Schwarz GmbH & Company KG, 2022. ISBN 9783939837152. Disponível em: <https://books.google.com.br/books?id=wBOwwwEACAAJ>.

61 ZAIDI, A. et al. *5G New Radio Designing for the Future.* [S.l.], 2017. Disponível em: <https://www.ericsson.com/49e9d0/assets/local/reports-papers/ericsson-technology-review/docs/2017/designing-for-the-future---the-5g-nr-physical-layer.pdf>.

62 3GPP. *TS 38.101 NR; User Equipment (UE) radio transmission and reception; Part 1: Range 1 Standalone.* [S.l.], 2023. Version 18.3.0.

63 BERTENYI, B. et al. Ng radio access network (ng-ran). *Journal of ICT Standardization,* v. 6, n. 1-2, p. 59–76, 2018.

64 RINALDI, F.; RASCHELLA, A.; PIZZI, S. 5g nr system design: A concise survey of key features and capabilities. *Wireless Networks,* Springer, v. 27, p. 5173–5188, 2021.

65 MORAIS, D. H. 5g nr overview. In: *5G NR, Wi-Fi 6, and Bluetooth LE 5: A Primer on Smartphone Wireless Technologies.* [S.l.]: Springer, 2023. p. 101–129.

66 HUI, D. et al. Channel coding in 5g new radio: A tutorial overview and performance comparison with 4g lte. *IEEE Vehicular Technology Magazine,* v. 13, n. 4, p. 60–69, 2018.

67 3GPP. *TS 38.214 NR; Physical layer procedures for data.* [S.l.], 2023. Version 18.0.0.

68 INC., T. M. *nrTBS.* Natick, Massachusetts, United States: The MathWorks Inc. Disponível em: <https://www.mathworks.com/help/5g/ref/nrtbs.html#mw__9b8c0746-596e-40e7-a586-f916f88cc3d6>.

69 3GPP. *TS38.212 NR; Multiplexing and channel coding.* [S.l.], 2023. Version 18.3.0.

70 INC., T. M. *Apply DL-SCH encoder processing chain.* Natick, Massachusetts, United States: The MathWorks Inc. Disponível em: <https://www.mathworks.com/help/5g/ref/nrdlsch-system-object.html>.

71 RICHARDSON, T.; KUDEKAR, S. Design of low-density parity check codes for 5g new radio. *IEEE Communications Magazine,* v. 56, n. 3, p. 28–34, 2018.

72 HAMIDI-SEPEHR, F.; NIMBALKER, A.; ERMOLAEV, G. Analysis of 5g ldpc codes rate-matching design. In: *2018 IEEE 87th Vehicular Technology Conference (VTC Spring).* [S.l.: s.n.], 2018. p. 1–5.

73 INC., T. M. *nrDLSCH - Apply DL-SCH encoder processing chain.* Natick, Massachusetts, United States: The MathWorks Inc. Disponível em: <https://www.mathworks.com/help/5g/ref/nrdlsch-system-object.html>.

74 LIN, Z. et al. Ss/pbch block design in 5g new radio (nr). In: *2018 IEEE Globecom Workshops (GC Wkshps).* [S.l.: s.n.], 2018. p. 1–6.

75 INC., T. M. *nrResourceGrid - Generate empty carrier slot resource grid.* Natick, Massachusetts, United States: The MathWorks Inc. Disponível em: <https://www.mathworks.com/help/5g/ref/nrresourcegrid.html>.

76 3GPP. *TS 36.331 Evolved Universal Terrestrial Radio Access (E-UTRA); Radio Resource Control (RRC); Protocol specification.* [S.l.], 2023. Version 17.6.0.

77 INC., T. M. *nrPSS - Generate PSS symbols.* Natick, Massachusetts, United States: The MathWorks Inc. Disponível em: <https://www.mathworks.com/help/5g/ref/nrpss.html>.

78 INC., T. M. *nrSSS - Generate SSS symbols*. Natick, Massachusetts, United States: The MathWorks Inc. Disponível em: <https://www.mathworks.com/help/5g/ref/nrsss.html>.

79 INC., T. M. *nrPBCHDMRS - Generate PBCH DMRS symbols*. Natick, Massachusetts, United States: The MathWorks Inc. Disponível em: <https://www.mathworks.com/help/5g/ref/nrpbchdmrs.html>.

80 INC., T. M. *nrPBCHDMRSIndices - Generate PBCH DM-RS resource element indice*. Natick, Massachusetts, United States: The MathWorks Inc. Disponível em: <https://www.mathworks.com/help/5g/ref/nrpbchdmrsindices.html>.

81 INC., T. M. *nrPBCH - Generate PBCH modulation symbols*. Natick, Massachusetts, United States: The MathWorks Inc. Disponível em: <https://www.mathworks.com/help/5g/ref/nrpbch.html>.

82 INC., T. M. *nrPBCHIndices - Generate PBCH resource element indice*. Natick, Massachusetts, United States: The MathWorks Inc. Disponível em: <https://www.mathworks.com/help/5g/ref/nrpbchindices.html>.

83 3GPP. *TS 36.211 Evolved Universal Terrestrial Radio Access (E-UTRA); Physical channels and modulation*. [S.l.], 2023. Version 17.4.0.

84 INC., T. M. *nrPDCCHResources - Generate PDCCH and PDCCH DM-RS resources*. Natick, Massachusetts, United States: The MathWorks Inc. Disponível em: <https://www.mathworks.com/help/5g/ref/nrpdcchresources.html>.

85 INC., T. M. *nrPDCCH - Generate PDCCH modulation symbols*. Natick, Massachusetts, United States: The MathWorks Inc. Disponível em: <https://www.mathworks.com/help/5g/ref/nrpdcch.html>.

86 INC., T. M. *NR PDSCH Resource Allocation and DM-RS and PT-RS Reference Signals*. Natick, Massachusetts, United States: The MathWorks Inc. Disponível em: <https://www.mathworks.com/help/5g/ug/nr-pdsch-resource-allocation-and-dmrs-and-ptrs-reference-signals.html>.

87 INC., T. M. *nrPDSCHDMRS - Generate PDSCH DM-RS symbols*. Natick, Massachusetts, United States: The MathWorks Inc. Disponível em: <https://www.mathworks.com/help/5g/ref/nrpdschdmrs.html>.

88 INC., T. M. *nrPDSCHDMRSIndices - Generate PDSCH DM-RS indices*. Natick, Massachusetts, United States: The MathWorks Inc. Disponível em: <https://www.mathworks.com/help/5g/ref/nrpdschdmrsindices.html>.

89 INC., T. M. *nrPDSCH - Generate PDSCH modulation symbols*. Natick, Massachusetts, United States: The MathWorks Inc. Disponível em: <https://www.mathworks.com/help/5g/ref/nrpdsch.html>.

90 INC., T. M. *nrPDSCHIndices - Generate PDSCH resource element indice*. Natick, Massachusetts, United States: The MathWorks Inc. Disponível em: <https://www.mathworks.com/help/5g/ref/nrpdschindices.html>.

91 INC., T. M. *nrSRS - Generate uplink SRS symbols*. Natick, Massachusetts, United States: The MathWorks Inc. Disponível em: <https://www.mathworks.com/help/5g/ref/nrsrs.html>.

92 INC., T. M. *nrSRSIndices - Generate uplink SRS resource element indices.* Natick, Massachusetts, United States: The MathWorks Inc. Disponível em: <https://www.mathworks.com/help/5g/ref/nrsrsindices.html>.

93 3GPP. *TS 38.300 NR; NR and NG-RAN Overall description; Stage-2.* [S.l.], 2023. Version 17.6.0.

94 SILVA, J. de C. et al. Lorawan — a low power wan protocol for internet of things: A review and opportunities. In: *2017 2nd International Multidisciplinary Conference on Computer and Energy Science (SpliTech).* [S.l.: s.n.], 2017. p. 1–6.

95 INC., T. M. *nrPUCCH - Generate PUCCH modulation symbols.* Natick, Massachusetts, United States: The MathWorks Inc. Disponível em: <https://www.mathworks.com/help/5g/ref/nrpucchdmrs.html>.

96 INC., T. M. *nrPUCCHIndices - Generate PUCCHresource element indice.* Natick, Massachusetts, United States: The MathWorks Inc. Disponível em: <https://www.mathworks.com/help/5g/ref/nrpucchdmrsindices.html>.

97 INC., T. M. *nrPUCCH - Generate PUCCH modulation symbols.* Natick, Massachusetts, United States: The MathWorks Inc. Disponível em: <https://www.mathworks.com/help/5g/ref/nrpucch.html>.

98 INC., T. M. *nrPUCCHIndices - Generate PUCCHresource element indice.* Natick, Massachusetts, United States: The MathWorks Inc. Disponível em: <https://www.mathworks.com/help/5g/ref/nrpucchindices.html>.

99 INC., T. M. *nrPUSCHDMRS - Generate PDSCH DM-RS symbols.* Natick, Massachusetts, United States: The MathWorks Inc. Disponível em: <https://www.mathworks.com/help/5g/ref/nrPUSCHdmrs.html>.

100 INC., T. M. *nrPUSCHDMRSIndices - Generate PDSCH DM-RS indices.* Natick, Massachusetts, United States: The MathWorks Inc. Disponível em: <https://www.mathworks.com/help/5g/ref/nrPUSCHdmrsindices.html>.

101 INC., T. M. *nrPUSCH - Generate PDSCH modulation symbols.* Natick, Massachusetts, United States: The MathWorks Inc. Disponível em: <https://www.mathworks.com/help/5g/ref/nrPUSCH.html>.

102 INC., T. M. *nrPUSCHIndices - Generate PDSCH resource element indice.* Natick, Massachusetts, United States: The MathWorks Inc. Disponível em: <https://www.mathworks.com/help/5g/ref/nrPUSCHindices.html>.

103 3GPP. *NR; User Equipment (UE) radio access capabilities.* [S.l.], 2024. Version 18.3.0.

104 Adrian Suciu. *ADALM2000 Overview.* Disponível em: <https://wiki.analog.com/university/tools/m2k>.

105 MathWorks, Inc. *ADALM2000 Support from MATLAB.* Disponível em: <https://www.mathworks.com/hardware-support/adalm2000.html>.

106 Digilent. *BNC Adapter.* Disponível em: <https://digilent.com/reference/test-and-measurement/bnc-adapter-board/start>.

107 Digilent. *Getting Started with the BNC Adapter*. Disponível em: <https://digilent.com/reference/test-and-measurement/bnc-adapter-board/getting-started-guide>.

108 Robin Getz. *M2K HDL Architecture*. Disponível em: <https://wiki.analog.com/resources/fpga/docs/hdl/m2k#axi_ad9963>.

109 XILINX. *Zynq-7000 SoC Data Sheet: Overview*. [S.l.], 2018. Version 1.11.1. Disponível em: <https://docs.xilinx.com/v/u/en-US/ds190-Zynq-7000-Overview>.

110 Pop Andreea. *Reference Manual (Understanding the Internals)*. Disponível em: <https://wiki.analog.com/university/tools/m2k/users/reference_manual>.

111 Rob Riggs. *Controlling the transceiver and transferring data*. Disponível em: <https://wiki.analog.com/university/tools/pluto/controlling_the_transceiver_and_transferring_data>.

112 Travis Collins. *What is libiio?* Disponível em: <https://wiki.analog.com/resources/tools-software/linux-software/libiio>.

113 JUNTEK. *DPA-2698 English Manual*. [S.l.]. Disponível em: <http://68.168.132.244/DPA-2698_EN_manual.pdf>.

114 LABS, P. P. *Model 5575A Bias Tee Product Specification*. [S.l.]. Disponível em: <http://woojoohitech.com/pages/pdf/5575A%20SPEC-4040045.pdf>.

115 LUMILEDS. *LUXEON Rebel ES*. [S.l.]. Disponível em: <https://br.mouser.com/datasheet/2/602/DS61-542365.pdf>.

116 ZWAAG, K. M. van der. *Application of Visible Light Communications in Intensive Care Medical Environments*. Dissertação (Mestrado) — UFES Universidade Federal do Espirito Santo, 2020.

117 QORVO. *TQP3M9037 Ultra Low-Noise, High Linearity LNA* . [S.l.]. Disponível em: <https://br.mouser.com/datasheet/2/412/TQP3M9037_Data_Sheet-1500717.pdf>.

118 MAHMUD, M. *BER for Different Modulation Techniques and PAPR Reduction in OFDM*. [S.l.: s.n.], 2012.

119 XU, X.; XIE, X.; WANG, F. Digital up and down converter in ieee 802.16d. In: *2006 8th international Conference on Signal Processing*. [S.l.: s.n.], 2006. v. 1.

120 GETZ, R. *Basic internals of Pluto*. Analog Devices, 2021. Disponível em: <https://wiki.analog.com/university/tools/pluto/users/understanding>.

121 The MathWorks Inc. *ADALM-PLUTO Radio Support from Communications Toolbox*. Disponível em: <https://www.mathworks.com/hardware-support/adalm-pluto-radio.html>.

122 The MathWorks Inc. *FIR Interpolation*. Disponível em: <https://www.mathworks.com/help/dsp/ref/firinterpolation.html>.

123 The MathWorks Inc. *MATLAB Filter Design Wizard for AD9361*. Disponível em: <https://wiki.analog.com/resources/eval/user-guides/ad-fmcomms2-ebz/software/filters>.

124   The MathWorks Inc. *AD9361 Filter Design Wizard.* Disponível em: <https://www.mathworks.com/matlabcentral/fileexchange/45843-ad9361-filter-design-wizard>.

125   Michael Hennerich. *Customizing the Pluto configuration.* Disponível em: <https://wiki.analog.com/university/tools/pluto/users/customizing>.

126   Jinchang Electron Global Service. *GSM Antenna JCG401.* Disponível em: <https://wiki.analog.com/_media/university/tools/pluto/users/jcg401.pdf>.

127   IEEE Recommended Practice for Antenna Measurements. *IEEE Std 149-2021 (Revision of IEEE Std 149-1977)*, p. 1–207, 2022.

128   BALANIS, C. *Antenna Theory: Analysis and Design.* Wiley, 2015. ISBN 9781119178989. Disponível em: <https://books.google.com.br/books?id=PTFcCwAAQBAJ>.

129   LATHI, B.; DING, Z. *Modern Digital and Analog Communication Systems.* Oxford University Press, 2019. (Oxford series in electrical and computer engineering). ISBN 9780190686840. Disponível em: <https://books.google.com.br/books?id=KZpnswEACAAJ>.

130   SARKIS, G.; SORIAGA, J. B.; RICHARDSON, T. Self-decodability of harq retransmissions for 5g nr ldpc codes. In: IEEE. *2021 11th International Symposium on Topics in Coding (ISTC).* [S.l.], 2021. p. 1–5.

131   LEBL, A.; MITIĆ, D.; VASILJEVIĆ, V. Bit error rate estimation and confidence levels. Technical University of Gabrovo, Bulgaria, 2019.

132   Paul Lee, Dieter Trimmel, Eytan Hallside. *No bump to bitrates for digital apps in the near term: Is a period of enough fixed broadband connectivity approaching?* Disponível em: <https://www2.deloitte.com/us/en/insights/industry/technology/technology-media-and-telecom-predictions/2024/bandwidth-demand-forecast.html>.

133   Gateway Fiber. *How Much Internet Speed Does a Smart Home Need?* Disponível em: <https://www.gatewayfiber.com/blog/how-much-internet-speed-do-you-need-for-a-smart-home>.

134   Full Spectrum. *What Internet Speed Do I Need For A Smart Home?* Disponível em: <https://www.fullspectrumtg.com/what-internet-speed-do-i-need-for-a-smart-home-2/>.

135   HUTCHINSON, M. N.; FRIGO, N. J.; PEASANT, J. R. Novel characterization of photodiode intermodulation distortion. In: *2016 Conference on Lasers and Electro-Optics (CLEO).* [S.l.: s.n.], 2016. p. 1–2.

136   PEREIRA, E. d. V. et al. Impact of optical power in the guard-band reduction of an optimized ddo-ofdm system. *Journal of Lightwave Technology*, v. 33, n. 23, p. 4717–4725, 2015.

137   KRISHNAMOORTHY, S. et al. Channel frame error rate for bluetooth in the presence of microwave ovens. In: IEEE. *Proceedings IEEE 56th Vehicular Technology Conference.* [S.l.], 2002. v. 2, p. 927–931.

138 WALRAND, J.; VARAIYA, P. Chapter 2 - network services and layered architectures. In: WALRAND, J.; VARAIYA, P. (Ed.). *High-Performance Communication Networks (Second Edition)*. Second edition. San Francisco: Morgan Kaufmann, 2000. p. 39–102. ISBN 978-1-55860-574-9. Disponível em: <https://www.sciencedirect.com/science/article/pii/B9780080508030500071>.

Appendix

APPENDIX A – Trigonometric Identity

Below are the main trigonometric identities used in justifying modulations and demodulations using orthogonal carriers [129].

$$sin^2x + cos^2x = 1 \tag{A.1}$$

$$sin^2x = \frac{1}{2}(1 - cos2x) \tag{A.2}$$

$$cos^2x = \frac{1}{2}(1 + cos2x) \tag{A.3}$$

$$sinx\,cosx = \frac{1}{2}sin2x \tag{A.4}$$

APPENDIX B – Modulation Coding Scheme

As proposed in [67] there are several modulation coding scheme as ilustrated in Table 12. The MCS table indicates the MCS index used in DCI, modulation order and Code Rate used in PDSCH symbols.

MCS Index	Modulation Order Qm	Code Rate
1	QPSK	120/1024
2	QPSK	193/1024
3	QPSK	308/1024
4	QPSK	449/1024
5	QPSK	602/1024
6	16QAM	378/1024
7	16QAM	434/1024
8	16QAM	490/1024
9	16QAM	553/1024
10	16QAM	616/1024
11	16QAM	658/1024
12	64QAM	466/1024
13	64QAM	517/1024
14	64QAM	567/1024
15	64QAM	616/1024
16	64QAM	666/1024
17	64QAM	719/1024
18	64QAM	772/1024
19	64QAM	822/1024
20	64QAM	873/1024
21	256QAM	682.5/1024
22	256QAM	711/1024
23	256QAM	754/1024
24	256QAM	797/1024
25	256QAM	841/1024
26	256QAM	885/1024
27	256QAM	916.5/1024
28	256QAM	948/1024

Table 12 – The Modulation Coding Scheme (MCS) encompasses all modulation types and code rates sanctioned within the 3GPP specification. It defines the range of modulation schemes and corresponding code rates permissible for generating PDSCH (Physical Downlink Shared Channel) symbols in adherence to the standards.

APPENDIX C – Base sequence for $M_{ZC} = 24$

This section shows the $\phi(n)$ values used in the Sounding Reference Signals Zadoff-Chu sequence generation. Table 13 is from [47].

u	$\phi(0)...\phi(23)$																							
0	-1	-3	3	-1	3	1	3	-1	1	-3	-1	-3	-1	1	3	-3	-1	-3	3	3	3	-3	-3	-3
1	-1	-3	3	1	1	-3	1	-3	-3	1	-3	-1	-1	3	-3	3	3	3	-3	1	3	3	-3	-3
2	-1	-3	-3	1	-1	-1	-3	1	3	-1	-3	-1	-1	-3	1	1	3	1	-3	-1	-1	3	-3	-3
3	1	-3	3	-1	-3	-1	3	3	1	-1	1	1	3	-3	-1	-3	-3	-3	-1	3	-3	-1	-3	-3
4	-1	3	-3	-3	-1	3	-1	-1	1	3	1	3	-1	-1	-3	1	3	1	-1	-3	1	-1	-3	-3
5	-3	-1	1	-3	-3	1	1	-3	3	-1	-1	-3	1	3	1	-1	-3	-1	-3	1	-3	-3	-3	-3
6	-3	3	1	3	-1	1	-3	1	-3	1	-1	-3	-1	-3	-3	-3	-1	-1	-1	1	1	-3	-3	-3
7	-3	1	3	-1	1	-1	3	-3	3	-1	-3	-1	-3	3	-1	-1	-1	-3	-1	-1	-3	3	3	-3
8	-3	1	-3	3	-1	-1	-1	-3	3	1	-1	-3	-1	1	3	-1	1	-1	1	-3	-3	-3	-3	-3
9	1	1	-1	-3	-1	1	1	-3	1	-1	1	-3	3	-3	-3	3	-1	-3	1	3	-3	1	-3	-3
10	-3	-3	-3	-1	3	-3	3	1	3	1	-3	-1	-1	-3	1	1	3	1	-1	-3	3	1	3	-3
11	-3	3	-1	3	1	-1	-1	-1	3	3	1	1	1	3	3	1	-3	-3	-1	1	-3	1	3	-3
12	3	-3	3	-1	-3	1	3	1	-1	-1	-3	-1	3	-3	3	-1	-1	3	3	-3	-3	3	-3	-3
13	-3	3	-1	3	-1	3	3	1	1	-3	1	3	-3	3	-3	-3	-1	1	3	-3	-1	-1	-3	-3
14	-3	1	-3	-1	-1	3	1	3	-3	1	-1	3	3	-1	-3	3	-3	-1	-1	-3	-3	-3	3	-3
15	-3	-1	-1	-3	1	-3	-3	-1	-1	3	-1	1	-1	3	1	-3	-1	3	1	1	-1	-1	-3	-3
16	-3	-3	1	-1	3	3	-3	-1	1	-1	-1	1	1	-1	-1	3	-3	1	-3	1	-1	-1	-1	-3
17	3	-1	3	-1	1	-3	1	1	-3	-3	3	-3	-1	-1	-1	-1	-3	-3	-1	1	1	-3	-3	-3
18	-3	1	-3	1	-3	-3	1	-3	1	-3	-3	-3	-3	1	-3	-3	1	1	-3	1	1	-3	-3	-3
19	-3	-3	3	3	1	-1	-1	-1	1	-3	-1	1	-1	3	-3	-1	-3	-1	-1	1	-3	3	-1	-3
20	-3	-3	-1	-1	-1	-3	1	-1	-3	-1	3	-3	1	-3	3	-3	3	3	1	-1	-1	1	-3	-3
21	3	-1	1	-1	3	-3	1	1	3	-1	-3	3	1	-3	3	-1	-1	-1	-1	1	-3	-3	-3	-3
22	-3	1	-3	3	-3	1	-3	3	1	-1	-3	-1	-3	-3	-3	-3	1	3	-1	1	3	3	3	-3
23	-3	-1	1	-3	-1	-1	1	1	1	3	3	-1	1	-1	1	-1	-1	-3	-3	-3	3	1	-1	-3
24	-3	3	-1	-3	-1	-1	-1	3	-1	-1	3	-3	-1	3	-3	3	-3	-1	3	1	1	-1	-3	-3
25	-3	1	-1	-3	-3	-1	1	-3	-1	-3	1	1	-1	1	1	3	3	3	-1	1	-1	1	-1	-3
26	-1	3	-1	-1	3	3	-1	-1	-1	3	-1	-3	1	3	1	1	-3	-3	-3	-1	-3	-1	-3	-3
27	3	-3	-3	-1	3	3	-3	-1	3	1	1	1	3	-1	3	-3	-1	3	-1	3	1	-1	-3	-3
28	-3	1	-3	1	-3	1	1	3	1	-3	-3	-1	1	3	-1	-3	3	1	-1	-3	-3	-3	-3	-3
29	3	-3	-1	1	3	-1	-1	-3	-1	3	-1	-3	-1	-3	3	-1	3	1	1	-3	3	-3	-3	-3

Table 13 – Values for $\phi(n)$ with Zadoff-Chu sequence lenght $M_{ZC} = 24$

APPENDIX D – Receiver Photodiode Schematics